

UNIVERSITY OF CALIFORNIA

Los Angeles

Plasma Lenses for Relativistic Electron Beams

A dissertation submitted in partial satisfaction of the
requirements for the degree
Doctor of Philosophy in Electrical Engineering

by


Joseph Grau Davis

1996

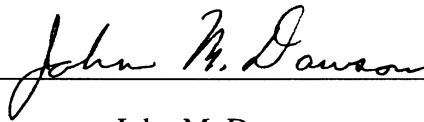
EMS
LIB

© Copyright by
Joseph Grau Davis
1996

The dissertation of Joseph Grau Davis is approved.



Warren B. Mori



John M. Dawson



Chan Joshi, Committee Chair

University of California, Los Angeles

1996

Contents

LIST OF FIGURES	v
ACKNOWLEDGMENTS	ix
VITA AND PUBLICATIONS	x
ABSTRACT	xiii
1 Introduction	1
2 Theory of "Passive" Plasma Lenses	9
2.1 Introduction	9
2.2 Simple Physical Model	10
2.3 Wakefield Model	19
2.4 Simulations	25
2.5 Summary	29
3 Development of an Electron Beam for Laboratory Demonstration of Plasma Lenses	30
3.1 Introduction	30
3.2 RF Photo-injector	33
3.2.1 Introduction	33
3.2.2 RF Gun Tuning	39
3.2.3 Drive Laser	53

3.2.4	Klystron and Timing System	59
3.3	Electron Beam Measurements	61
3.3.1	Introduction	61
3.3.2	Quantum Efficiency Measurements	64
3.3.3	Bunch Length Measurements	76
3.3.4	Energy Measurements	84
3.3.5	Emittance Measurements	88
3.3.6	Profile Measurements	92
3.4	Summary	98
4	Overdense Plasma Lens Experiment	99
4.1	Introduction	99
4.2	Electron Beamline	102
4.3	Plasma Source	106
4.4	Time Integrated Measurements	111
4.5	Time Resolved Measurements	115
4.6	Wakefield Analysis	119
4.7	Simulations	128
4.8	Summary	134
5	Conclusion	135

List of Figures

2.1	Electron Beam in Vacuum	10
2.2	Electron Beam in an Overdense Plasma	13
2.3	Return Current in an Overdense Plasma	14
2.4	Electron Beam in an Underdense Plasma	16
2.5	Temporal Wakefield Response for Various Plasma Densities	22
2.6	Radial Wakefield Response for Various Plasma Densities	23
2.7	Simulation of Adiabatic Return Currents in an Overdense Plasma	27
2.8	Simulation of Wakefield Return Currents in an Overdense Plasma	27
3.1	UCLA RF Gun	38
3.2	Calculated RF Gun Field Profiles on Axis for Various Cathode Positions . . .	42
3.3	Measured Resonant Frequency Dependence on Gun Temperature	43
3.4	Measured Perturbation Induced by Optical Fiber	44
3.5	Inferred Field Profile on Axis for Various Bead Sizes	45
3.6	Comparison of Calculated and Measured on Axis Field Profile	45
3.7	Measurement of Field Balance Dependence on Gun Temperature	47
3.8	Measurement and Calculation of Field Balance Dependence on Cathode Position	49
3.9	Measurement and Calculation of Field Balance Dependence on Resonant	

Frequency	50
3.10 Measurement and Calculation of Q Dependence on Field Balance	51
3.11 Calculation of Difference Frequency Dependence on Field Balance	52
3.12 Photoinjector Drive Laser Schematic	53
3.13 Measurements of Mode Locked Oscillator Output	54
3.14 Pulse Compression Setup and Output	55
3.15 Regenerative Amplifier Schematic	56
3.16 Measurement of Regenerative Amplifier Performance	56
3.17 Streak of Amplified and Compressed Laser Pulse	57
3.18 RF and Timing System Schematic	60
3.19 Diagnostic Beamline Schematic	63
3.20 Laser Injection Geometry	67
3.21 Measurement of Charge as a Function of Laser Energy for an Unbalanced RF Gun	68
3.22 Measurement of Charge as a Function of Incident Polarization for 70° Laser Injection	70
3.23 Measurement of Charge as a Function of Laser Energy for a Balanced RF Gun	71
3.24 Measurement of QE as a Function of RF Power Coupled to the Gun	72
3.25 Measurement of QE as a Function of Field Gradient	72
3.26 Measurement and Simulation of Charge as a Function of Laser Injection Phase	73
3.27 Cherenkov Radiator Setup	78
3.28 Cherenkov Streak Measurement of the Electron Beam	79

3.29	Streak Measurement of Electron Beam with 70° Laser Injection	81
3.30	Streak Measurement of Electron Beam from Undamaged Cathode Area	82
3.31	Streak Measurement of Electron Beam from Damaged Cathode Area	82
3.32	Streak Measurement and Simulation of Electron Beam Generated by 50 ps Laser Pulse	83
3.33	Measurement of Beam Energy as a Function of RF Power in the Gun	86
3.34	Energy and Phase as Functions of Electric Field for Optimal Acceleration . . .	87
3.35	Measurement of Emittance as a Function of Beam Charge	90
3.36	Measurement of Emittance as a Function of Laser Injection Phase	91
3.37	Nonuniform Electron Emission	94
3.38	Damage on Surface of CATH2	96
4.1	Overdense Lens Experimental Beamline	103
4.2	Schematic of the Plasma Source	107
4.3	Radial Plasma Density Profile	108
4.4	Longitudinal Plasma Density Profile	109
4.5	Time Integrated Spot Size Measurements at PM2, 21 cm Downstream of the Plasma Lens	114
4.6	Time Resolved Measurement of the Plasma Focused Electron Beam	117
4.7	Calculated Temporal Wakefield Response	120
4.8	Electric and Magnetic Field Contributions to the Radial Wakefield	121
4.9	Measured Beam Envelope with Plasma Off	123
4.10	Comparison of the Wakefield Calculation of Dynamic Focusing with the Measurement	124
4.11	Comparison of the Wakefield Calculated Beam Profile and the	

Measurement at PM2	125
4.12 Measured and Calculated Beam Envelope with Plasma On	126
4.13 Spot Size at PM2 as a Function of Beam Charge	127
4.14 Simulated, Calculated and Measured Beam Envelope with Plasma Off	130
4.15 Simulation, Calculation and Measurement of Dynamic Focusing from the Plasma Lens	131
4.16 Simulated, Calculated and Measured Beam Profile at PM2	132
4.17 Simulated, Calculated and Measured Beam Envelope with the Plasma On . . .	133

Acknowledgments

First, I would like to acknowledge the help of Garnick Hairapetian and thank him. It is with his collaboration that the experiments and analysis were performed and through our daily interaction that my understanding of electron beams and plasmas has grown. Next, I would like to thank my advisor, Professor Chan Joshi, for his guidance and encouragement throughout my graduate career. He provided the expertise, resources and motivation which made this project successful. I would also like to thank Professor Claudio Pellegrini for the opportunity to develop and use the Particle Beam Physics Laboratory and for his support of the electron beam and plasma experiments. Throughout my years of study at UCLA I have received excellent support from my fellow graduate students, undergraduate assistants, facilities personnel, engineering staff and administrators. I would like to thank them all for their assistance and friendship. Finally, I owe my deepest thanks and appreciation to Carol for her support and encouragement and for proof reading this entire dissertation.

VITA

May 28, 1967 Born, San Francisco, California

1989 B.S., Engineering Physics
 University of California, Berkeley

1989-1993 ATRI Fellowship

1993 M.S., Electrical Engineering
 University of California, Los Angeles

1993-1996 Graduate Research Assistant
 Department of Electrical Engineering
 University of California, Los Angeles

PUBLICATIONS

P. Davis, G. Hairapetian, M. Hogan, C. Joshi, M. Lampel, S. Park, C. Pellegrini, J. Rosenzweig, G. Travish and R. Zhang, "The UCLA Compact High Brightness Electron

Accelerator", Proceedings of the 1995 Particle Accelerator Conference, Dallas, TX, USA, 1-5 May 1995

G.Hairapetian, **P. Davis**, C.E.Clayton, C.Joshi, C. Pellegrini and T. Katsouleas, "Transverse Dynamics of a Short, Relativistic Electron Bunch in a Plasma Lens", Physics of Plasmas, June 1995, vol.2, (no.6, pt.2):2555-61.

G. Hairapetian, **P. Davis**, C.E. Clayton, C. Joshi, S. Hartman, C. Pellegrini and T. Katsouleas, "Experimental Demonstration of Dynamic Focusing of a Relativistic Electron Bunch by an Overdense Plasma Lens", Physical Review Letters, 11 April 1994, vol.72, (no.15):2403-6.

R. Brogle, P. Muggli, **P. Davis**, G. Hairapetian and C. Joshi, "Studies of Linear and Nonlinear Photoelectric Emission for Advanced Accelerator Applications", Proceedings of the 1995 Particle Accelerator Conference, Dallas, TX, USA, 1-5 May 1995

S.C.Hartman, N.Barov, C. Pellegrini, S. Park, J. Rosenzweig, G. Travish R. Zhang, C. Clayton, **P. Davis**, M. Everett, C. Joshi and G. Hairapetian, "Initial Measurements of the UCLA RF Photo-Injector", Nuclear Instruments & Methods in Physics Research, Section A, 11 Feb. 1994, vol.340, (no.1):219-30.

P. Davis, G. Hairapetian, C. Clayton, C. Joshi, S. Hartman, S. Park, C. Pellegrini, J. Rosenzweig, "Quantum Efficiency Measurements of a Copper Photocathode in an RF Electron Gun", Proceedings of the 1993 Particle Accelerator Conference, Washington,

DC, USA, 17-20 May 1993, p. 2976-8 vol.4.

G. Hairapetian, **P. Davis**, M. Everett, C. Clayton, C. Joshi, S. Hartman, S. Park and C. Pellegrini, "Streak Camera Measurements of Electron Bunch Length from a Copper Photocathode in an RF Gun", Proceedings of the 1993 Particle Accelerator Conference, Washington, DC, USA, 17-20 May 1993, p. 3003-5 vol.4.

G. Hairapetian, **P.Davis**, C.E. Clayton, C. Joshi, S. Hartman, C. Pellegrini and T. Katsouleas, "Experimental Demonstration of Plasma Lens Focusing", Proceedings of the 1993 Particle, Washington, DC, USA, 17-20 May 1993, p.3543-5 vol.5.

P.G. Davis, G. Hairapetian, C. Joshi, N.C. Luhmann Jr., and others."Design and Operation of a Novel,Compact 20 MeV Linac at UCLA", (Intense Microwave and Particle Beams III, Los Angeles, CA, USA, 20-24 Jan. 1992). Proceedings of the SPIE - The International Society for Optical Engineering, 1992, vol.1629:513-20.

ABSTRACT OF THE DISSERTATION
Plasma Lenses for Relativistic Electron Beams

by

Joseph Grau Davis

Doctor of Philosophy in Electrical Engineering

University of California, Los Angeles, 1996

Professor Chan Joshi, Chair

An overdense plasma lens is fully characterized through experiments, calculations and computer simulations. The development of an electron beam source for performing the plasma lens experiments is described. A laser-driven rf photoinjector was used to produce a 3.5 MeV electron bunch containing up to 7 nC with a pulse duration of < 25 ps FWHM. Up to 0.6 nC was used to characterize the overdense plasma lens.

In characterizing the plasma lens, both time-integrated and time-resolved measurements of the electron beam spot size were performed. With the time-integrated measurements, a factor of 4 reduction in spot size was observed, from 2.4 mm FWHM to 0.55 mm FWHM, at the best focus, 21 cm downstream of the plasma. Time-resolved measurements demonstrated the dynamic focusing produced by the overdense plasma

lens. The temporal dependence of the beam profile indicated that the head of the electron beam was not affected by the plasma while the rest of the beam was focused by various amounts. The minimum spot size occurred 35 ps from the head of the beam, in reasonable agreement with the plasma response time, $1/\omega_p$, for the measured plasma density of $4 \times 10^{12} \text{ cm}^{-3}$.

The experimental results are compared with analytical calculations and computer simulations. The analytical calculations are based on two-dimensional wakefield theory while the computer simulations were performed with a PIC code. Good agreement was achieved between the measured, calculated and simulated results for both time-integrated and time-resolved characteristics. From this analysis, it was determined that the plasma lens focusing force consisted of both radial electric field and azimuthal magnetic field contributions, and due to the characteristic ≈ 7 ps risetime of the electron bunch produced by the photoinjector, the maximum focusing force constituted 60% radial electric field and 40% azimuthal magnetic field.

Chapter 1

Introduction

One of the figures of merit for electron beam colliders is luminosity. Luminosity is a measure of the inherent ability of a colliding-beam system to produce reactions [1] and is defined as:

$$\mathcal{L} = \frac{f_{rep} N^2 H_D}{4\pi\sigma_0^{*2}} \quad (1)$$

where f_{rep} is the accelerator repetition rate, N is the number of electrons per bunch, H_D is the beam-beam disruption enhancement factor and σ_0^* is the rms beam radius at the focus [2]. Because of the statistical nature of high energy electron beam collider experiments, the luminosity per second along with the reaction cross section define the probability that a particular reaction can be measured and therefore the luminosity is a critical parameter in every experiment. As electron beams are accelerated to higher energies in order to probe smaller distances, the reaction cross section decreases approximately as:

$$\sigma_i \approx 10^{-37} E^{*-2} R_i \quad (\text{cm}^2) \quad (2)$$

where E^* is the center of mass energy in TeV and R_i is the ratio of the cross section for the process i divided by the cross section for the mu pair production through the

electromagnetic interaction only [3]. Based on this scaling of the cross section, in order to maintain a measurable number of events (yield of 100 events per 10^7 seconds) the luminosity must scale with the center of mass energy as:

$$\mathcal{L} = 10^{33} \left(\frac{E^*}{3} \right)^2 (\text{cm}^{-2} \text{s}^{-1}) \quad (3)$$

where E^* is again the center of mass energy in TeV and $R_i \approx 1$, corresponding to the ratio for mu pair production [3]. Therefore, for future colliders there is a need to increase the beam luminosity at the interaction point. One way to increase the luminosity is by reducing the spot size at the interaction point. This is accomplished through strong focusing of the beam. The minimum spot size is limited by the magnetic gradients of conventional quadrupole magnets (< 25 kG/cm), geometric and chromatic errors in thick quadrupole lenses, and complicated focusing lattices used to focus the electron and positron beams [4]. In order to reduce the spot sizes further, a simpler and stronger focusing lens is necessary. It was suggested by Katsouleas [5] and Chen [6] that a plasma lens could provide extremely strong focusing in a single lens and therefore produce large enhancements in the luminosity.

Plasmas have been used for focusing or guiding charged particle beams since 1922 [7]. There are three basic types of plasma lenses, the electrostatic lens, the "active" lens and the "passive" lens. The electrostatic lens classification applies to plasma lenses whose focusing properties are derived from electrostatic fields maintained in a quasi-neutral or non-neutral plasma. These fields are either ambipolar radial electric fields which are created by electron beam ionization of a neutral gas [8] or Coulomb fields in a pure electron plasma [9]. The first observations of plasma focusing can be characterized

as electrostatic lenses. In the 1920's and 1930's several researchers experimented with the propagation of electron beams through various gasses [10]. They observed that a low voltage (< 100 kV) electron beam passing through a gas will ionize the gas thereby creating a plasma in the vicinity of the electron beam. The plasma electrons have larger thermal velocities than the plasma ions and therefore escape from the region within the electron beam at a faster rate than the ions, creating an ambipolar electric field which focuses the electron beam [8]. This effect was termed "gas focussing" or "ion focussing" [8]. Since the maximum potential is of the order of the plasma electron temperature (< 10 eV), the focusing force is weak and not particularly useful for relativistic electron beams. The second type of electrostatic lens was proposed by Gabor in 1947 [9]. He proposed the use of a pure electron plasma for focusing ion beams. A uniform density electron plasma provides a linear radial electric field ideal for focusing ion beams proportional to the electron plasma density. However, uniform electron plasma densities are difficult to achieve and even at densities of 10^{11} cm⁻³ the focusing strength of the Gabor lens is only 300 G/cm [11]. Finally, in order to make a Gabor lens for an electron beam, either a pure ion plasma or positron plasma is required. Unfortunately, because of the large mass of ions, the magnetic field required to confine the ion plasma is greater than 2 T. Such a strong magnetic field could be used to directly focus the electron beam with greater efficiency [12]. As far as a pure positron plasma is concerned, it is extremely difficult to produce such a plasma [13] and, therefore, the use of a positron plasma is not a practical solution for focusing relativistic electron beams [11].

The second type of plasma lens is the "active" lens [11]. This type of lens was first demonstrated by Panofsky and Baker in 1950 [14]. In the "active" plasma lens, a plasma is used as a conduit through which a large electric current is passed parallel to the charged

particle beam. The azimuthal magnetic field associated with the uniform externally driven current in the plasma provides a linear focusing gradient proportional to the externally driven current. The "active" lens can be used for focusing either ion or electron beams by simply reversing the direction of the externally driven current. However, "active" lenses have only found use in focusing ion beams when large gradients (> 20 kG/cm) and large apertures (≈ 2 cm) are required or when compact symmetric focusing is required [15][16][17]. Since these "active" lenses only produce focusing gradients which are comparable with quadrupole magnets, they have not been used to focus electron beams. More recently, an "active" lens for relativistic electron beams was proposed in which an electron bunch, with larger charge and peak current than the bunch which is to be focused, is injected into a plasma just ahead of the electron bunch to be focused [18][19]. For the appropriate choice of plasma density, large wakefields will be generated in the plasma by the drive electron bunch or laser pulse. These wakefields contain large radial electric fields [19][5] which will then act to focus the trailing electron bunch if properly phased. Although such wakefields have been observed in a plasma [20], plasma lenses of this type have not been tested because of the realization that the drive bunch used to generate the wakefields will self-focus from its own magnetic field and wakefield [5].

In contrast with the electrostatic and the "active" plasma lens, the "passive" lens consists of a pre-formed, current-free and neutral plasma [11]. Upon entry of the charged particle beam, this plasma responds by movement of the plasma electrons in an attempt to maintain charge and current neutrality. The mechanism of the "passive" plasma lens was first illustrated by Bennett in 1934 [21]. Bennett showed that an electron beam propagating through a plasma could be charge neutralized without neutralizing the self-magnetic field, and if the current is large enough, the beam will self

pinch. Typically, in order for the focusing force to be large enough to overcome the beam emittance force, the electron beam must be relativistic. The concept of a "passive" plasma lens for relativistic electron beams was first proposed by Katsouleas while analyzing the physical mechanisms of a plasma wake-field accelerator [5]. The initial analytical calculations were performed in the overdense regime where the plasma density is larger than the beam density [6][22]. In this regime the electron beam perturbations on the plasma are linear and therefore can be solved analytically. However, focusing can also occur in the underdense regime where the plasma density is less than the beam density. In this case the plasma response becomes nonlinear and must be modeled with particle simulations [23]. Positron beams can also be focused with a "passive" plasma lens. In the overdense regime, the plasma response to a positron beam produces focusing forces that are identical to those produced by an electron beam. However, in the underdense regime, although positrons can experience a net focusing force, the focusing force for a positron beam is dissimilar to that of an electron beam due to the nonlinear plasma response, and based on particle simulations, the underdense plasma lens for positron beams is inferior to the overdense lens [23]. Both the overdense and underdense regimes offer excellent possibilities as "passive" plasma lenses for relativistic electron beams.

In comparison with quadrupole lenses, the "passive" plasma lens offers three major advantages. First, the "passive" lens is capable of producing focusing gradients up to 300 MG/cm [23] which is orders of magnitude larger than that of conventional quadrupole magnets. Secondly, it results in symmetric focusing as opposed to the focusing in one plane and defocusing in the orthogonal plane produced by quadrupole magnets. And finally, the plasma lens is a compact device, typically < 1 m in length,

whereas quadrupole magnets, which must be used in pairs and typically require complicated beam lines for optimum focusing, employ lattices > 10 m in length. However, there are some major disadvantages to "passive" plasma lenses. The most obvious disadvantage is that a plasma requires a certain amount of gas in the vacuum system of the accelerator depending on the density required and lens thickness required. This is particularly problematic at the final focus where the background gas can interfere with the measurements of the collider experiments. Since the object of the plasma lens is to focus the beam strongly, the focal length is necessarily short and therefore the plasma is very close to the interaction point and difficult to isolate. Furthermore, besides the background gas problem, which might be reduced by differential pumping or a vacuum window, "passive" lenses are subject to severe spatial and temporal aberrations, since the beam itself is used to generate the focusing effect. The severity of these aberrations depends on the lens design and the beam characteristics. Finally, it has been proposed that a plasma lens could be tailored to produce adiabatic focusing which would result in spot sizes which are smaller than the Oide limit [24]. The adiabatic lens is technically difficult to build and experimental verification of simpler plasma focusing schemes should be performed before attempting an adiabatic lens.

The first experimental demonstration of "passive" plasma lens focusing was in 1965 [25]. This experiment was actually a relativistic version of electrostatic lens experiments. A 2.5 MeV electron stream generated a plasma while propagating through a gas. The plasma then acted to shield the beams space charge field leaving the self-magnetic field to pinch the beam. Although Bennett's theory was confirmed, the beam and plasma characteristics were very different than those of beams in a linear collider. The first experiment which addressed plasma lens focusing for future colliders was performed at

Argonne National Laboratory in 1989 [26]. In this experiment a 21 MeV electron bunch ($\sigma_z = 2.1$ mm, $\sigma_r = 1.4$ mm) with 5 nC of charge was pinched to its Bennet equilibrium radius in an Argon plasma. The spot size of the electron beam was monitored at the edge of the plasma and a factor of 2 reduction in the spot size at that position was observed when the plasma was on. The plasma column was 35 cm long however the calculated focal length of the lens was only 8 cm, therefore, this constituted a thick lens (focal length \leq plasma length) whose output radius matched the Bennet equilibrium radius. Time resolved measurements were also made using a Cherenkov cell and a streak camera, but they did not reveal the dynamic nature of the pinching mechanism. Although significant focusing was observed, a thick lens is not practical for final focus applications since it places the plasma at the focal spot. In 1991 a thin plasma lens was demonstrated at Tokyo University [27]. An electron bunch ($\sigma_z = 3$ mm) with 0.5 nC of charge was focused by an Argon plasma. The plasma length was 20 cm while the focal length of the plasma lens was > 1 m and therefore a thin lens. Since the focal length was quite long, only a 20% reduction in the 2.5 mm spot size was observed at the 1.3 m position from the plasma. Although these experiments confirmed the plasma lens effect, an experiment showing the dynamic focusing of a thin plasma lens that could be compared with the wakefield theory for plasma focusing was still needed.

In 1994, an experiment which demonstrated the dynamic focusing of a thin plasma lens was completed at UCLA [28][29]. This experiment used an overdense argon plasma to focus a 3.8 MeV electron bunch (7.5 mm FWHM) containing .6 nC of charge. The plasma was 8 cm long and the focal length was 21 cm, therefore constituting a thin lens. A factor of 4 reduction in spot size was observed in both time integrated and time resolved measurements. For the first time the dynamic focusing properties of a thin

overdense plasma lens were observed and compared with wakefield calculations and computer simulations.

This dissertation describes in detail the preparations and results of the UCLA experiment. In Chapter 2, the theoretical background necessary to understand and analyze the plasma lens results is reviewed. Emphasis is placed on the overdense plasma lens since this is the regime covered by the experiment. From the theory, estimates of the plasma density and the electron beam parameters required to observe dynamic focusing with the available diagnostics, are calculated. Chapter 3 then describes the development of an electron beam source which matches these requirements. Finally, in Chapter 4, the overdense plasma lens experiment and results are described including the plasma source and electron beam diagnostics. The experiment is then analyzed using the wakefield theory described in Chapter 2 and computer simulations. Although this experiment demonstrated dynamic focusing of a thin plasma lens, it only addressed the overdense lens regime. A similar experiment in the underdense regime should be performed in order to complete the experimental verification of "passive" plasma lens theory (particularly for the underdense case where analytic calculations cannot be performed without loss of generality). Finally, a plasma lens experiment using an electron beam with energies and densities like those in linear colliders should be performed. Such an experiment has been proposed for the Final Focus Test Beam at the Stanford Linear Accelerator Center and currently preliminary design and development of a plasma source are under way [30].

Chapter 2

Theory of "Passive" Plasma Lenses

2.1 Introduction

The "passive" plasma lens mechanism was first proposed by Bennet as "Magnetically Self-Focussing Streams" in 1934 [21]. In this first description of magnetic self-focusing, a uniform density electron stream is assumed to be in equilibrium with a uniform density of ions and the equilibrium radius of the electron stream is calculated. An understanding of the dynamics through which this equilibrium is achieved was not accomplished until 1970 when Cox and Bennett examined the penetration of a relativistic electron beam through a high density ($n_p > 10^{16} \text{ cm}^{-3}$) plasma [31]. Although the focusing mechanism had been described, the possibility for strong focusing of a relativistic electron beam was not realized until 1986. Katsouleas, while investigating the two-dimensional dynamics of the plasma wakefield accelerator [32], was first to recognize the strong focusing in a "passive" plasma lens [5] while Chen [6] and Ruth [19] produced the first analytical description of the two-dimensional dynamics. These initial works led to a serious investigation of "passive" plasma lenses by various

researchers and resulted in an excellent understanding of both the overdense and underdense regime [23]. The simple physical model presented in Section 2.2 summarizes the basic principles behind both the overdense and underdense "passive" plasma lenses while Sections 2.3 and 2.4 describe analytic and particle simulation models for analyzing the overdense plasma lens experiment.

2.2 Simple Physical Model

Since the "passive" plasma lens derives its focusing from the self-fields of the electron bunch, first consider a cylindrically symmetric electron bunch of uniform density propagating in vacuum near the speed of light as shown in Fig. 2.1. Due to the Coulomb repulsion between electrons, the electrons within the bunch experience a radial electric

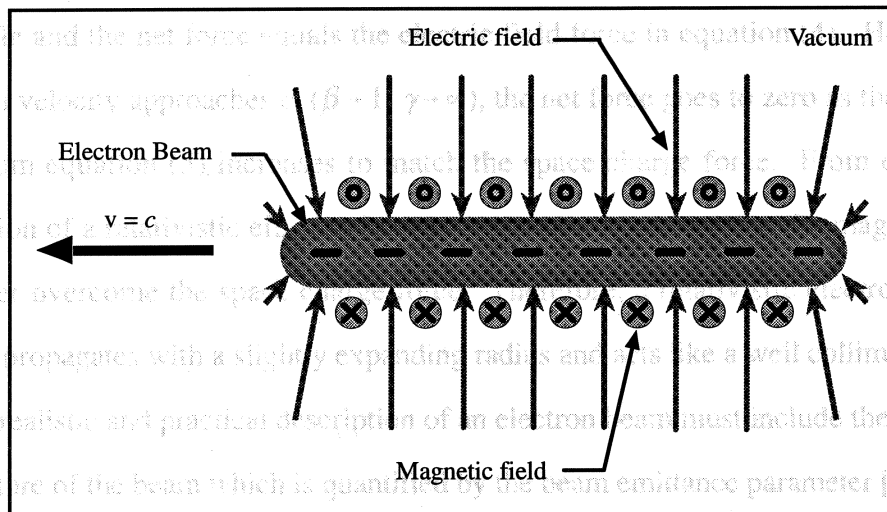


Figure 2.1: Electron Beam in Vacuum

field acting to push the bunch apart. This force is easily calculated using Gauss's law:

$$\vec{F}_{sc}(r) = 2\pi n_b e^2 r \hat{r} \quad (4)$$

where n_b is the beam density and e is the electron charge. Because the bunch is moving, the moving charges generate a magnetic field in the azimuthal direction which tends to counteract the space charge force and holds the electrons together. The magnetic field is determined using Ampere's law and the magnetic force on the electrons within the bunch is then calculated from the Lorentz force:

$$\vec{F}_{mag}(r) = -2\pi n_b e^2 \beta^2 r \hat{r} \quad (5)$$

where $\beta = v/c$. Combining these forces yields the net force on the electrons at any given radius r :

$$\vec{F}_{net}(r) = \frac{2\pi n_b e^2 r}{\gamma^2} \hat{r} \quad (6)$$

where $\gamma = 1/(1 - \beta^2)$. For low velocity beams ($\beta \approx 0$, $\gamma \approx 1$) the magnetic field is negligible and the net force equals the electric field force in equation (4). However, as the beam velocity approaches c ($\beta \rightarrow 1$, $\gamma \rightarrow \infty$), the net force goes to zero as the magnetic force from equation (5) increases to match the space charge force. From this simple description of a relativistic electron bunch in vacuum, it is clear that the magnetic force can never overcome the space charge force. Therefore, a relativistic electron beam in vacuum propagates with a slightly expanding radius and acts like a well collimated beam. A more realistic and practical description of an electron beam must include the transverse temperature of the beam which is quantified by the beam emittance parameter [33]. Since the net electromagnetic force on a relativistic electron beam is essentially zero, relativistic electron beams expand according to the beam emittance.

In developing a simple physical picture of the "passive" plasma lens, some simplifying assumptions are made so that a steady state solution can be derived easily. First, assume the transverse temperature or the electron beam emittance is zero and that the beam velocity is c . Therefore, a relativistic electron beam in vacuum propagates with a constant radius. Second, assume the electron bunch is long compared to the response time of the plasma and that any variations within the electron bunch are slow compared with the plasma response time. The response of the plasma is dictated by the mobility of the electrons and is therefore inversely proportional to the plasma frequency, $\omega_p \equiv \sqrt{4\pi n_p e^2 / m_e}$, where n_p is the plasma density and m_e is the electron mass. Finally, assume the plasma ions have infinite mass and therefore are immobile as the electron beam passes through the plasma. With these assumptions a simple description of the "passive" plasma lens is easily derived and order of magnitude calculations of lens properties can be computed.

The "passive" plasma lens consists of a pre-formed, current free and neutral plasma of thickness L along the electron beam path. For simplicity, assume the transverse extent of the plasma is infinite and the plasma density is uniform throughout. Since this is to be a thin lens, the plasma thickness must be less than the focal length of the lens therefore $L \ll f$. There are two regimes in which the "passive" plasma lens can operate, the overdense regime ($n_p \gg n_b$) and the underdense regime ($n_p \leq n_b$).

In the overdense regime, the electron beam acts as a small perturbation on the plasma. Since the beam rise time and length are long compared to ω_p , the plasma responds adiabatically to the electron beam. Locally, within the electron beam, the plasma electrons are expelled in order to preserve the charge neutrality in the presence of the beam electrons. Because of the electron inertia, the plasma electrons require a time

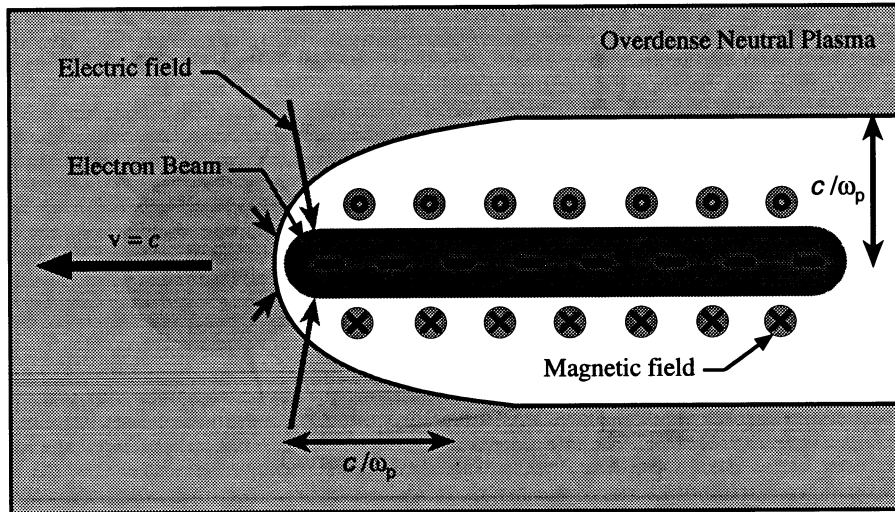


Figure 2.2: Electron Beam in an Overdense Plasma

$t \approx 1 / \omega_p$ to respond to the electron beam. Therefore, the head of the electron bunch acts to expel the plasma electrons so that the bulk and tail of the electron bunch are fully charge neutralized as depicted in Fig. 2.2. The plasma electrons also act to current neutralize the beam, however, the plasma return currents exist in a channel of radius c / ω_p , the characteristic plasma scale length. The net return current equals the electron beam current thus preserving current neutrality in the plasma, but locally (in the vicinity of the electron beam) full current neutralization can only occur if $\sigma_r > c / \omega_p$ where σ_r is the beam radius. As shown in Fig. 2.3, although the plasma return current is peaked on axis, if $\sigma_r < c / \omega_p$ only partial current neutralization of the electron beam is achieved. Because full space charge neutralization has been achieved but only partial current neutralization, the beam's self-magnetic force can now overcome the space charge force and the beam will self-focus. For simplicity, consider the case when $\sigma_r \ll c / \omega_p$ so that the plasma return currents within the electron beam are negligible. Therefore, the full vacuum magnetic field acts to pinch the beam. The magnetic gradient is calculated from

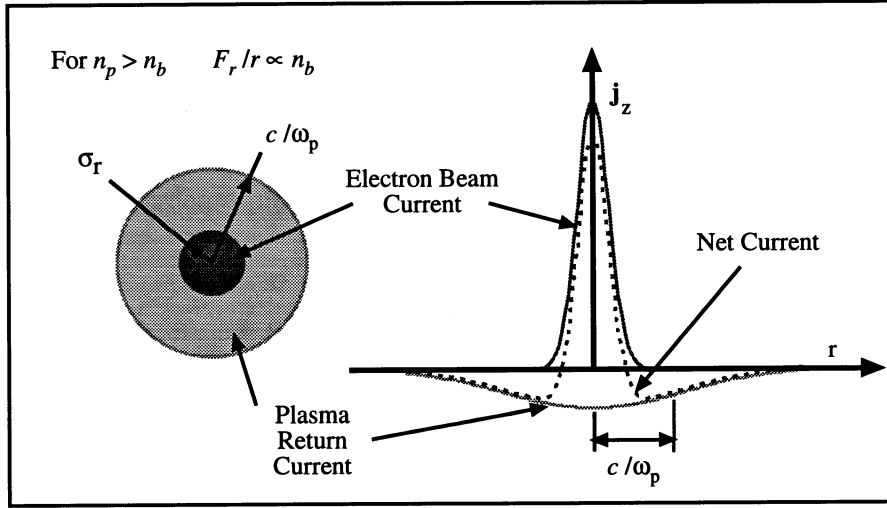


Figure 2.3: Return Current in an Overdense Plasma

Ampere's law to be:

$$\frac{B_\theta}{r} = 2\pi n_b e = 3 \times 10^{-9} n_b [\text{cm}^{-3}] \text{ G/cm [23].} \quad (7)$$

For a thin lens, the focal length can be calculated assuming a parallel beam receives a transverse kick upon passing through the thin plasma lens. The transverse momentum acquired from the plasma lens is approximated from the magnetic force calculated in equation (5):

$$F_{\text{overdense}} = F_{\text{mag}\perp} = \frac{\Delta P_\perp}{\Delta t} = -2\pi n_b e^2 \beta^2 r, \quad (8)$$

but since the electron beam is propagating at c , $\beta = 1$ and $\Delta t \approx L/c$ therefore,

$$\Delta P_\perp \approx \frac{-2\pi n_b e^2 rL}{c}. \quad (9)$$

The ratio of the focal length to radial position at the lens is equal to the ratio of

longitudinal beam momentum to transverse beam momentum [23], or:

$$\frac{f}{r} = \left| \frac{P_{\parallel}}{\Delta P_{\perp}} \right| = \left| \frac{\gamma m_e c}{-2\pi n_b e^2 r L / c} \right|. \quad (10)$$

Therefore, for the overdense plasma lens:

$$f = \frac{2\gamma c^2}{L \omega_b^2} = 5.6 \times 10^{11} \frac{\gamma}{L[\text{cm}] n_b[\text{cm}^{-3}]} \text{ cm}, \quad (11)$$

where $\omega_b \equiv \sqrt{4\pi n_b e^2 / m_e}$ [11]. Since the plasma fully space charge neutralizes the electron bunch, the focusing forces and therefore focal properties, such as focal length, depend on the electron beam density and density profile. This has major implications for lens aberrations which will be discussed later, but first compare the overdense lens with the underdense lens.

In the case of the underdense plasma lens, again consider a pre-formed, current free and neutral plasma only this time $n_p \leq n_b$. The plasma electrons again move away from the electron beam in an attempt to maintain the charge neutrality of the plasma with the addition of the electron beam as shown in Fig. 2.4. However, since $n_p \leq n_b$, even when all of the plasma electrons are expelled from the beam region, the plasma ion density is not large enough to fully space charge neutralize the electron beam and therefore the amount of space charge neutralization from the underdense plasma is calculated from the Coulomb force produced by the ion channel:

$$\vec{F}_{ions}(r) = -2\pi n_p e^2 r \hat{r} \quad (12)$$

where n_p is the plasma density since the ion density equals the plasma density assuming the ions are immobile [23]. Due to the plasma electron inertia, the plasma response time

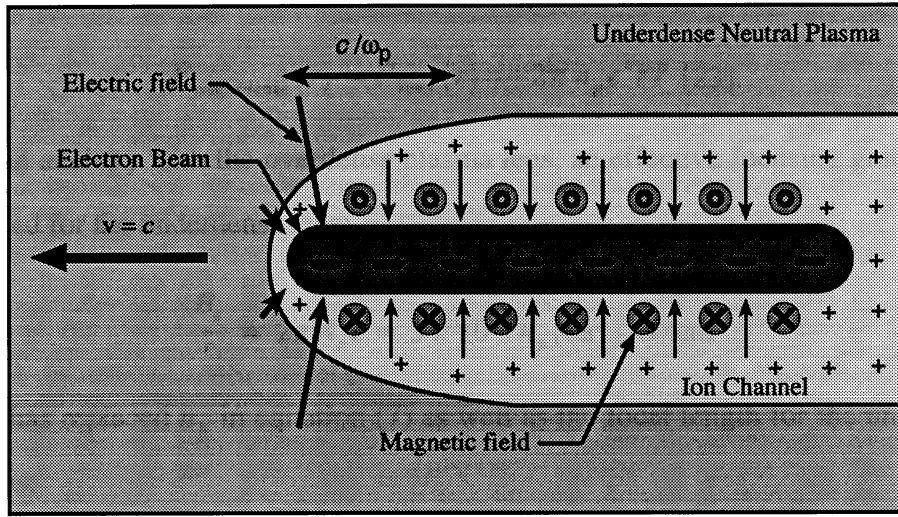


Figure 2.4: Electron Beam in an Underdense Plasma

is at least $1 / \omega_p$, before the pure ion channel is formed and could be longer depending on the electron beam radius over which the plasma electrons must be expelled. It is important to note that since all of the plasma electrons within the electron beam channel have been expelled, there are no plasma electrons left to create a return current within the electron beam channel. Therefore, all the plasma return currents exist outside of the beam channel and the beam's self magnetic field is not reduced within the ion channel. Once the ion channel is formed, the focusing force on the electron bunch can be calculated in the same manner which was used for the overdense lens. Consider the net force on the electron bunch by adding the space charge force from equation (4), the magnetic force from equation (5) and the focusing force due to the ion channel from equation (12):

$$\vec{F}_{underdense}(r) = 2\pi n_b e^2 r \hat{r} - 2\pi n_b e^2 \beta^2 r \hat{r} - 2\pi n_p e^2 r \hat{r}. \quad (13)$$

Assuming the beam velocity is c , as was done in the overdense case, $\beta \rightarrow 1$ and the beam's space charge and self-magnetic fields cancel leaving only the force from the

uniform ion channel:

$$\vec{F}_{\text{underdense}}(r) = \vec{F}_{\text{ions}}(r) = -2\pi n_p e^2 r \hat{r} \quad [23]. \quad (14)$$

Drawing an analogy with the overdense plasma lens, an effective focusing gradient can be computed for the underdense lens:

$$\frac{B_\theta}{r} = 2\pi n_p e = 3 \times 10^{-9} n_p [\text{cm}^{-3}] \text{ G/cm} \quad (15)$$

where n_p has replaced n_b in equation (7) as well as the focal length for the underdense plasma lens:

$$f = \frac{2\gamma^2}{L \omega_p^2} = 5.6 \times 10^{11} \frac{\gamma}{L [\text{cm}] n_p [\text{cm}^{-3}]} \text{ cm}. \quad (16)$$

where ω_p has replaced ω_b in equation (11) [11].

From these simple physical descriptions of the overdense and the underdense plasma lenses, a qualitative understanding and a comparison between these lenses can be achieved. First consider the temporal aberrations of these "passive" plasma lenses. Both the overdense and the underdense lenses require a minimum time equal to $1 / \omega_p$ in order to respond to the electron bunch. Therefore, in both cases, the head of the beam remains unfocused while the plasma space charge neutralization is setup. In the overdense lens, additional temporal aberrations are created which depend on the longitudinal profile of the electron bunch [23]. From equations (7) and (11) it is clear that both the focusing gradient and the focal length depend on the beam density. Therefore, if the electron beam density varies in time, so will the focusing gradient and the focal length. For a typical Gaussian profile the focusing force will be strongest in the center of the bunch and therefore that portion will focus closest to the plasma and result in the smallest spot size

while the head and tail of the beam will experience weaker focusing depending on the beam current and therefore focus further from the plasma. On the other hand, for the underdense lens, the focusing gradient and the focal length, from equations (15) and (16), are dependent only on the plasma density. Therefore, as long as the plasma density does not vary in time, then the focusing gradient and the focal length likewise will be time independent. In the above calculations, the ions were assumed to be immobile which is a good assumption for Argon ions and times less than 300 ps. Therefore, the time aberrations for the underdense lens, except for the $1/\omega_p$ response time at the head of the bunch, should be negligible for electron bunches shorter than 300 ps. These same equations lend some insight into the spatial aberrations produced by these plasma lenses. Although it was assumed in the simple calculations for the overdense lens that the transverse profile of the electron beam was uniform, equations (7) and (11) remain true for an arbitrary profile if the uniform beam density, n_b , is replaced with the actual profile, $n_b(r)$. Therefore, the overdense plasma lens also suffers from severe spherical aberrations depending on the beams profile. These aberrations have been discussed by various authors [6][11][23][34] for different profiles with more detailed calculations and have shown that if the beam profile can be tailored properly, then the aberrations can be eliminated [23]. For the underdense plasma lens, the spatial aberrations are very small [23]. Again, since the focusing gradient is a function of the plasma density, as long as the plasma profile is uniform and as long as the electron beam is entirely within the ion channel, the spatial aberrations will be negligible. For a typical beam size, $\sigma_r < 1$ mm, maintaining a uniform transverse plasma profile is easy while keeping the beam within the ion channel will naturally occur if n_b is a few times n_p . Although the overdense lens has greater temporal and spatial aberrations than the underdense lens, because the

focusing force is proportional to n_b rather than n_p , and since by definition of the underdense lens, $n_b > n_p$, the overdense lens provides stronger focusing than the underdense lens for a given electron beam. Also, despite the temporal and spatial aberrations of the overdense lens, significant enhancements in the luminosity at the final focus can still be achieved [23]. Finally, because the overdense lens can be analyzed by treating the beam as a small perturbation on the plasma, detailed analytical calculations for the overdense lens can be performed whereas for the underdense case, the plasma response is extremely non-linear [35] and particle simulations must be performed in order to predict the lens behavior. Therefore, although the underdense lens appears to have many benefits in the simple approximations given above where the rise time of the beam is slow and the plasma response is adiabatic, for realistic beams in future colliders, it is not clear that the underdense lens will outperform the overdense lens.

2.3 Wakefield Model

In order to achieve a better understanding of the overdense plasma lens, a more detailed model of the electron beam and plasma interaction is required. A general analytical description of the electromagnetic fields of the electron beam in the plasma has been achieved by various researchers [6][22][31] by treating the electron beam as a small perturbation on the plasma. The first analysis of the wakefields in a plasma was done by Dawson and Chen [32]. However, their analysis was only one dimensional and does not describe the pinching mechanism of the plasma lens. The fully electromagnetic two-dimensional problem was later analyzed by Chen [6] and Keinigs and Jones [22]. This

model is referred to as the wakefield model and the main results are summarized here. In the analysis, it is assumed that the electron beam is axisymmetric and that the plasma through which the beam travels is cold and uniform and of course overdense compared to the electron beam density. In this model, the beam current is held constant. Therefore, self-pinching within the plasma which would thereby increase the beam current is not included, making this model valid only for a thin lens. The plasma ions are made immobile, which is a good assumption for bunches < 300 ps long. Given the above assumptions, the beam current can be generally described by:

$$\begin{aligned}\vec{J}_b &= \beta c \rho_b (r, z, t) \hat{z} \\ \rho_b (r, z, t) &= -en_b R(r) T\left(\tau \equiv t - \frac{z}{\beta c}\right)\end{aligned}\quad (17)$$

where $\beta = v_b / c$ with v_b equal to the beam velocity and where n_b is the peak beam density with $R(r)$ and $T(\tau)$ are dimensionless profiles in space and time respectively [22]. The wave equations for the electric and magnetic fields in the plasma can then be written in terms of these quantities:

$$\begin{aligned}\left(\nabla^2 - \frac{\omega_p^2}{c^2} - \frac{1}{c^2} \frac{\partial^2}{\partial t^2}\right) \vec{E}(\vec{r}, t) &= \frac{4\pi}{c^2} \frac{\partial}{\partial t} \vec{J}_b + 4\pi \nabla(\rho_p + \rho_b) \\ \left(\nabla^2 - \frac{\omega_p^2}{c^2} - \frac{1}{c^2} \frac{\partial^2}{\partial t^2}\right) \vec{B}(\vec{r}, t) &= -\frac{4\pi}{c^2} \nabla \times \vec{J}_b\end{aligned}\quad (18)$$

and can be solved for any arbitrary beam profile [22]. In solving these equations, only three field components survive:

$$\begin{aligned}
E_z(r, \tau) &= -k_p \omega_p G(r) \int_0^\tau d\tau' T(\tau') \cos[\omega_p(\tau - \tau')] \\
E_r(r, \tau) &= \frac{\partial G(r)}{\partial r} \left[\omega_p \int_0^\tau d\tau' T(\tau') \sin[\omega_p(\tau - \tau')] - T(\tau) \right] \\
B_\theta(r, \tau) &= -\beta \frac{\partial G(r)}{\partial r} T(\tau)
\end{aligned} \tag{19}$$

where

$$G(r) \equiv -4\pi en_b \left[\int_0^r dr' r' R(r') I_0(k_p r') K_0(k_p r) + \int_r^\infty dr' r' R(r') I_0(k_p r) K_0(k_p r') \right] \tag{20}$$

and $k_p = \omega_p / c$ [22]. The transverse components which act to focus or defocus the electron beam can be rewritten as the transverse wakefield [22] which is defined as:

$$\begin{aligned}
W_\perp(r, \tau) &\equiv E_r(r, \tau) - \beta B_\theta(r, \tau) \\
&= \frac{\partial G(r)}{\partial r} \left[\omega_p \int_0^\tau d\tau' T(\tau') \sin[\omega_p(\tau - \tau')] - \frac{T(\tau)}{\gamma^2} \right].
\end{aligned} \tag{21}$$

Equation (21) indicates that the transverse fields produced by an electron bunch in an overdense plasma depend on both the temporal and spatial profile of the electron bunch. Unlike a traditional solenoid or quadrupole lens, the overdense plasma lens properties are dependent on the electron beam properties. However, the spatial and temporal responses are separable and therefore an independent understanding of these dependencies is possible. Assuming the electron beam's time profile, $T(\tau)$, matches that of the electron beam measured experimentally as described in Chapter 3, the temporal profile of the

transverse wakefield:

$$\propto \omega_p \int_0^\tau d\tau' T(\tau') \sin[\omega_p(\tau - \tau')] - \frac{T(\tau)}{\gamma^2} \quad (22)$$

is plotted for various plasma densities in Fig. 2.5. A positive wakefield value

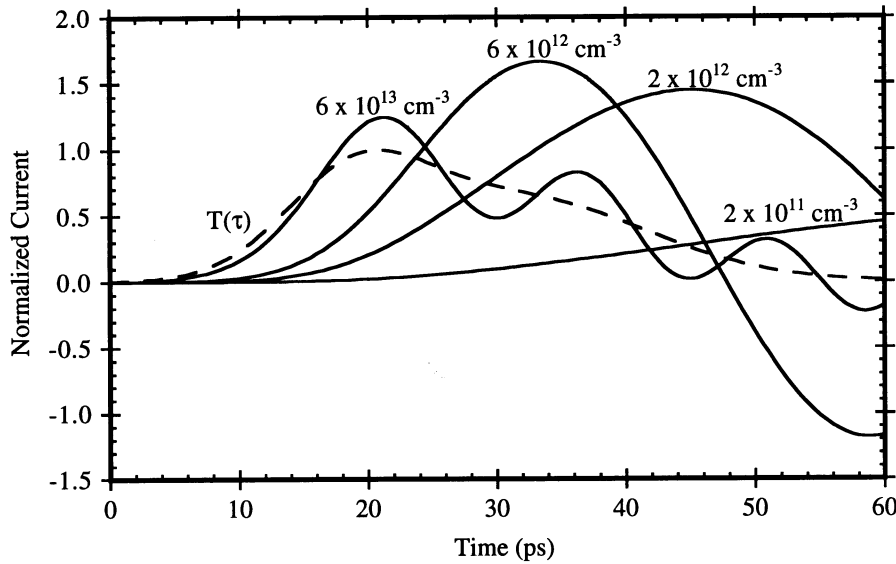


Figure 2.5: Temporal Wakefield Response for Various Plasma Densities

corresponds to a focusing force while a negative value indicates defocusing at a particular time measured from the front of the electron bunch. From Fig. 2.5, it is clear that at low plasma densities, the plasma response is slow since $1/\omega_p$ is long, and the wakefield amplitude is also correspondingly weak. As the density is increased, the response of the plasma is faster and stronger until the plasma response time matches the beam's rise time which occurs around $n_b = 6 \times 10^{12} \text{ cm}^{-3}$. For that density, the wakefield response is maximized but large amplitude plasma oscillations are created which can be seen to defocus the tail of the electron beam and exist for some time in the plasma after the beam

has passed. If the beam density is further increased, the plasma response time continues to decrease so that it can follow the beam profile more closely although ripples at the plasma frequency still exist. In the limit where $\omega_p \rightarrow \infty$ the plasma response matches the beam response as was discussed in the simple physical description of Section 2.3 [11]. However, as the plasma density is increased, the radial profile also changes.

The radial wakefield response, $\propto \partial G(r)/\partial r$, is plotted in Fig. 2.6 assuming a gaussian radial profile. The same values of plasma densities that were used for the plots

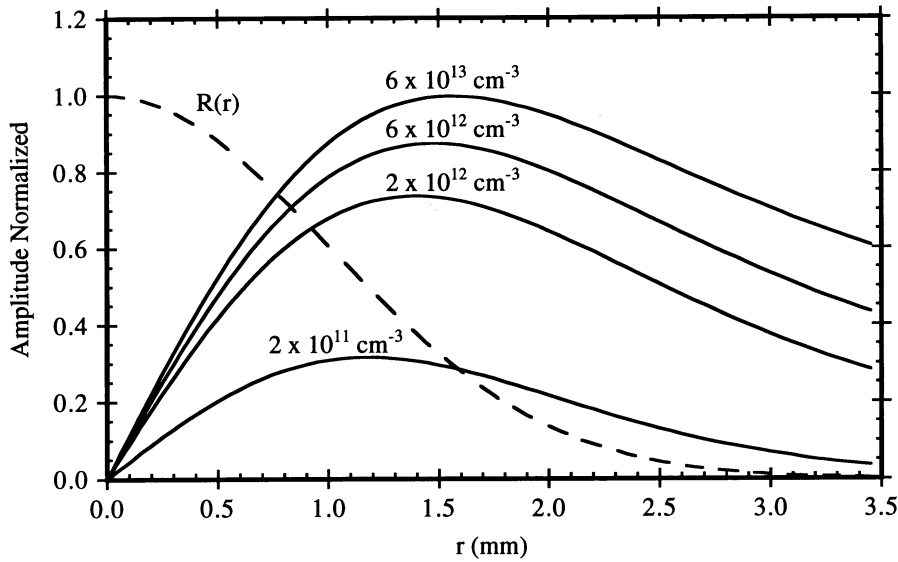


Figure 2.6: Radial Wakefield Response for Various Plasma Densities

of the temporal wakefield response are used in Fig. 2.6. The radial wakefield response is shown to monotonically decrease as the plasma density is increased. Unlike the temporal response, the radial response does not show an enhancement in amplitude at $r \approx c/\omega_p$. The reason for the decrease in wakefield amplitude comes from the return currents which are driven in the plasma. As was described in the simple physical model of Section 2.3 and depicted in Fig. 2.3, the plasma return currents are driven in a channel of radius

$\approx c / \omega_p$. Therefore, as the plasma density is increased, the return current channel radius is decreased and for a given electron beam profile, $R(r)$, the wakefield response is decreased due to current neutralization within the electron bunch. The radial wakefield profile also indicates that for a gaussian beam profile, an overdense plasma lens will always manifest spherical aberrations since the focusing force is not linear over the entire beam. The linearity of the wakefield depends on the plasma density because of the return currents driven in the plasma. At larger plasma densities, the return current profile acts to reduce the wakefields at larger radius more than the wakefields near the axis. This causes a reduction in the linear portion of the focusing field. The wakefield response for three different radial beam profiles was calculated by Su *et al.* [23]. The radial profiles used were uniform, parabolic and gaussian and the aberrations for each were compared with a perfect linear focusing force. Both the parabolic and the gaussian profiles resulted in aberrations that produced weaker than linear focusing at large radii while the uniform beam profile resulted in stronger than linear focusing at large radii. Therefore, it was suggested that an optimum beam profile could be found which eliminates the spherical aberrations of the overdense plasma lens [23]. However, in practice, controlling the beam profile is difficult and for the overdense lens experiment presented in Chapter 4, the measured beam profile was approximately gaussian.

Although the lens aberrations are minimized and the radial wakefield response is maximized at low plasma densities, when multiplied by the temporal profile, a maximum focusing force is produced when the risetime of the electron bunch matches the plasma period. The optimum plasma density will depend on the particular application depending on how much spherical aberration can be tolerated and how long the electron bunch is. Given this analytical model, the focusing force can be calculated for exact beam and

plasma parameters of the overdense plasma lens experiment.

2.4 Simulations

The analytic calculations described by the wakefield theory are limited by the assumption that the beam current and therefore the beam radius does not change while the beam is propagating through the plasma lens. This is a good approximation for a thin lens, however, unless the plasma is infinitely thin, the wakefield model will not completely represent the beam and plasma dynamics. In order to model these beam dynamics selfconsistently as the electron beam propagates through a plasma, particle simulations are used. As an independent analytical tool, particle simulations are used for predicting the behavior of plasma lenses, studying the physical mechanisms in plasma lenses, and analyzing plasma lens experiments. In fact, simulations have been used to verify and make comparisons to the wakefield analytical model since the model was developed. Katsouleas proposed the "passive" plasma lens based on the observation of beam self-pinching in 2-D simulations [5] and later Su *et al.* analyzed both the overdense and underdense lenses for positron and electron beams using a 2-1/2 D simulation code [23].

In the analysis of the overdense plasma lens experiment, MAGIC was used to model the plasma lens [36]. MAGIC is a 2-1/2 dimensional, finite difference, time-domain, fully electromagnetic and relativistic particle-in-cell (PIC) code. Cylindrical geometry with azimuthal symmetry was used in the simulations. The plasma was modeled with immobile ions, which, as mentioned above, was assumed in the simple physical model

and the wakefield calculations and is a valid assumption for simulation time < 300 ps. (MAGIC is capable of modeling the plasma with finite mass ions. Simulations using Argon ions were performed and showed no difference with the infinite mass case.) In representing the plasma, 80,000 electrons and ions were used. The particles are distributed uniformly throughout the plasma space in the simulation. In creating a non-uniform plasma profile, the mass and charge per particle are adjusted rather than the particle distribution.

To verify the simple physical model and to gain some insight into the physics of the plasma lens, two simple simulations were run before using MAGIC to simulate the overdense lens experiment. Using MAGIC, the beam current and the plasma return current can be plotted in two dimensions r , and z . The simplest case to simulate is the adiabatic regime where the rise time of the electron bunch is long compared to the plasma period. In the simulation, the plasma density is $5 \times 10^{12} \text{ cm}^{-3}$ and the rise time of the electron bunch is $50 / \omega_p \approx 400$ ps while the beam length is > 1 ns. A uniform electron beam in the transverse direction is used with a radius equal to $\frac{1}{2} c / \omega_p$. The electron beam energy was set to 1 GeV so that self-pinching would not occur within the plasma lens and therefore a direct comparison to the simple physical model can be made. As shown in Fig. 2.7, the plasma return currents flow mainly outside of the electron beam as predicted in Section 2.2. No plasma oscillations have been excited since the beam's risetime is slow compared to the plasma period. The second simple simulation is performed to gain insight into the return current dynamics when the electron beam rise time is on the order of the plasma period. Again the plasma density is $5 \times 10^{12} \text{ cm}^{-3}$ and the beam radius is equal to $\frac{1}{2} c / \omega_p$, but in this case the electron beam rise time is $1 / \omega_p \approx 8$ ps. Again, a 1 GeV beam energy is used to prevent pinching within the plasma

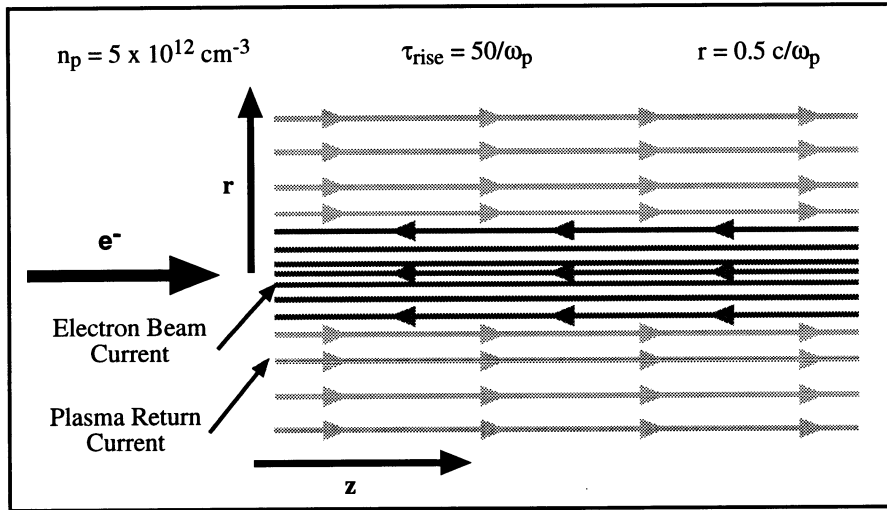


Figure 2.7: Simulation of Adiabatic Return Currents in an Overdense Plasma

lens. As shown in Fig. 2.8, the return currents in this case are much more complicated. Instead of the uniform return current of Fig. 2.7, the return currents vary at the plasma period both within the beam and outside it. The sharp rise time of the electron bunch generates wakefields in the plasma which act on the uniform electron beam which

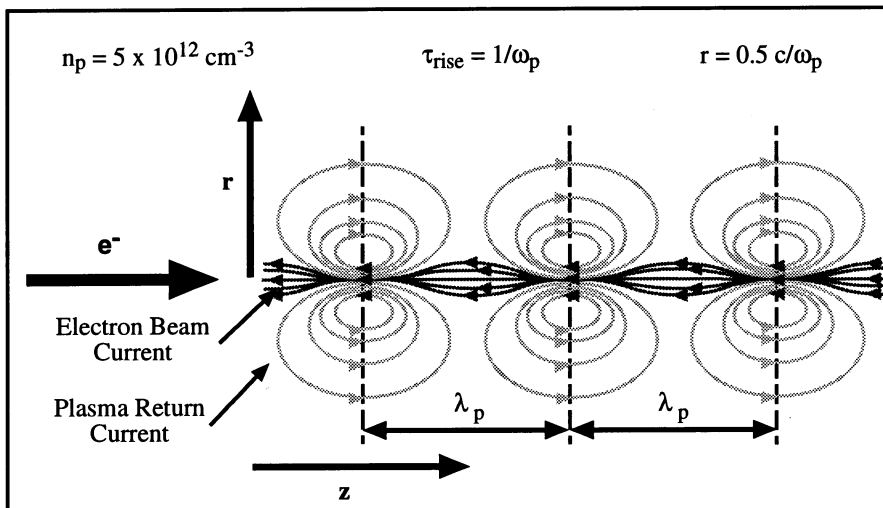


Figure 2.8: Simulation of Wakefield Return Currents in an Overdense Plasma

follows. These are the same wakefields predicted by the wakefield theory.

For the overdense plasma lens experiment, the electron beam was modeled by another particle code rather than creating an ideal beam within MAGIC as was done in the above sample cases. Instead, PARMELA [37] was used to model the electron beam generated by a laser driven rf gun. The PARMELA code calculates the space charge forces between particles using a point to point space charge calculation rather than a PIC calculation. This allows the particles to be modeled in a fully three-dimensional space, however, limitations on the rf field modeling for the rf gun require the use of azimuthally symmetric accelerating fields. Because point to point space charge calculations are performed, this code is limited to modeling a small number of particles before the time requirements to run the simulation are prohibitive. Up to 4,000 particles are used in simulating the electron bunch. In PARMELA, the particles all have the same charge and mass and the particle distribution determines the beam profile. The simulation begins at the photocathode in the electron gun where the electrons are produced according to the laser profile. The description of the rf gun dynamics is presented in Chapter 3. PARMELA is employed to model the electron beam up to the injection point into the plasma lens. In using PARMELA, the correlated beam characteristics produced in the rf gun are maintained in the simulation. PARMELA accurately models the rf gun dynamics as is demonstrated in Chapter 3 and Chapter 4. At the injection point to the plasma lens, particle positions and momentums in space are exported to MAGIC where they are translated into the cylindrically symmetric coordinate system used in the PIC code. The beam particles are then allowed to propagate through the plasma whose density profile in MAGIC is matched to the measured plasma density profile. The results of these simulations are presented in Chapter 4 as part of the overdense plasma lens experiment

analysis.

2.5 Summary

A simple physical model for the "passive" overdense plasma lens has been described. This model is verified with both analytic calculations and with 2-D computer simulations. From the simple model, it is understood that the plasma requires a minimum time of $1 / \omega_p$ in order to respond to the electron beam. Furthermore, The focusing properties of the overdense plasma lens depend critically on the electron beam. From the analytic model and the computer simulations, it has been shown that the plasma response to a sharp rise time of the electron beam can excite plasma oscillations which will effect the overdense lens focusing properties. In demonstrating an overdense plasma lens, the dynamic focusing from the plasma response must be resolved. Additionally, in order to demonstrate practical focusing, a thin lens should be used which will significantly reduce the electron beam spot size (> factor of 2 reduction). The experimental results can then be compared directly with numerical calculations using the analytic model and computer simulations. In order to realize an experiment in which a practical lens is used to demonstrate dynamic focusing, the electron beam parameters must be carefully considered. In Chapter 3, the electron beam used for the demonstration of dynamic focusing of a relativistic electron beam is described in detail and the optimum choice for plasma density and electron beam characteristics is discussed.

Chapter 3

Development of an Electron Beam for Laboratory Demonstration of Plasma Lenses

3.1 Introduction

A laser driven rf photo-injector was constructed at UCLA for the study of beam-plasma interactions[28] and beam-photon interactions [38]. This photo-injector is designed to provide a single 4.5 MeV electron bunch of adjustable charge at a repetition rate up to 5 Hz [39]. A short UV (266 nm) laser pulse produces electrons from a copper photo-cathode in the endwall of the 1/2 cell of a 1 1/2 cell rf gun. The laser energy controls the beam charge and can yield up to 7 nC. For low charges the electron bunch duration is determined by the drive laser which operates with either 2 ps or 50 ps FWHM pulses. The versatility of this electron source allows matching of the electron beam parameters with the experimental requirements.

There are three beam parameters which can be adjusted: duration, charge density, and energy. Both the physics of the beam-plasma interaction and the limitations of beam diagnostics determine the electron beam requirements for plasma lens experiments. The beam duration is bracketed between the streak camera resolution and the onset of plasma instabilities other than the electrostatic plasma oscillations which produce the electron beam focusing. The streak camera available for this experiment, a Hadland Imacon 500, had only 3 ps resolution, therefore, to resolve the time dependent focusing, an electron beam duration > 30 ps was required. On the other hand, the bunch duration is limited by the dynamic response of the plasma and the onset of other instabilities, both of which depend on the plasma density. Recall from Chapter 2 that the minimum response time of the plasma in both the overdense and underdense regime is $\approx 1/\omega_p$ due to the inertia of the plasma electrons. In order to resolve the onset of the plasma response, $1/\omega_p$ must exceed 5 ps. This constrains the plasma density, n_p , to less than $1 \times 10^{13} \text{ cm}^{-3}$. The plasma density ($n_p \approx 4 \times 10^{12} \text{ cm}^{-3}$) was chosen so that $1/\omega_p \approx 9$ ps. The plasma instabilities which limit the electron beam length are the hose instability [40] and the two stream instability [41]. The growth rates for these instabilities are typically longer than $10 1/\omega_p$ which for the above chosen plasma density is ≈ 100 ps. However, it will be shown that for the overdense plasma lens experiment, the bunch duration was actually limited by the properties of the photo-injector to 80 ps (25 ps FWHM) and therefore these instabilities were never an issue.

Given the beam duration, the electron bunch charge density is determined by the transverse spot size and the charge per bunch. The required bunch density depends on the plasma regime in which the lens will operate: overdense or underdense. As was defined in Chapter 2, in the overdense regime the plasma density is larger than the

electron beam density, where as, in the underdense regime the reverse is true. Since the plasma density, as defined by the optimal plasma response time, is approximately $4 \times 10^{12} \text{ cm}^{-3}$, the beam density must be less than $4 \times 10^{12} \text{ cm}^{-3}$ for the overdense lens and greater than $4 \times 10^{12} \text{ cm}^{-3}$ for the underdense lens. The minimum acceptable spot size depends on the minimum spatial profile which can be resolved by the streak camera diagnostic. The static spatial resolution achieved with our streak camera was $\approx 33 \text{ }\mu\text{m}$. In order to dynamically resolve a significant spot size reduction, (> 5) the initial spot size was chosen to be $> 1 \text{ mm}$ FWHM, which corresponds to a $\sigma_r \approx 0.04 \text{ cm}$ assuming a gaussian profile. Finally, later in this chapter, it will be shown that the bunch length is limited to $\approx 25 \text{ ps}$ FWHM, which corresponds to a $\sigma_z \approx 0.3 \text{ cm}$. Therefore, the charge which matches the beam density with the plasma density is

$$Q = (2\pi)^{\frac{3}{2}} en_p \sigma_r^2 \sigma_z = 4.8 \text{ nC}. \quad (23)$$

To access the overdense plasma lens regime, the beam charge must be less than 4.8 nC or the spot size must be larger than 1 mm FWHM, while for a plasma lens in the underdense regime the beam charge must exceed 4.8 nC.

Finally, the least critical beam parameter to match is the beam energy. The only requirement on beam energy is that the electron beam be relativistic so that the self-magnetic field becomes comparable to the space charge force. It is the self-magnetic field force that focuses the beam. Electrons with energies above 3 MeV have velocities within 5% of the speed of light. However, as the energy increases the focal length of the lens also increases proportionally, as shown in Chapter 2, due to the increased electron mass. Since the focused spot size is proportional to the focal length, lower energy beams will experience a greater reduction in spot size. Beam energy between 3 and 15 MeV will

result in a measurable spot size reduction.

The UCLA rf gun photo-injector is a versatile electron beam source which can produce electron beams with 2 ps or 25 ps FWHM bunch lengths and up to 7 nC of charge per bunch at energies up to 4.5 MeV. This parameter range satisfies the requirements dictated by the diagnostics and plasma source available for performing the overdense plasma lens experiment. In Section 3.2 the characteristics of the rf photo-injector and the system components required for its operation are described, while in Section 3.3 measurements of the electron beam produced by the UCLA photo-injector are presented.

3.2 RF Photo-injector

3.2.1 Introduction

The first rf photo-cathode electron gun was proposed in 1985 by Fraser *et al.* [42] and tested in 1988 by Sheffield *et al.* [43]. The basic innovation was the installation of a photo-cathode in an rf accelerating structure. Resonant rf cavities are used for acceleration of particle beams to high energies since they act as step-up transformers by magnetically coupling the rf power into the TM_{010} mode of an rf cavity which sustains large electric fields on axis for particle acceleration [44]. Because these accelerators operate at high frequencies (MHz-GHz), they can sustain larger electric field gradients than DC accelerators [45] and are therefore more compact than DC guns [46]. By placing a photo-cathode in these high electric fields (up to 100 MV/m), the electron beam is quickly accelerated to relativistic velocities, thereby reducing the effects of space charge on emittance growth [47]. Furthermore, laser control over the electron emission offers

the opportunity of producing intrinsically brighter electron beams than those produced by thermionic guns. Therefore, rf photo-cathode electron guns are compact, high quality electron beam sources.

Photo-injectors utilize picosecond laser pulses synchronized with high power rf to create a short electron beam in an rf gun. Typically, an rf accelerating structure is configured in the π -mode, so that each cell supports anti-parallel electric fields to each adjacent cell. In a full cell the accelerating electric field is maximum at the center of the cell, where as, in a 1/2 cell the field is maximum at the endwall of the 1/2 cell, opposite the iris. By positioning the cathode in the endwall of the 1/2 cell the electric fields are maximized on the cathode providing for maximum acceleration. Because the rf fields oscillate in time, in an rf accelerator, the time of flight for the electrons to traverse a cell is matched to the half-period of the rf so that the electrons constantly experience an accelerating field. These accelerators are used once the electron beam has reached relativistic velocities ($v \approx c$) in order to facilitate matching the electron velocity to a periodic accelerating structure. However, in photo-cathode rf guns, since the electrons are born at rest within the accelerator, and since the time of flight between cells is matched for electrons which travel near the speed of light, the laser must produce the electrons at the appropriate rf phase which allows the electrons time to reach the iris between cells before the polarity of the rf fields changes. The optimum injection phase occurs slightly before the cavity reaches its maximum accelerating gradient and depends on the peak accelerating gradient achieved in the cavity [37]. By synchronizing the laser with the rf, the electrons can be produced at exactly this optimum phase. The combination of large electric fields on the cathode with the ability of precisely controlling the injection of the electrons produces an electron beam of superior quality.

Until the advent of the photo-cathode gun, electrons were produced thermionically in either DC or RF guns. A thermionic cathode produces electrons continuously. The electron bunch length produced directly by DC guns is determined by the switching time of the pulsed DC field, where as, in rf guns the bunch length is determined by the fraction of the rf field period which provides sufficient acceleration on the cathode to match the electron velocity with the accelerating structure ($\approx \lambda/4$). In order to produce short electron bunches with high peak currents, rf bunching sections are employed to compress the beams from DC and RF thermionic guns. These additional rf cavities add expense and complexity to the accelerator and furthermore are limited in the ultimate beam brightness which they can achieve [42].

The use of photo-cathodes results in many advantages over the use of thermionic cathodes. With photo-cathodes, the laser spatial profile and duration, in principle, determine the electron emission. Since picosecond lasers can be used to drive photo-cathode rf guns, the need for bunching sections is eliminated. Furthermore, by utilizing the precise control over the electron emission offered by laser-driven photo-cathodes, electron beams which are brighter than those from thermionic guns can be produced.

Photo-injectors produce brighter beams since photo-cathodes produce higher peak currents than the thermionic emitters and since these guns also produce inherently lower emittance beams. Thermionic cathodes produce up to 10 A/cm^2 [42] of current, while photocathodes can produce many kAmps/cm^2 of current provided there is enough laser energy [48]. The improved inherent emittance is easily seen by applying the emittance definition to laser produced electrons. The minimum intrinsic emittance of a beam generated from a thermionic cathode is:

$$\varepsilon = 2\pi r_b \sqrt{\frac{kT}{m_e c^2}} \quad (24)$$

where r_b is the beam radius at the cathode, k is Boltzman's constant, T is the cathode temperature, m_e is the electron mass, and c is the speed of light in vacuum [1]. For a photo-electron we replace kT with $h\nu - \phi_0$ where h is Plank's constant, ν is the laser wavelength and ϕ_0 is the work function of the cathode. For a standard thermionic cathode operating at a temperature of 1160 K the beam emittance for a 1 mm radius cathode is $8.8 \times 10^{-7} \pi$ -mm-mrad. For a carefully chosen photo-cathode and laser wavelength such as copper ($\phi_0 = 4.65$ eV) and the 4th harmonic of YAG at 266 nm ($h\nu = 4.66$ eV) the predicted emittance is only $2.8 \times 10^{-7} \pi$ -mm-mrad, an improvement of a factor of three. However, when the cathodes are placed in the large electric fields in rf guns the work function is reduced [49]. In the example of copper, for fields of 100 MV/m the work function is reduced by 0.38 eV thereby increasing the energy spread of the produced electrons and resulting in an emittance of $1.7 \times 10^{-6} \pi$ -mm-mrad which is actually larger than that of the thermionic cathode. Therefore, the choice of cathode material and laser wavelength is critical for the improvement of beam emittance over that of thermionic emitters.

Currently, neither thermionic nor photocathode guns have achieved this minimum intrinsic beam emittance due to additional emittance contributions from the nonlinear rf fields and space charge. However, the normalized emittances produced by photo-injectors are lower than those produced by thermionic guns. The improvement comes from the quick acceleration that occurs in a photocathode rf gun because the electrons are produced in extremely large electric fields (≈ 100 MV/m) and the small emission area

which is controlled by the laser spot size on the photo-cathode. Since the beam is quickly accelerated to relativistic velocities, the effective emittance growth due to space charge is reduced, while the small emission area reduces emittance growth due to the rf fields since less of the nonlinear fields are sampled by the electron beam. However, a small electron emission area will result in increased space charge forces which can produce a degradation in the beam emittance if the desired beam charge is large. Therefore, an optimum laser spot size on the cathode exists for minimizing emittance growth for a given beam charge. As accelerating structures are improved to reduce nonlinear rf fields and increase field gradients, the beam brightness from photo-injectors will approach the fundamental limits mentioned above. Nevertheless, laser driven rf guns provide improved performance over thermionic guns due to the larger current densities which can be produced and the reduced emittance growth from space charge and nonlinear rf fields.

Additional advantages of photo-injectors due to the control of electron emission by the laser pulse have been postulated since the inception of photocathode rf guns [50]. Since the laser profile and more recently the temporal profile of laser pulses can be carefully controlled, shaping of the electron beam is possible. However, the added complexity of tailoring the laser pulses may decrease photo-injector reliability and the practicality of electron beam shaping has yet to be demonstrated. Fundamental studies of photo-injector performance need to be completed before assessing the viability of electron beam bunch shaping and whether the improvements merit the added difficulties of laser pulse shaping.

The UCLA photo-injector is based on the Brookhaven National Laboratory (BNL) gun design [37]. It consists of a 1-1/2 cell accelerating section which is inductively coupled to a TE_{010} waveguide so as to maximize coupling to the π -mode and suppress the 0-mode as shown in Fig. 3.1. The cathode is removable so that various materials could be

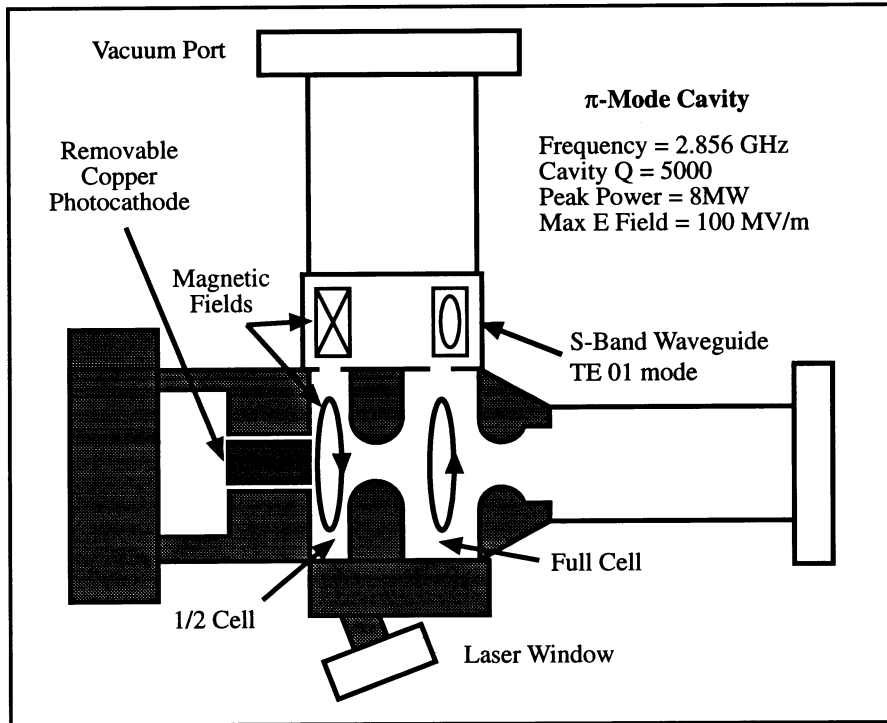


Figure 3.1: UCLA RF Gun

tested and so that the cathode could be replaced if damaged. For standard gun operation Cu was chosen as the cathode material. This choice was based on the exclusive use of copper in the rf gun construction and its ability to withstand the large fields supported in the rf gun. Secondly, the work function for copper is 4.65 eV. This is less than the energy of 266 nm light (4.66 eV), a common laser wavelength. Finally, although the quantum efficiency of copper is poor for a photo-cathode (1×10^{-5}), copper does not require the ultrahigh vacuum needed to maintain better cathodes such as cesium antimonide [51]. Cesium cathodes offer quantum efficiencies as high as a few percent, however, even under vacuum better than 10^{-10} Torr, typical lifetimes are only a few days in the rf gun environment [51]. On the other hand, the lifetime of a copper cathode is

indefinite barring laser damage or severe arcing damage from the breakdown of the large electric fields at the cathode surface.

In this section, 3.2, the hardware associated with the rf photo-injector is described. First the tuning of the rf gun for optimal accelerator performance is delineated in detail and the results are compared with numerical calculations. Next, the laser system used to generate the electrons from the photo-cathode is described. Finally, the rf power system and the laser triggering system are outlined and the critical timing links between the laser and the rf system are designated.

3.2.2 RF Gun Tuning

Tuning of the rf gun consists of two major elements: balancing the fields between the 1/2 cell and the full cell and setting the cavity resonance frequency to match the rf power source. If the gun has been designed and constructed correctly, other important rf cavity parameters, such as the coupling and Q, will have satisfactory values once the fields are balanced and the frequency is matched. There are two controls for tuning the gun balance and frequency. These are the gun temperature and the cathode position. Both affect the resonant frequency of the gun by perturbing the cavity geometry. The gun temperature affects both the 1/2 cell and the full cell almost identically and therefore does not significantly change the field balance while changing the resonant frequency. On the other hand, movement of the cathode in the 1/2 cell drastically affects both the field balance and the resonant frequency. Therefore, in tuning the gun, the field balance is adjusted first, by positioning of the cathode, while the resonant frequency can be matched later by adjusting the gun temperature.

Both the resonant frequency matching and the field balance are critical for optimal rf

gun performance. The effects of a frequency mismatch between the rf power source and the rf gun are simple to understand. If the frequency mismatch is less than half of the resonance width, the TM_{010} accelerating mode will still be driven in the cavity, but because of the mismatch, the power coupling will be low and most of the rf power will be reflected by the cavity instead of being absorbed and coupled to the electron beam. This results in poor power efficiency and reduced beam quality if the required large electric fields (≈ 100 MV/m) are not achieved on the cathode. However, if the mismatch is larger than the resonance width, power could be coupled into adjacent cavity modes which would not provide any acceleration for the electron beam. Fortunately, a frequency mismatch is easily remedied by adjusting the gun temperature for minimum reflected power from the cavity.

On the other hand, a field imbalance between the 1/2 cell and the full cell will severely limit rf gun performance even when the resonant frequency is matched to the rf power source. The main effect of a field imbalance is to limit the electron beam energy. The ultimate limit on electron energy is due to the maximum accelerating gradient achieved before surface breakdown occurs in the cavity. Therefore, with imbalanced fields this breakdown will occur sooner in one cell than in the other, whereas by balancing the fields, the highest field gradients can be achieved in both cells simultaneously. With a lower beam energy the space charge force acts more strongly and the beam will suffer greater beam emittance degradation and bunch lengthening than with a higher energy beam. This is particularly significant in the 1/2 cell where the beam is accelerated from rest. Aside from beam energy limitations, a field imbalance can directly degrade beam quality by introducing higher order spatial harmonics. As was mentioned in the introduction, one of the major causes of emittance growth in the photo-injector is the

nonlinear rf field. The addition of higher order spatial harmonics adds nonlinear rf fields which produce added emittance growth. Finally, a field imbalance, such that the field in the full cell exceeds that of the 1/2 cell, will affect the emission of electrons from the cathode. When generating a high current electron beam, the axial space charge field of the beam can become comparable with the accelerating electric field. In this case, the emission from the cathode will be space charge limited. Unfortunately, the field balance is controlled by the cathode position. Since an adjustment to the cathode position also changes the resonant frequency of the cavity, the gun temperature must be adjusted simultaneously to keep the cavity frequency matched to the high power rf source. This is a difficult and tedious adjustment at high power. Therefore, it is important to balance the 1/2 cell and full cell fields to within 10 % before installation of the rf gun into the high power rf system.

In the BNL gun design, the coupling through the iris between the full cell and the 1/2 cell is small therefore the field balance depends critically on the resonant frequencies of each cell independently. Since the cathode is placed in the endwall of the 1/2 cell where the electric fields are maximized, the position of the cathode significantly affects the capacitance of the 1/2 cell and therefore its resonant frequency. When the 1/2 cell frequency is not matched closely to the full cell frequency, the cells become decoupled and the cavity no longer resonates in the π -mode. The ratio of the field in the 1/2 cell to that in the full cell is related to the coupling between the cells. As was mentioned previously, the cathode in the UCLA gun is removable. A numerical field solver, SUPERFISH [52], was used to study the field profile as a function of cathode position. The results of these calculations are shown in Fig. 3.2 and indicate that a cathode displacement of 50 μm will produce a field imbalance of almost a factor of 2. Since the

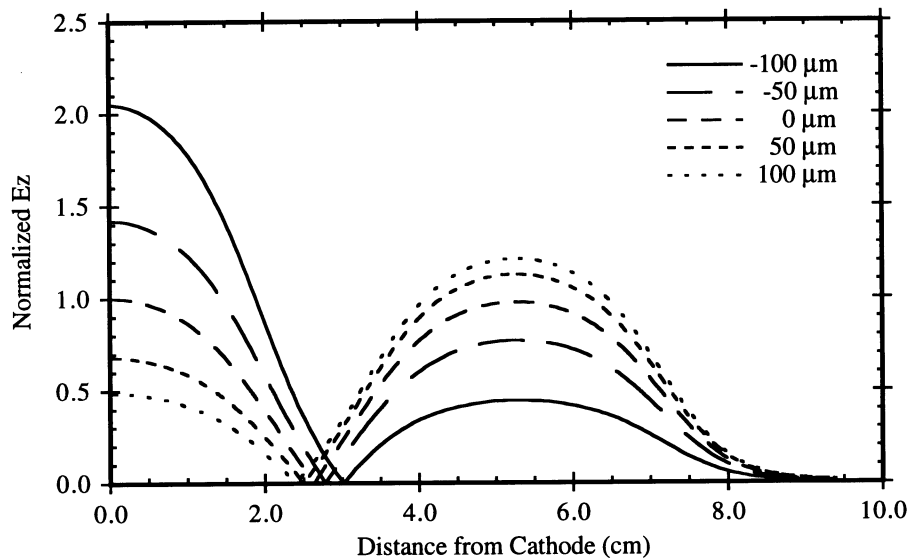


Figure 3.2: Calculated RF Gun Field Profiles on Axis for Various Cathode Positions

cathode in the UCLA gun is movable, careful measurements of the field balance are required in order to position the cathode precisely where the 1/2 cell and full cell fields balance.

Measurement of the field balance is performed using the frequency perturbation method as described by Ginzton [53]. According to Slater perturbation theory, a metallic bead, introduced into the cavity, produces a perturbation on the resonant frequency which is proportional to the square of the electric field [54]. By scanning the bead along the axis of the rf gun and recording the frequency shift of the π -mode resonance, the axial electric field profile is mapped. The resonant frequency and the frequency shift produced by the metallic bead were measured with a HP 8720A network analyzer. When given time to average, the resolution of the network analyzer is better than 100 Hz. However, it was empirically determined that the accuracy of the measurement was ± 1 kHz due to temperature drifts which occurred on a time scale of about 15 min. It is shown in Fig.

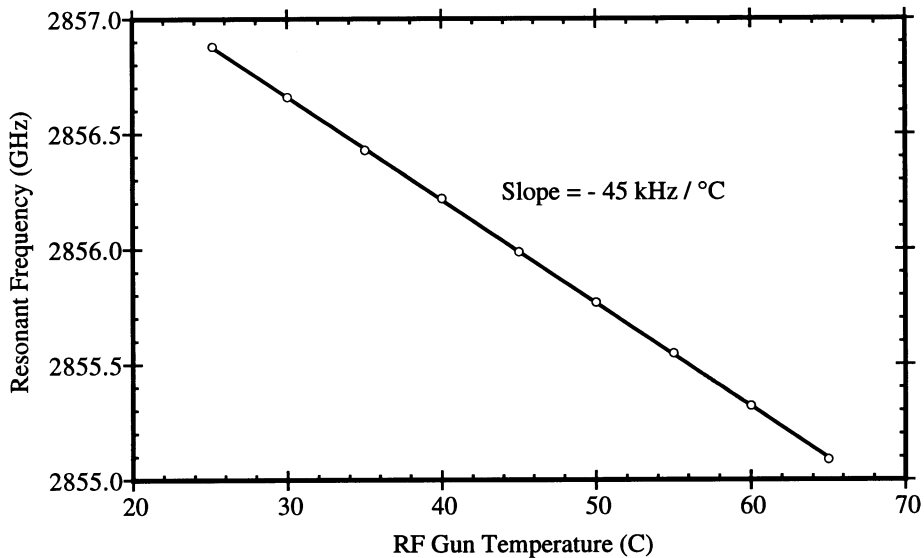


Figure 3.3: Measured Resonant Frequency Dependence on Gun Temperature

3.3 that the resonant frequency varies linearly with the gun temperature with a slope of 45 kHz/ °C. Given that the temperature stability of the water chiller used to control the rf gun temperature is specified as ± 0.05 °C, the measured error of ± 1 kHz is better than the expected error of ± 2 kHz due to thermal fluctuations. The improvement of the thermal stability is probably due to the heat capacity of the rf gun. The maximum frequency shifts induced by a metallic bead, without distorting the field profile of the cavity, are about 200 kHz. With a measurement error of only ± 1 kHz, the field balance can be measured to better than 0.5%

In order to achieve a 0.5% accuracy in the field balance measurement, the systematic error introduced by the fiber which supports the bead and by the metallic bead itself must be considered. Since the cathode is in the endwall of the 1/2 cell, the metallic bead is introduced through the full cell. The rf gun is turned on its side, so that the 1/2 cell lies beneath the full cell, and the metallic bead is suspended into the gun from the tip of a 125

μm diameter optical fiber. This fiber is attached to a micrometer that allows for precise movement of the bead and a calibration of the bead's distance from the cathode. Although the fiber is a dielectric and therefore perturbs the frequency much less than the metallic bead, its perturbation of the frequency is significant. Therefore, this perturbation must be subtracted from the bead data for an accurate field measurement. The frequency perturbation caused by the optical fiber alone is plotted in Fig. 3.4. Once this systematic

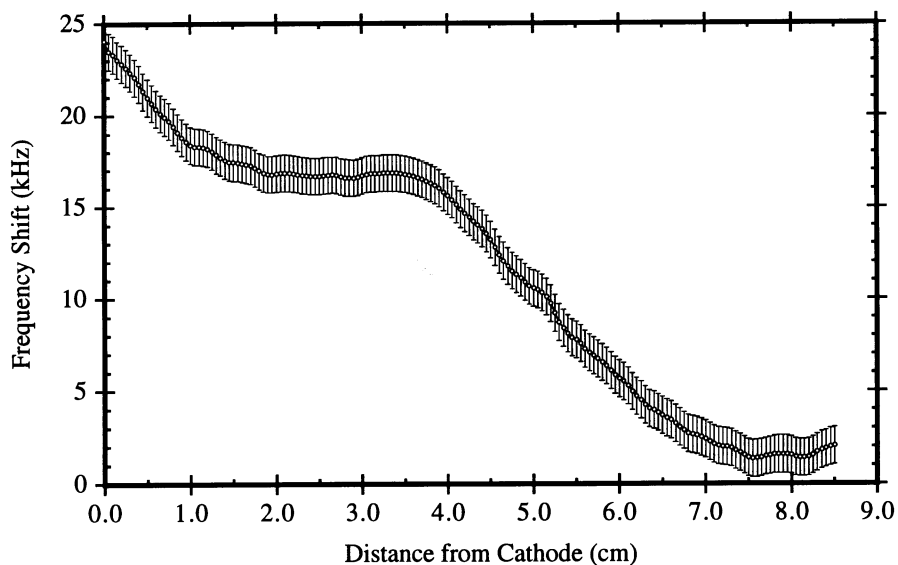


Figure 3.4: Measured Perturbation Induced by Optical Fiber

error has been corrected, the square root of the frequency shift is plotted as a function of bead position. Another source of error can be introduced by the metallic bead itself. If the bead is too large, the bead will modify the electric fields in the cavity so that the frequency perturbation no longer represents the fields in the gun but instead the fields of the cavity-bead system. Plots of the inferred field profile for various bead sizes are depicted in Fig. 3.5. Beads larger than 2 mm introduced significant perturbations on the field profile, while the 1 mm bead measurement resulted in lower signal to noise than the

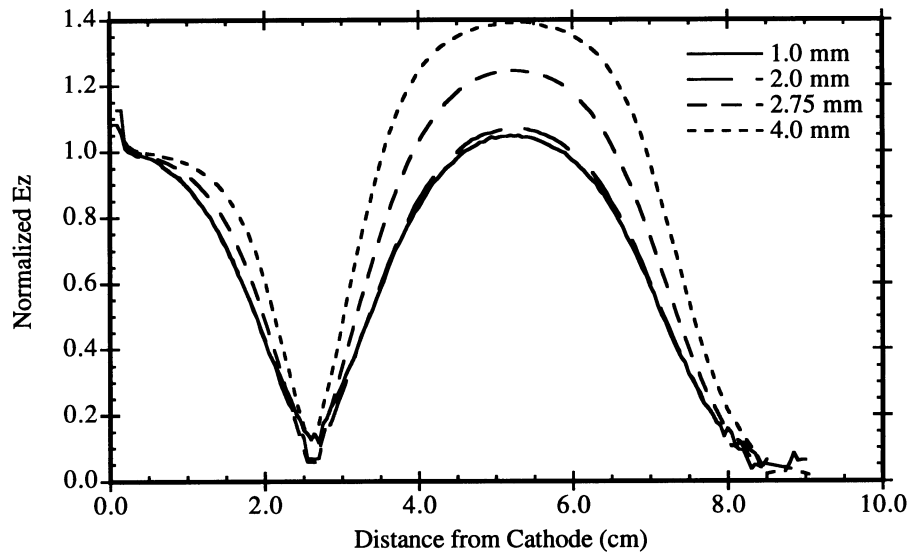


Figure 3.5: Inferred Field Profile on Axis for Various Bead Sizes

2 mm bead due to the fixed error of ± 1 kHz and the smaller frequency shifts. Therefore, the optimum bead diameter is 2 mm. As shown in Fig. 3.6, the field measurements agree

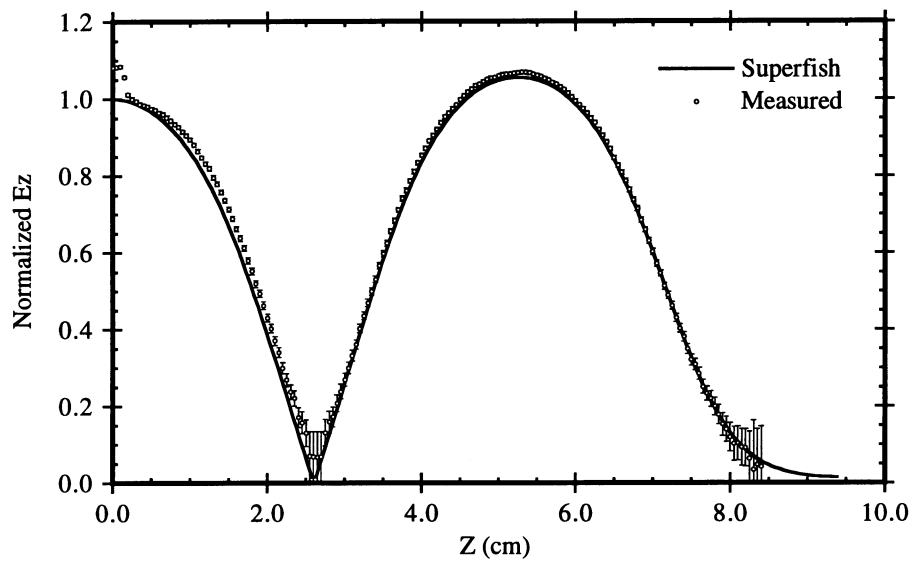


Figure 3.6: Comparison of Calculated and Measured on Axis Field Profile

extremely well with the field profiles predicted by SUPERFISH.

Once the fields have been balanced, the gun temperature must be set so that the cavity resonance frequency matches that of the rf power source. The temperature tuning is performed by changing the temperature of the reservoir which feeds the gun's water jacket. It was shown in Fig. 3.3 that a 1 °C increase in temperature produces a 45 kHz decrease in the cavity resonance. The high power rf source that drives the rf gun is a SLAC XK-5 Klystron which operates at 2.856 GHz. In tuning the cavity resonance to match the klystron output, the change in resonance frequency due to the difference in the index of refraction between air and vacuum must be considered. Although the rf gun is operated under vacuum in order to prevent breakdown of the large electric fields and to provide a vacuum environment for electron beam propagation, the tuning of the gun is performed at atmosphere. The change in the resonant frequency caused by changing from air to vacuum can be calculated from the difference in the index of refraction and is approximately 800 kHz. This frequency shift was confirmed by the measurement of a 790 ± 10 kHz shift in the resonance when the gun was pumped down to vacuum. Since the tuning is performed at atmosphere, the gun is temperature tuned to resonate at $2.85520 \text{ GHz} \pm 10 \text{ MHz}$. The effect of temperature tuning on field balance was measured and proved to be small, although not insignificant, as shown in Fig. 3.7. A 40° C increase in the gun temperature resulted in a 10% increase of the full cell field over the field at the cathode. The change in field balance due to a change in temperature is caused by unequal thermal expansion of the stainless steel flange which holds the cathode and the copper gun itself. Since the stainless steel expands less, the net effect is to move the cathode into the cavity which, as shown in Fig. 3.2, shifts the field balance in favor of the full cell. Therefore, the final field balance should be performed within 4 °C of the

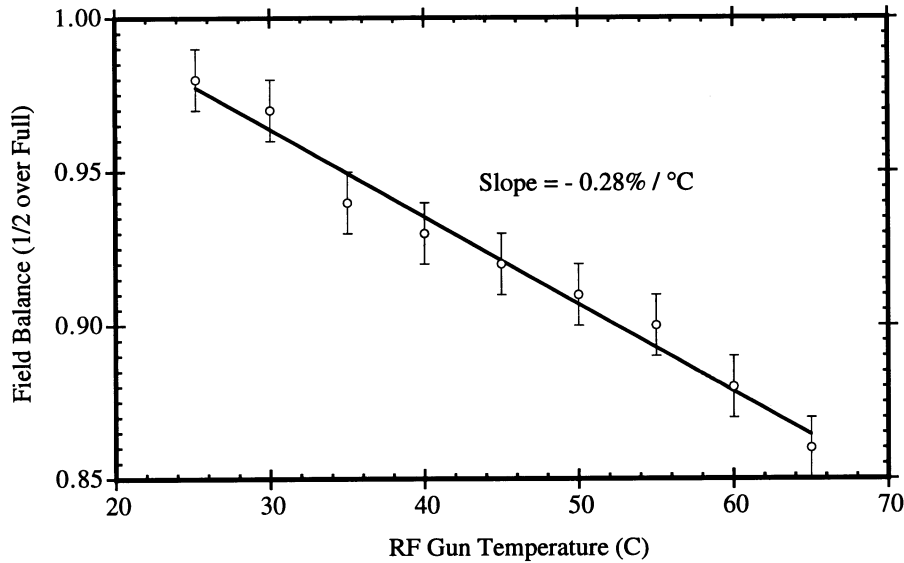


Figure 3.7: Measurement of Field Balance Dependence on Gun Temperature

resonance so that the temperature tuning effect on the field balance will be less than 1%. The UCLA rf gun was tuned at atmosphere to $2.85520 \text{ GHz} \pm 10 \text{ MHz}$ at a temperature of $65.0 \text{ }^\circ\text{C}$ with a field ratio of 1.00:1.00 1/2 cell to full cell.

With the rf cavity tuned, careful measurements of the cavity parameters can be undertaken. These include measurements of the waveguide coupling coefficient (β_w) and Q as well as calibrations of power monitoring antennas in each cell. The gun coupling is set by the dimensions of the coupling irises between the waveguide and the cavity and therefore was fixed at the time of gun construction. The machining of the irises produces a perturbation on the cavity modes. In order to minimize this perturbation the irises were enlarged during construction until near critical coupling was achieved but the gun still remained slightly undercoupled. The coupling is determined from a measurement of the VSWR at the resonant frequency. Since the cavity is undercoupled, $\beta = 1/\text{VSWR}$ [53]. The measured VSWR equalled 1.13 therefore $\beta_w = 0.89$. Because

the coupling is primarily determined by the geometry and size of the coupling irises, β_w showed only a weak dependence on cathode position and proved to be independent of gun temperature. The loaded Q , Q_L , was determined from the half-power bandwidth of the transmission from the waveguide port to the full cell monitor antenna. The bandwidth was measured to be 536 KHz, centered about the resonant frequency of 2.85620 Ghz, which results in a loaded Q :

$$Q_L = f/\Delta f = 5300 \quad (25)$$

where Δf is the half power bandwidth and f is the resonant frequency. The unloaded Q , Q_0 , can then be calculated using the coupling coefficients of the waveguide and the monitor:

$$Q_0 = Q_L (1 + \beta_w + \beta_a) \quad (26)$$

where β_a is the coupling coefficient of the full cell monitor. Since the fields in the cavity approach 100 MV/m, both the 1/2 cell and full cell monitor antennas have been constructed to provide a maximum of -35 dB power transmission between the cavity and the antenna port. Therefore, the coupling coefficient for the full cell monitor is essentially equal to zero and can be ignored in the determination of Q_0 . Using the measured value of β_w , the unloaded Q is calculated: $Q_0 = 10,000$. The purpose of the 1/2 cell and full cell antennas was to monitor any changes in the field balance and to observe rf breakdown in the cavity during high power operation. Unfortunately, at high power, it is difficult to measure power to better than ± 1 dB which corresponds to a field imbalance of $\pm 10\%$. Therefore the monitor antennas can be used for rough tuning of the field balance but when precise field balance is required, low power tuning, as described at the beginning of this section, should be used. The antennas were assembled so that the power coupling

of the monitors would nearly match when the fields were balanced. The measured power coupling at the resonance frequency was -37.6 dB for the 1/2 cell antenna and -37.0 dB for the full cell antenna when the fields were balanced.

Additional measurements were made to test the sensitivity of the cathode position and to compare these measurements with SUPERFISH calculations. The field balance was measured as a function of cathode position and is in excellent agreement with SUPERFISH calculations as shown in Fig. 3.8. The gun balance is very sensitive to

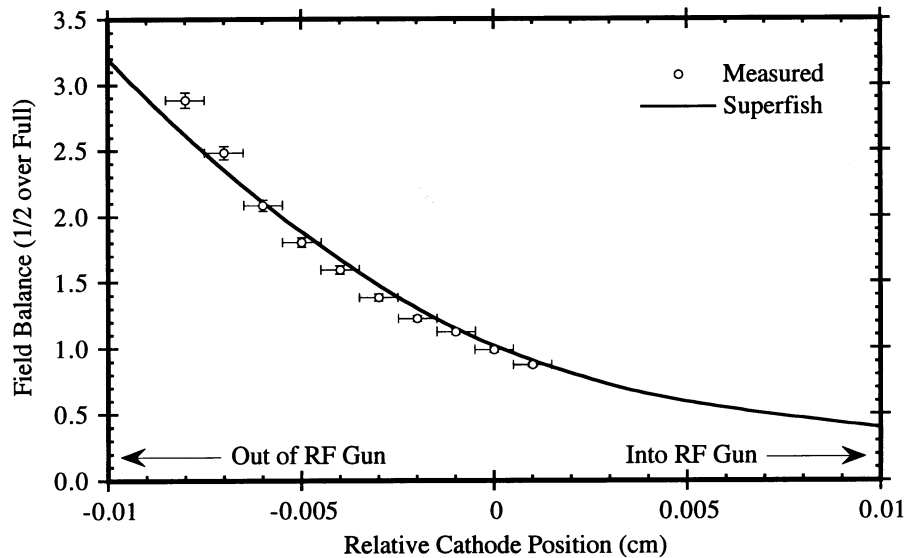


Figure 3.8: Measurement and Calculation of Field Balance Dependence on Cathode Position

cathode position and a 50 μm shift in cathode position can cause a 10% change in the field balance. However, because of slippage in the micrometer mechanism, the micrometer calibrations cannot be used to set the cathode position rather the bead pull should be used to set the field balance. As the cathode position was changed, the resonant frequency also changed along with the field balance. The resonant frequency was measured as a function of field balance and shown in Fig. 3.9 along with the

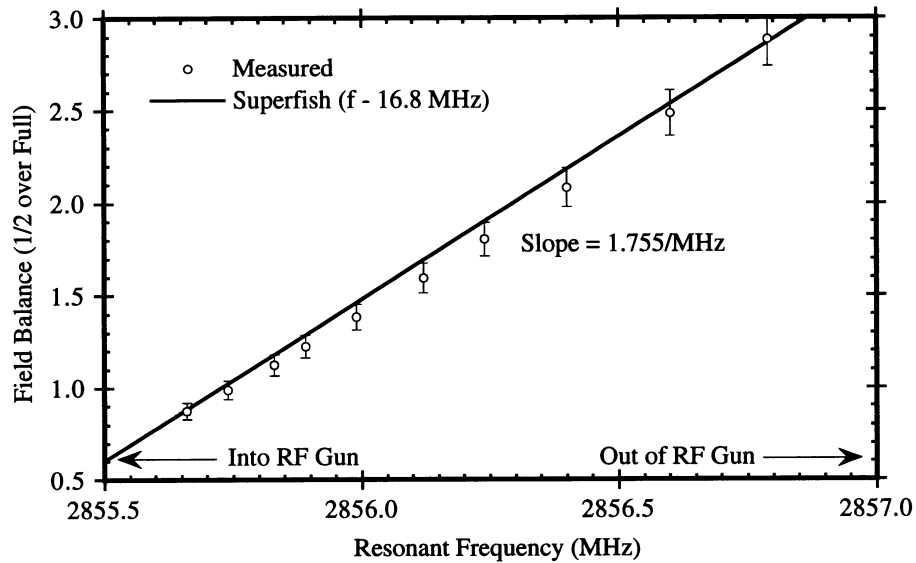


Figure 3.9: Measurement and Calculation of Field Balance Dependence on Resonant Frequency

SUPERFISH calculations. Although the absolute frequency predicted by SUPERFISH was 16.8 MHz higher than the measured frequency, the slope from the SUPERFISH calculations agrees well with the measured data. This frequency offset is due to the perturbations caused by the coupling irises and the monitor ports. Finally, the cavity Q was measured as a function of the field balance. Both the SUPERFISH Q and the measured Q are plotted in Fig. 3.10. SUPERFISH predicted Q values which were higher than those measured by 2600 but the dependence on field balance agreed well with the measurements. The measured values are expected to be lower since SUPERFISH does not include the losses due to the coupling irises.

Because of the sensitivity of the field balance on cathode position, the rf gun fields can become unbalanced easily during operation and an accurate method of balancing the fields without removing the rf gun and performing a bead pull should be developed. The cathode can move 50 μm due to thermal motions produced while the gun is baking out

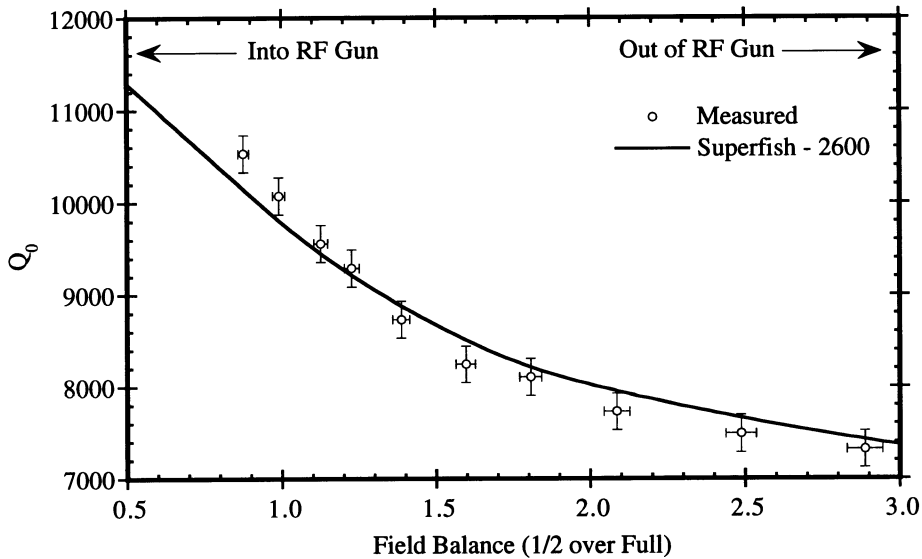


Figure 3.10: Measurement and Calculation of Q Dependence on Field Balance

for high vacuum or from an accidental bump. As has been shown above, a $50\ \mu\text{m}$ displacement of the cathode will produce more than a 10% change in the field balance and also a change in the resonant frequency. Pulsed power measurements have accuracies of no better than 10% where as cw rf measurements with calibrated network analyzers can be accurate to better than 1%. Because the bead pull is not easily implemented with the rf gun in place and additionally would require bringing the gun up to atmosphere, another method of balancing the fields was investigated using SUPERFISH. The difference between the π -mode resonance frequency and the 0-mode resonance frequency depends on the field balance as shown in Fig. 3.11. When the fields are balanced, the difference between the π -mode and the 0-mode equals $1.73\ \text{MHz} \pm 30\ \text{kHz}$. Unfortunately, this frequency difference is not unique to the field balanced case but also occurs when the field in the 1/2 cell is twice that in the full cell. However, by starting with the cathode position inside the gun with respect to the field balance point, the difference frequency

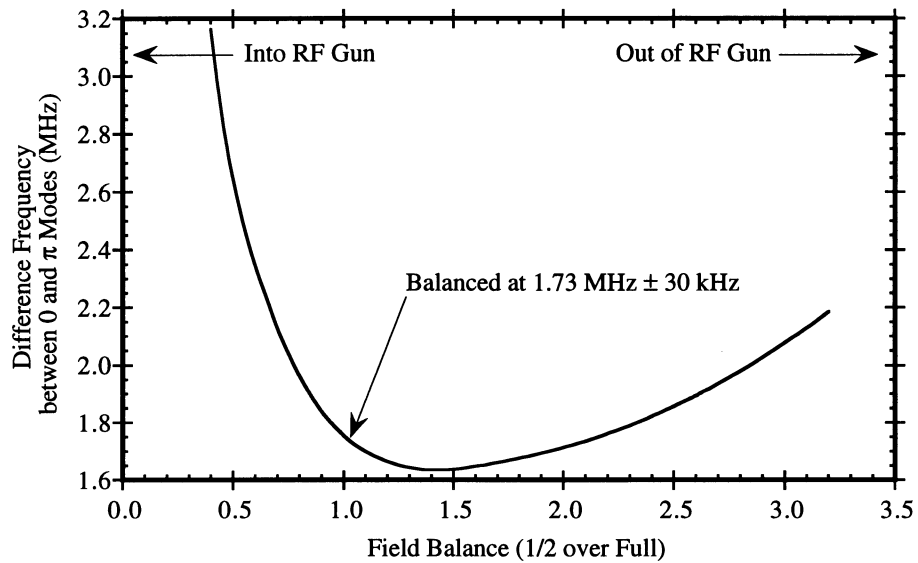


Figure 3.11: Calculation of Difference Frequency Dependence on Field Balance

could be measured as the cathode is slowly pulled out of the gun. At the point where the frequency difference equals $1.73 \text{ MHz} \pm 30 \text{ kHz}$ the gun will be balanced. If the minimum frequency difference is found while adjusting the cathode position, then the field balance point has been passed and the cathode should be pushed back into the gun and the balancing process should be started again. The limitations of this measurement are due to the accuracy with which the frequency difference can be made given the poor coupling available through the monitor loops. Since the gun is to remain in place, connected to the waveguide, the network analyzer cannot be coupled to the waveguide port and instead must couple through either the 1/2 cell or full cell port. Since the coupling of these ports is small, the accuracy in the frequency measurement will suffer and an amplifier will probably be required. Before this method for balancing the fields is attempted a cross calibration with the bead pull should be performed to confirm that the required accuracy is achievable.

3.2.3 Drive Laser

Since the laser pulse determines both the pulse length and the total charge of the electron beam, its performance is paramount for achieving a high brightness beam. Because of the high peak laser powers required to produce 1 nC of charge from a copper photocathode chirped pulse amplification and compression[55] was chosen to obtain laser pulses with less than 2 ps duration and 4 mJ of energy at 1064 nm. This technique utilizes self-phase modulation (SPM) and group velocity dispersion (GVD) to increase the spectrum of the pulse in a time correlated fashion so that it may be compressed to its new transform limit using an anomalously dispersive element. Limits on pulse compression are due to the nonlinearity of the spectral bandwidth increase from SPM and the power threshold for other nonlinear effects such as Stimulated Raman Scattering. A schematic of the drive laser is presented in Fig. 3.12.

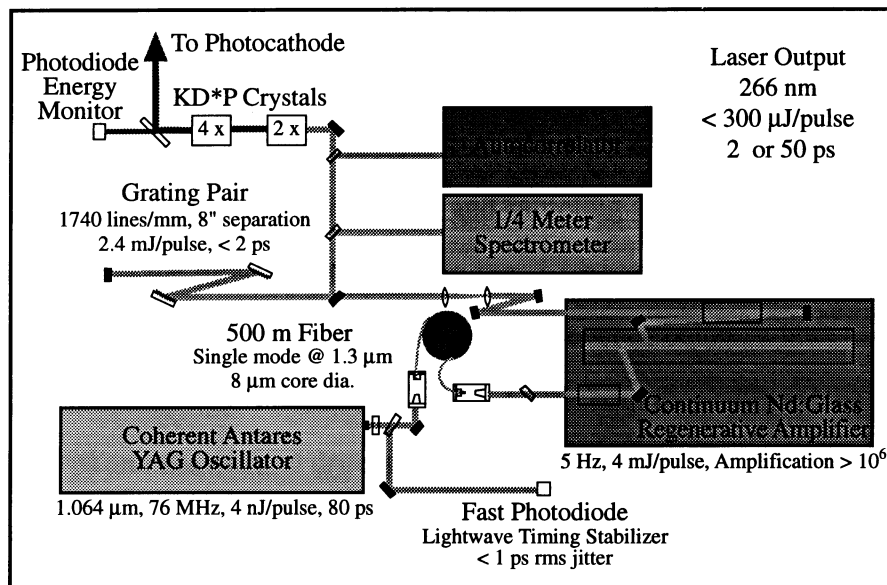


Figure 3.12: Photoinjector Drive Laser Schematic

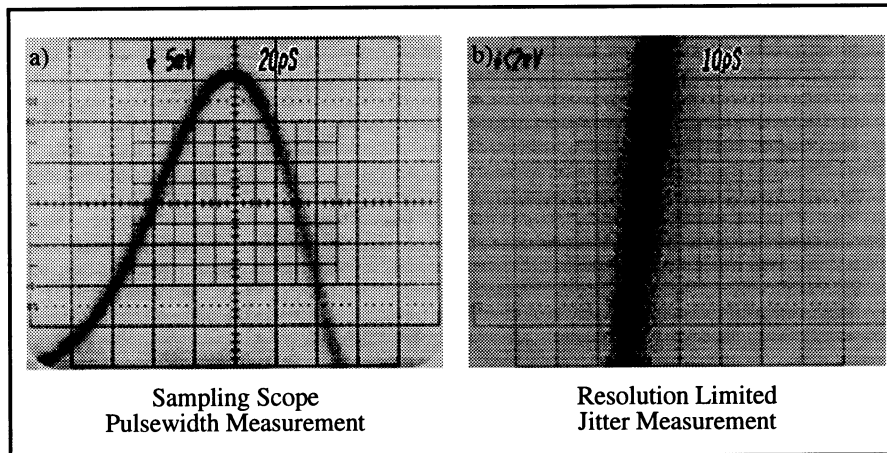


Figure 3.13: Measurements of Mode Locked Oscillator Output

The laser oscillator, a Coherent Antares YAG, produces 80 ps FWHM pulses in a mode locked pulse train at 76 MHz. A sampling scope is used to monitor the performance of the oscillator and to measure the output pulse width. Fig. 3.13(a) shows the scope trace of the Antares output pulse and indicates a pulse width of 80 ps FWHM. The sampling scope can also be used to measure the jitter between the rf and the mode locked pulses. Since the scope is triggered by the rf, the trace shown in Fig. 3.13(b), which shows the rising edge of the photodiode signal, is a measure of the jitter. However, the resolution of the photodiode and sampling scope system is no better than 10 ps and therefore the jitter measurement in Fig. 3.13(b) is resolution limited. In order to reduce the Antares jitter to this resolution limited level or below, a jitter stabilizer was installed which will be described in Section 3.2.4. Without the stabilizer the jitter can be as large as 30 ps and the thermal drifts throughout the day can be greater than 100 ps.

Pulse compression from 80 ps to less than 2 ps is achieved using a fiber-grating compressor (see Fig. 3.14). For optimal pulse compression, 500 m of single mode fiber is used together with a pair of holographic gratings (1700 lines/mm). The grating pair is

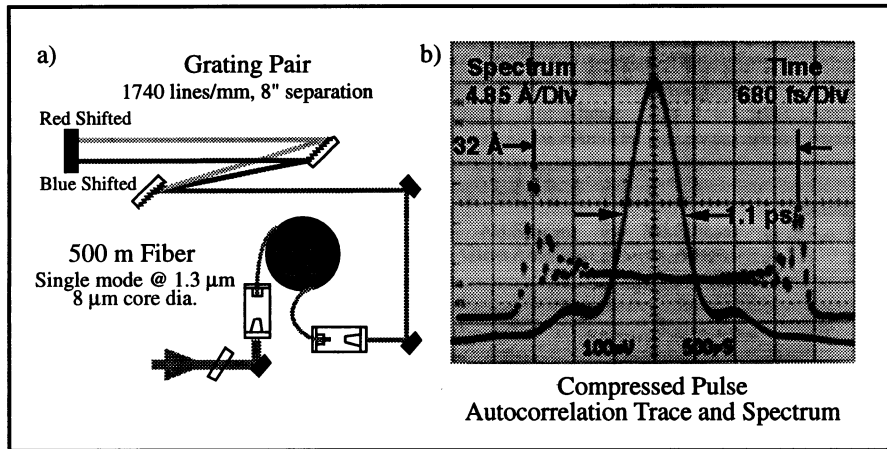


Figure 3.14: Pulse Compression Setup and Output. a) Schematic of the pulse compression system b) Spectrum and autocorrelator trace of the compressed pulse

setup in a double pass configuration at near Littrow incidence (67°) and a grating separation of 9 inches. Optimization of the pulse compression is performed periodically by adjusting the input power to the fiber. Typically, 1 watt of power is coupled through the fiber with an efficiency of 50%. The laser spectrum is continuously monitored and a scanning autocorrelator is used to measure the laser pulse width while tuning the pulse compression with the cw mode locked laser beam. Typical spectrum and autocorrelation traces are shown in Fig. 3.14(b). However, in high power operation, the pulse must be amplified before compression.

A Nd:silicate glass regenerative amplifier from Continuum provides amplification of 10^6 between the fiber and the grating pair. A schematic of the regenerative amplifier layout is depicted in Fig. 3.15. Silicate glass rather than YAG is used so that the full bandwidth of the chirped pulse can be amplified. However, the repetition rate of the regenerative amplifier is limited to 5 Hz due to poor thermal properties of the silicate glass heads. Pockels cell #1 is used to switch one pulse from the cw pulse train into the regenerative amplifier cavity. This pulse is amplified to 3 mJ within 30 round trips in the

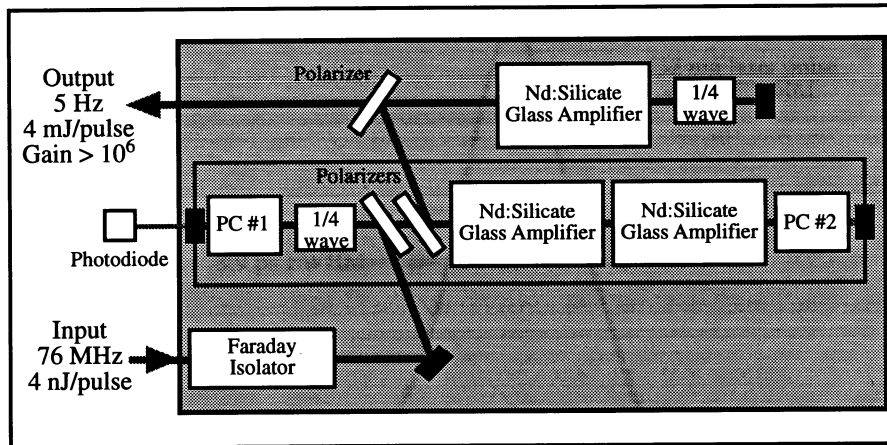


Figure 3.15: Regenerative Amplifier Schematic

regenerative amplifier cavity. Once the pulse has reached saturation it is switched out with Pockels cell #2. The energy gain of this pulse in the regenerative amplifier is monitored by a photodiode which looks at the leakage through one of the cavity mirrors. Scope traces showing the energy buildup in the regenerative amplifier cavity and the

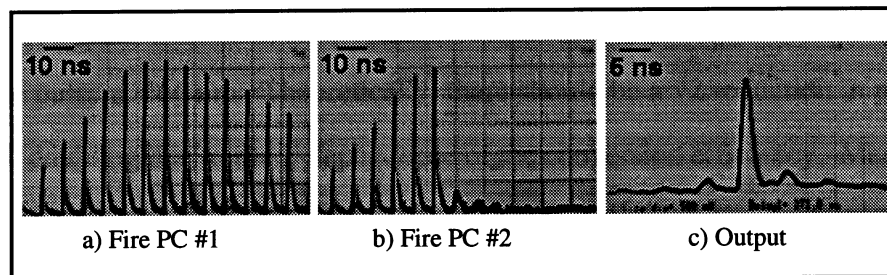


Figure 3.16: Measurement of Regenerative Amplifier Performance. a) Build up and decay of trapped pulse in the regenerative amplifier cavity. b) Switch out of amplified pulse at maximum energy c) Amplified pulse output of regenerative amplifier. (Note that the photodiode response is > 500 ps.)

pulse switch out are shown in Fig. 3.16. The pulse is further amplified to 5 mJ by double passing an external amplifier. Each pulse is still about 100 ps long until compression in the grating pair. The efficiency of the grating pair compressor is about 60%. Therefore, this system provides 3.0 mJ pulses at 1064 nm of less than 2 ps

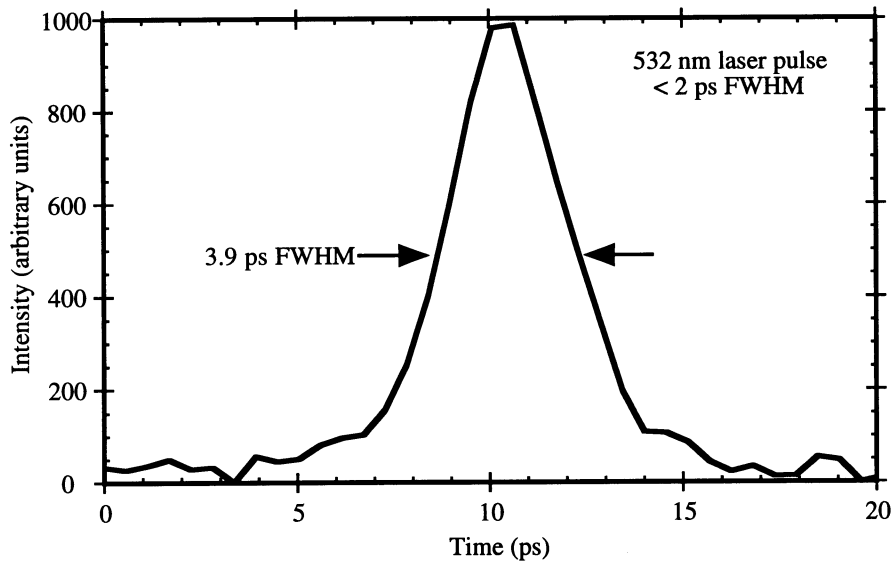


Figure 3.17: Streak of Amplified and Compressed Laser Pulse

duration operating at 5 Hz.

These pulses are then frequency up converted to 266 nm using two KD*P doubling crystals. The net conversion efficiency from IR to UV is about 12% resulting in up to 350 μ J per pulse at 266 nm. Theoretically, there should be a $\sqrt{2}$ reduction in pulse width upon each doubling due to the I^2 dependence of the conversion efficiency. Measurements of the pulse width were obtained after the first doubling crystal using a streak camera. The optical sensitivity of the streak camera did not extend to the IR or UV and therefore pulse width measurements were only conducted at 532 nm. In streaking short pulses, care is taken to avoid space charge saturation within the streak camera which can result in erroneous measurements. Fig. 3.17 depicts a typical laser streak integrated intensity plot. The laser pulse streak resulted in a pulse width of 3.9 ps FWHM. Since the resolution of the streak camera is 3.5 ps, the actual laser pulse width is 1.7 ps. Autocorrelation measurements of the CW mode locked YAG laser beam result in pulse widths of 2 ps

FWHM. After doubling to green light, the pulse width is expected to decrease by $\sqrt{2}$, producing 1.4 ps pulses in reasonable agreement with the streak camera measurements.

Because the repetition rate of the regenerative amplifier is limited to 5 Hz, single shot diagnostics are required. Fluctuations in laser energy from shot to shot demand constant monitoring since this will greatly affect electron production and accelerator performance. Therefore we have installed a photodiode to monitor the laser energy for each shot. This photodiode is sensitive to 266 nm and directly measures the UV energy. The photodiode is calibrated against a pyroelectric detector. This calibration is repeated each day to confirm that a change in the beam alignment does not affect the energy measurement. Fluctuations in the laser energy of about 20% are typical although fluctuations as high as 50% and as low as 5% occur depending on the stability of the mode locked YAG.

Although the short pulse (< 2 ps) drive laser system produces the highest brightness and quality electron beam, for the overdense plasma lens experiment a long electron beam is required so that time dynamics of the focusing can be resolved by the 3.5 ps streak camera. Therefore the laser system used to create long electron pulses did not require chirped pulse amplification and compression and instead the 80 ps FWHM mode locked laser pulses were directly amplified by the regenerative amplifier. The amplified pulses were doubled and quadrupled using the same KD*P doubling crystals as in the short pulsed system but with slightly less efficiency. However, since the grating compressor was not used, the full 5 mJ laser pulse was transported to the doubling crystals and therefore the output energy reached the same 350 μ J at 266 nm as did the short pulse system. Since there is a $\sqrt{2}$ reduction in pulse width per doubling crystal, the 80 ps FWHM pulses result in 40 ps FWHM pulses as verified by autocorrelation and streak camera measurements.

3.2.4 Klystron and Timing System

Ultimately the laser pulse must be injected into the rf gun at the correct phase of the rf. This requires the rf to be phase-locked with the laser. The rf frequency is 2.856 GHz. This is dictated by the SLAC klystrons which we use to amplify the rf to peak powers of 20 MW. Therefore the mode locker frequency was chosen to be 38.08 MHz, the 75th subharmonic of 2.856 GHz. The 38.08 MHz is produced by a crystal oscillator whose stability is specified as ± 1 Hz per day. The output of this oscillator is then split to drive the mode locker for the laser and a 75x upconverter which provides 2.856 GHz rf for the klystron. The CW 2.856 GHz and the mode locked laser pulses out of the YAG oscillator can then be monitored on a sampling scope with about 10 ps resolution as described in Section 3.2.3. Under normal operation the jitter between the rf and the laser pulses is ≈ 20 ps, which corresponds to $\approx 20^\circ$ in rf phase. This jitter would produce intolerable fluctuations in beam energy and energy spread at the output of the accelerator. Therefore a timing stabilizer was installed between the crystal oscillator and the mode locker. The stabilizer monitors the 76 MHz laser output via a fast photodiode. The diode signal is then mixed with the second harmonic of the 38.08 MHz. The mixed signal is analyzed by a differential phase detector and the output of the phase detector then drives a phase shifter installed in line with the mode locker. By constantly adjusting this phase the laser pulses are kept locked to the 38.08 MHz oscillator. This stabilizer is specified to reduce the jitter of the mode-locked laser pulses to less than 1 ps RMS.

The cw 2.856 GHz output of the 75x multiplier is insufficient to drive the klystron directly. A pulsed preamplifier is used to amplify to about 200 W over 8 μ s with a repetition rate of 5 Hz synchronized with the firing of the regenerative amplifier. The rf

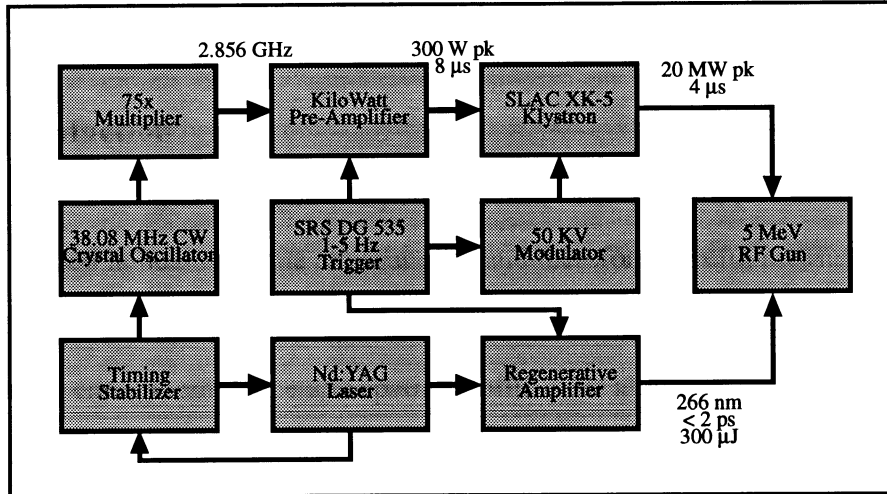


Figure 3.18: RF and Timing System Schematic

can now be amplified by the klystron to 20 MW over 4 μ s and maintains the 5 Hz repetition rate. Since the klystron is most stable when driven to saturation (≈ 20 MW), the rf power to the photoinjector is controlled by a high power variable attenuator installed in the waveguide system. Because of the high power of rf, the transport of the rf to the gun is via evacuated s-band waveguide. A vacuum of $< 10^{-7}$ Torr must be maintained to prevent breakdown in the waveguide. In the rf gun, where fields of 100 MV/m are achieved, the vacuum requirements are stricter and a vacuum of $< 10^{-8}$ Torr is required. In attaining these vacuum levels a certain amount of rf conditioning is required. Typically this takes one week of slowly increasing the rf power until full power is reached without further arcing in the gun or waveguide. A block diagram of the rf and timing systems is depicted in Fig. 3.2.18.

3.3 Electron Beam Measurements

3.3.1 Introduction

Regardless of the gun tuning, laser performance, or rf system, it is the electron beam that will be used in beam-plasma experiments, and therefore, careful measurements of the electron beam must be performed. To fully characterize the electron beam, the charge, bunch length, energy, emittance and spatial profile must all be measured. Although only the long pulse (50 ps FWHM laser pulse) electron beam was used for the plasma lens experiment, the short pulse (2 ps FWHM laser pulse) results are also presented in order to describe the performance capabilities of the photo-injector.

The beam performance depends on the gun, cathode and drive laser characteristics. While measuring the electron beam, these characteristics were varied. As was explained in Section 3.2, the gun balance depends critically on the cathode position. It is difficult to control and monitor the gun balance once the gun has been installed in the beamline. Therefore, the gun parameters were not usually changed and all measurements were conducted with a balanced gun unless explicitly noted.

Likewise, since the gun balance is extremely sensitive to cathode position and the high vacuum requirements in the gun require baking of the rf gun after exposure to atmosphere, replacement of the cathode is a difficult procedure and was only done twice. All three cathodes used were made from oxygen free high conductivity copper (OFHC) copper. The first cathode (CATH1) used was machine finished and sanded with 600 grit sand paper and then cleaned in methanol before installation. Unfortunately, the surface was damaged by the laser during operation. This cathode was replaced with a

commercially polished cathode purchased from Spawr Industries (CATH2). The best performance was achieved with this cathode, however, under high power operation, its performance degraded as will be explained in Sections 3.3.2 and 3.3.6. After measuring an order of magnitude drop in quantum efficiency, this cathode was replaced with a hand polished OFHC copper cathode prepared at UCLA (CATH3). This final cathode's performance was poor and perhaps indicates a severe contamination of the electron gun. The reason for this poor performance is currently under investigation.

In contrast, the laser characteristics are easily changed. Since copper was always the cathode material, 266 nm light was always used in order to get single photon photo-emission. However, as discussed in Section 3.2.3, the laser pulse width could be set to either 2 or 50 ps. Measurements of all the beam characteristics were made with both pulse widths but only the bunch length and emittance indicated any dependence on laser pulse width. It was also indicated in Section 3.2.3, that the laser could be injected at near normal incidence or at 70° from the normal. The quantum efficiency increased by 50% at 70° injection for p-polarized light, but, because of time delays across the cathode surface as the laser wavefronts impinge the cathode surface at 70° , the 70° injection port was abandoned after the quantum efficiency measurements were completed. Finally, the laser energy density on the cathode was the easiest parameter to adjust. This could be controlled by either controlling the energy of the laser pulse or adjusting the spot size. It was during an adjustment of the spot size on the cathode that the first cathode was damaged by a sub mm laser spot with 200 μ J of UV. Typically the spot size was maintained at 4 mm FWHM unless otherwise noted.

Another element which can be controlled easily is the rf power. Both the peak power and the phase can be varied as described in Section 3.2.4. Unfortunately, adjusting

either the phase or the peak power will also change the beam dynamics in the gun and therefore the beam transport. This made measurements involving these parameters difficult but the quantum efficiency, emittance and beam energy were measured as functions of rf peak power and laser injection phase. For these measurements the beam transport was optimized for each rf power or phase value.

The transport of the electron beam is controlled by a single solenoid lens and two kicker magnets. A simplified beamline showing the diagnostics used in characterizing the beam and their location is depicted in Fig. 3.19. The bucking solenoid depicted in Fig. 3.19 is used to zero the magnetic field on the cathode. At less than 5 MeV beam energy, the solenoid lens is very effective and quadrupole magnets were not needed to transport the beam. This made the transport of the beam easy since the solenoid symmetrically focuses the beam where as quadrupoles must be used in pairs since they focus in one plane only. As indicated in Fig. 3.19, the beam is transported to the various diagnostics where the beam characteristics are measured.

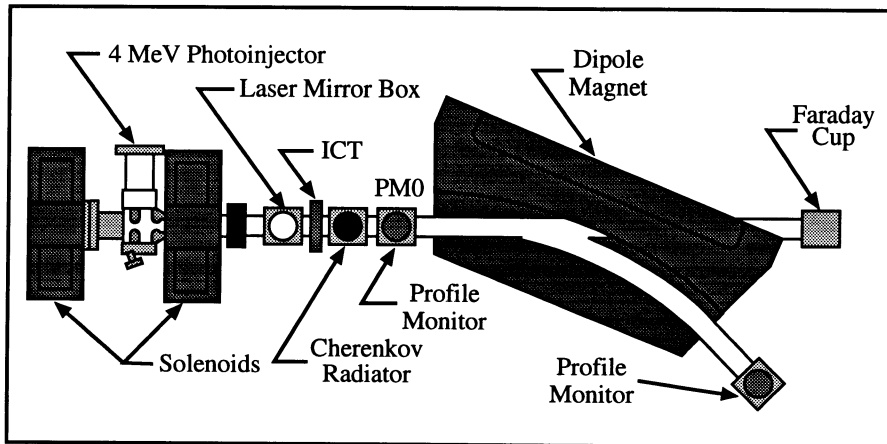


Figure 3.19: Diagnostic Beamline Schematic

3.3.2 Quantum Efficiency Measurements

The photocathode quantum efficiency is a fundamental parameter in laser driven rf guns. It has been shown that the quantum efficiency depends on the wavelength, injection angle, and polarization of light used in producing electrons[56]. Furthermore, the quantum efficiency is strongly affected by experimental conditions such as the cathode surface, vacuum conditions, and the applied electric field[57].

In most quantum efficiency experiments, special consideration is given to the collection of all the charge produced by the injected photons. Since the purpose of the rf photo-injector is to create an electron beam, the charge contained in the electron beam at the output of the rf gun was measured and used in the calculation of quantum efficiency. Therefore, this measurement defines an effective quantum efficiency of the photo-injector rf gun system which incorporates the collection efficiency of the beam. Except in cases where saturation of beam charge as a function of laser energy occurred, this effective quantum efficiency should equal the actual quantum efficiency of the copper cathode.

The electron charge is measured with two independent diagnostics: the Faraday cup and the Integrating Current Transformer (ICT). Both these diagnostics agree with each other to within 10%. The Faraday cup was constructed from carbon in the form of a 1/2" diameter cylinder of 1" in length. Carbon was chosen because of its low Z to reduce Bremsstrahlung and backscattering. The length of the cylinder corresponds to two stopping distances for 5 MeV electrons and therefore all the electrons will be stopped in the carbon. The Faraday cup is mounted in a 1.5" diameter beam pipe using a boron nitride ring which supports and electrically isolates it. The electron beam charge is integrated and the peak voltage is read. The charge is equal to the capacitance of the Faraday cup and associated signal cables times the voltage measured. This capacitance is

typically 0.3 nF.

The Faraday cup is an excellent charge diagnostic, however, because it is an integrating device, it collects the dark current. The dark current consists of electrons produced by field emission near the peaks of the rf cycle. Over 12,000 electron bunches from this dark current are created during the 4 μ s rf pulse from the klystron. These bunches are 350 ps apart (corresponding to the period of the rf) and less than 100 ps long. Under optimum focusing conditions, the dark current can contain >10 nC of charge. This is a large background in comparison to the photoelectron beam whose charge is always less than 3 nC. The dark current is very consistent and this background can be subtracted, however, it decreases the signal to noise ratio and limits the resolution of the Faraday cup to less than 1/4 nC of photoelectrons. Furthermore, the charge measurement depends critically on the capacitance measurement which is limited to 10%. For these reasons the Faraday cup was used only to confirm the calibration of the ICT.

The ICT gives a background free measurement of the photoelectron beam charge. This device (manufactured by Bergoz of France) couples to the magnetic field produced by the electron beam as it passes through the ICT. The magnetic field is enhanced in a magnetic core which encircles the beam line azimuthally. The special alloys used in the core construction have a very high magnetic permeability. The magnetic core is wrapped with a single turn winding which is terminated by a capacitor. The capacitor integrates the current produced in the windings by the magnetic field. Both the magnetic core and the capacitor serve to lengthen the induced signal to about 8 ns. The capacitor discharges through the same single turn winding again producing a magnetic field in the alloy core. Another winding about the magnetic core which is terminated by a 50 Ω load acts as a very high impedance probe for reading the induced voltage across the capacitor. In this

process, the two windings about the magnetic core act as a transformer. By adjusting the turn ratio, the output pulse length and amplitude are changed. With a turn ratio of 10:1, the output is always 20 ns regardless of the input pulse length as long as the input pulse is less than 1 ns. Both the peak voltage and the integrated voltage are proportional to the beam charge independent of beam pulse length and beam position.

The ICT provides a measurement of the photoelectron beam charge which is independent of the dark current background. As was mentioned above, the dark current is comprised of >10 nC of charge distributed over 12,000 electron bunches. Because of a 2 μ s buildup time before the rf reaches full power in the gun, most of the dark current is contained in the last 6000 electron bunches. The charge per bunch is therefore < 4 pC. This charge level is near the limits of detectability of the ICT and is insignificant when compared to the photoelectron charge of 1 nC per bunch.

The 10% accuracy of the ICT was well within the shot to shot charge fluctuations produced by the laser. Fluctuations in the laser amplitude up to 50% from shot to shot were observed. Because of these unpredictable fluctuations a single shot data acquisition system was implemented. As mentioned above in Section 3.2.3, the laser energy is measured for each shot with a photodiode and the ICT produces a 20 ns pulse whose integrated voltage is proportional to the electron charge. Therefore, the laser energy and beam charge are measured and recorded for each shot by our data acquisition system.

The first quantum efficiency measurements were conducted with CATH1 for both 2° and 70° incidence. The laser injection geometry is shown in Fig. 3.20. The polarization angle ϕ is the angle the electric field makes with respect to the plane of incidence. Therefore, 0° corresponds to p-polarized light and 90° corresponds to s-polarized light. A 1/2 waveplate allows continuous rotation of the laser polarization through a full 360°.

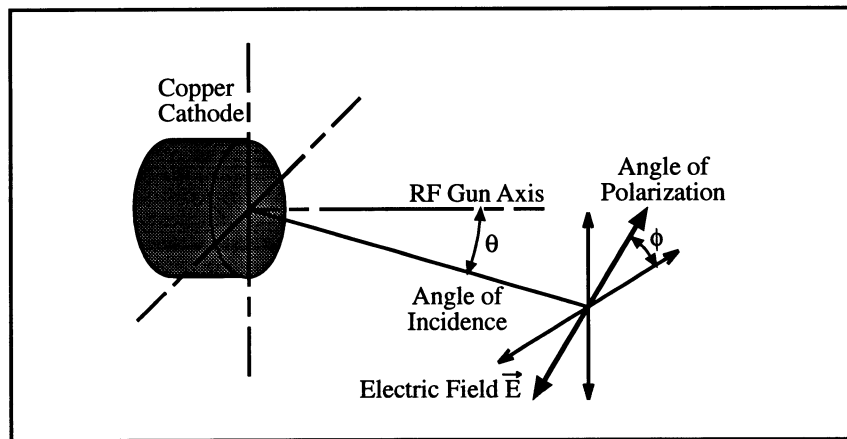


Figure 3.20: Laser Injection Geometry

The angle θ refers to the angle of incidence of the laser beam with respect to the beam axis of the electron gun. Unfortunately, before any measurements were complete, the laser was accidentally focused to sub mm spot sizes on the cathode. This produced what appeared to be enhanced emission of up to 100 nC per pulse as measured by the Faraday cup, however, the ICT showed that the pulse duration lasted hundreds of nanoseconds. This emission was determined to be enhanced field emission similar to that observed at BNL [58]. The enhanced emission occurs when the laser pulse ablates the cathode surface which sparks a plasma discharge in the large rf fields. This investigation of enhanced field emission resulted in a $2 \times 4 \text{ mm}^2$ damaged spot on the cathode. Therefore, most measurements using CATH1 utilized the damaged portion of the copper cathode for photo-emission.

During operation the gun became unbalanced such that the fields in the full cell were 80% larger than those in the 1/2 cell. This limited the maximum electric field on the cathode to less than 50 MV/m and resulted in the saturating shown in Fig. 3.21. The Fowler-Dubridge theory for one photon photoelectric effect predicts a linear dependence

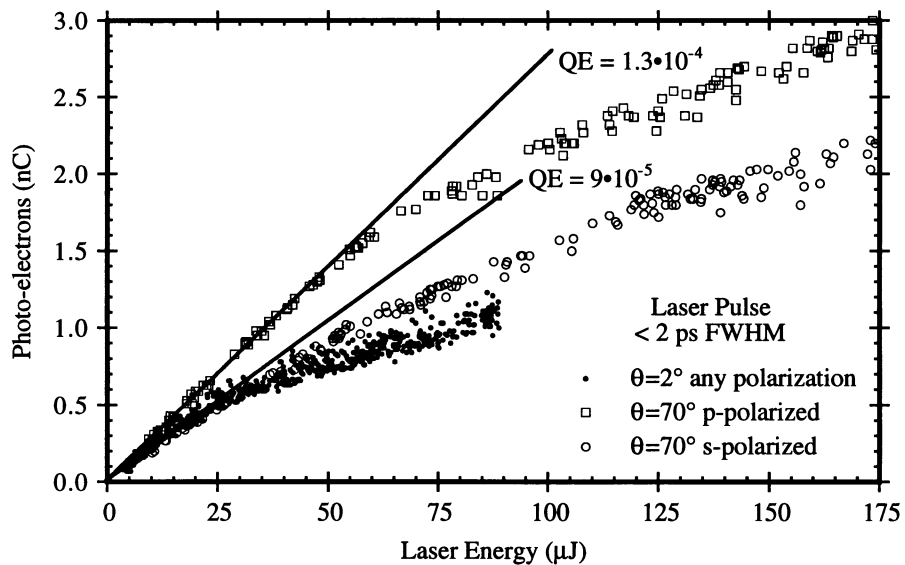


Figure 3.21: Measurement of Charge as a Function of Laser Energy for an Unbalanced RF Gun

of charge production on incident laser energy. However, the measured charge vs laser energy manifests a saturation of charge output for laser energies above 50 μJ . The saturation can be explained by space charge effects near the cathode surface. When the electrons are produced by the laser pulse, they are emitted as a thin disk from the cathode: approximately 80 μm thick and 1 mm in diameter corresponding to the laser spot size on the cathode. The space charge electric field between the electron bunch and the cathode can be approximated by a surface charge density and its image charge in the cathode. Using this simple model, a space charge field equaling the accelerating field of 50 MV/m results from only .25 nC of charge. This value agrees with the 0° data.

The particle accelerator code, PARMELA, has been used to model this space charge effect. This code calculates the space charge forces between a user specified number of test particles as the particles are accelerated from the cathode in an rf gun. However, experimentally the space charge problem is complicated by the cathode damage. Because

of this damage, most of the electrons could be produced from microemitters on the cathode surface [58][59]. At these emitters the space charge could be worse. Despite these limitations in the computer modeling, the PARMELA simulation showed saturation similar to that of experimental data.

Therefore values of quantum efficiencies are taken in the low charge limit. Linear fits for laser energies below 25 μJ result in quantum efficiencies of 1.3×10^{-4} and 9×10^{-5} for 70° and 2° injection respectively and are labeled with the quantum efficiency (QE) corresponding to the slope of the line. From these fits, an enhancement in quantum efficiency of 50% is observed for 70° p-polarized over 70° s-polarized light. Measurements of charge vs laser energy were obtained for various polarization angles. For 2° injection, changing the polarization angle did not affect the charge collected. However, for 70° injection, measurements resulted in curves of similar shape to those of Fig. 3.21 but which lie in between the 70° s-polarized and 70° p-polarized curves depending on the angle of polarization. Fig. 3.22 shows the polarization dependence of collected charge for a laser energy of 100 μJ . Identical plots are found at different energies. The functional form of this enhancement fits a $\cos^2 \phi$ dependence which implies that the enhancement is dependent on the energy of p-polarized light rather than its electric field. The increase in quantum efficiency for p-polarized vs s-polarized injection is probably due to the difference in the reflectivity of copper at these polarizations. The reflectivity of a copper mirror was measured as a function of incident angle for both s- and p- polarized 266 nm light. According to the generalized Fowler-Dubridge theory, the quantum efficiency is proportional to absorbed laser energy. Therefore, a 90% increase in absorption was measured for p-polarized light over s-polarized light predicting a 90% improvement of the quantum efficiency for p-polarized

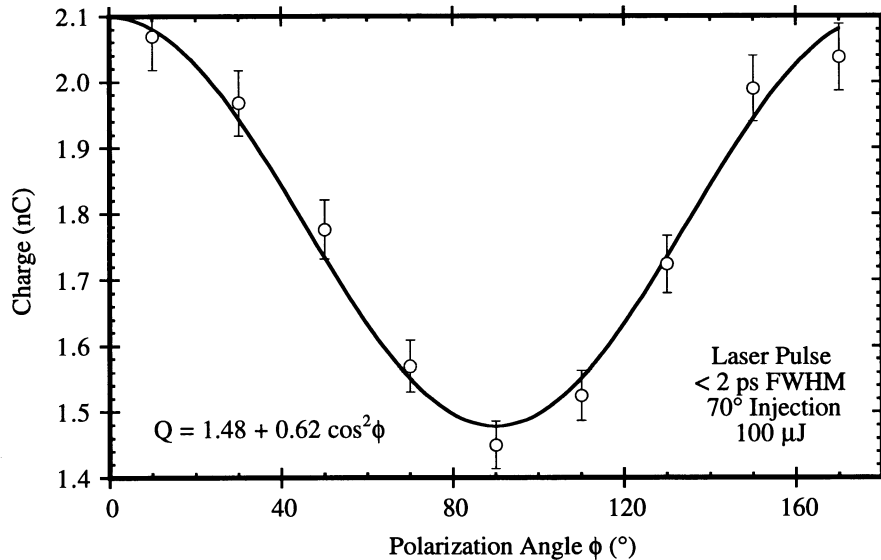


Figure 3.22: Measurement of Charge as a Function of Incident Polarization for 70 $^\circ$ Laser Injection injection. The measured enhancement was only 50%. This discrepancy is probably due to a difference in the relative reflectivities of the damaged cathode in comparison to those of the copper mirror.

In order to improve the beam quality and quantum efficiency, the damaged cathode was replaced with a commercially polished cathode (CATH2) purchased from Spawr Industries. It was polished to $\lambda/4$ at .6 μ m flatness and 40/20 scratch and dig. Because this cathode was mirror finished, the rf conditioning was carefully monitored in order to prevent damage to the cathode surface.

CATH2 was installed in late August, 1994 and rf conditioning continued for 3 months. Rf breakdown was observed throughout the conditioning process during which the rf power was increased in steps until the occurrence of rf breakdown events reached a prescribed limit of less than three consecutive rf breakdowns and less than a 1% occurrence of breakdown events over a 15 minute interval. When the frequency of breakdown events fell below this limit the rf power was increased until the number of

breakdown events once again approached this level. Using this guideline, the rf power was slowly increased until an input power of 5 MW was achieved.

In early December the rf power was raised to 7 MW and the first quantum efficiency measurements were made. These resulted in quantum efficiencies of 1×10^{-4} . Since the rf gun was rebalanced during the installation of the new cathode, higher fields were attained on the cathode and the photo-electron charge vs laser energy plots (Fig. 3.23) did not show the saturation effects seen with CATH1. The quantum efficiency was also

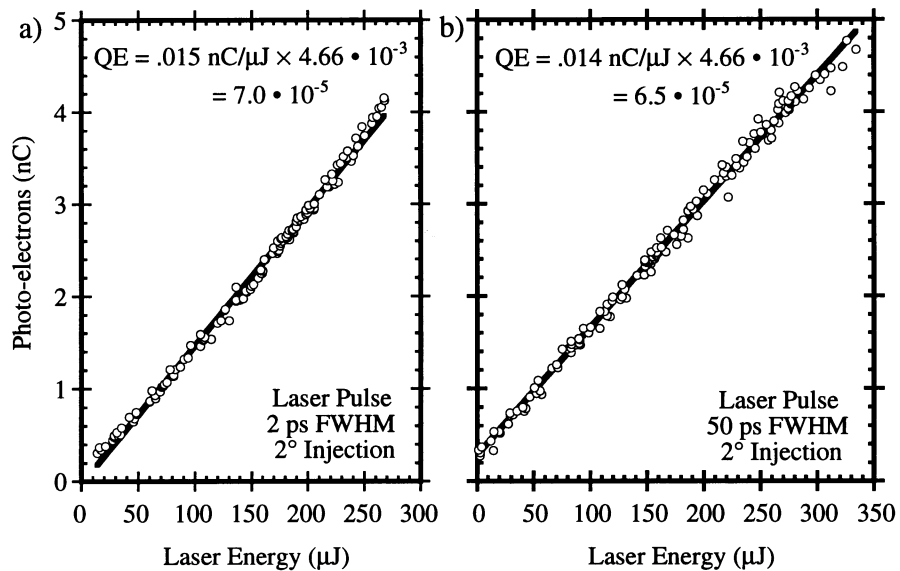


Figure 3.23: Measurement of Charge as a Function of Laser Energy for a Balanced RF Gun measured as a function of rf power and laser injection phase. Fig. 3.24 shows an increase in quantum efficiency with increasing rf power in agreement with Schottky reduction of the work function from large electric fields present at the cathode surface ($> 50 \text{ MV/m}$). These three data points are plotted with a low field quantum efficiency measurement done in a DC gun as functions of \sqrt{E} in Fig. 3.25 and fit with the Schottky work function reduction model. The same effect is seen in the measurement of charge as a function of laser injection phase. As the injection phase increases the quantum

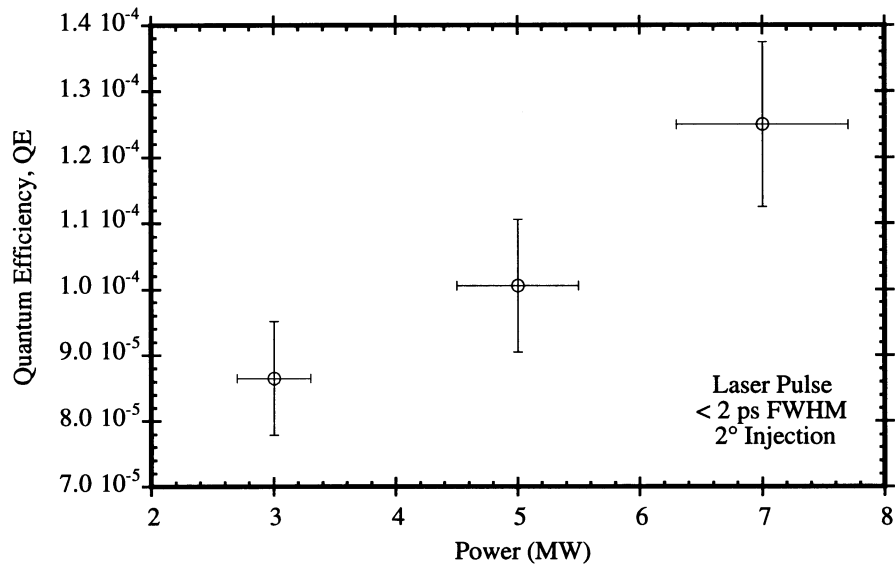


Figure 3.24: Measurement of QE as a Function of RF Power Coupled to the Gun efficiency increases due to increased electric field on the cathode at the time of injection. This increase in quantum efficiency combined with the transport losses which occur in the rf gun due to rf gun dynamics result in the curve depicted in Fig. 3.26. PARMELA

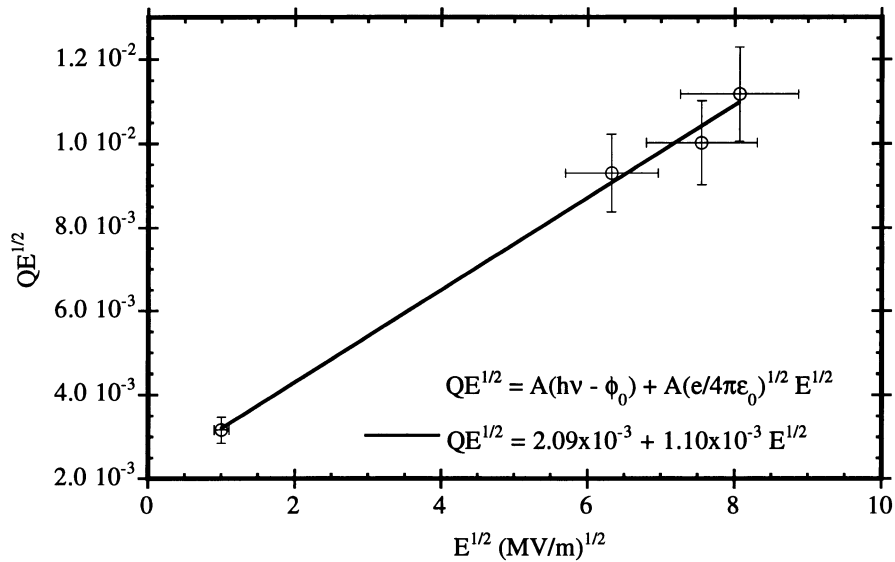


Figure 3.25: Measurement of QE as a Function of Field Gradient

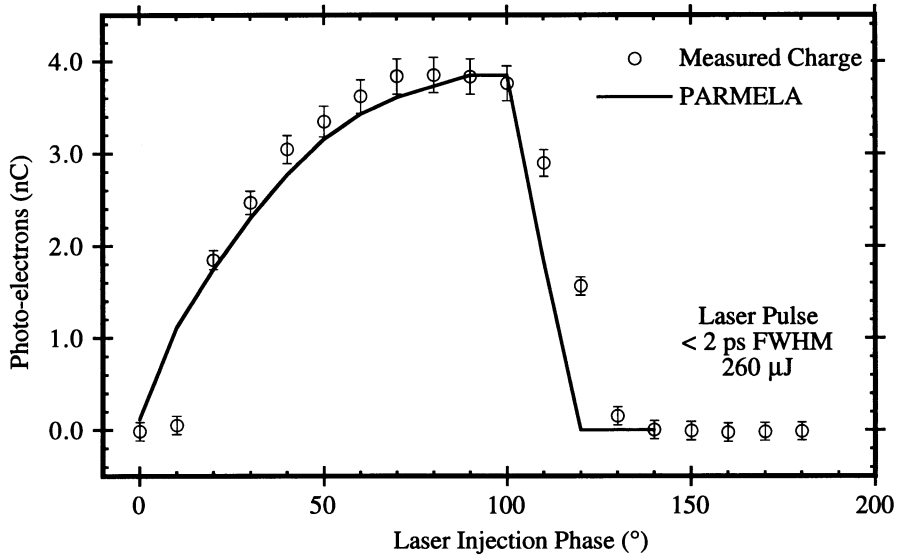


Figure 3.26: Measurement and Simulation of Charge as a Function of Laser Injection Phase

was used to model this effect using the measurement of quantum efficiency as a function of rf power to model the electron emission from the cathode for various phases. The quantum efficiency was remeasured in late December and resulted in values 40% lower than those measured earlier that month.

However, in January, the quantum efficiency dropped to 1×10^{-5} . The drop in quantum efficiency was accompanied by structured emission from the cathode surface which will be described in detail in Section 3.3.6. It was discovered that by keeping the gun under vacuum without rf power for a few days, the quantum efficiency would recover to a level of 2.6×10^{-5} (still below the levels recorded in December). This level could be maintained for many hours as long as the rf power level was maintained below 6 MW. However, once the rf power was increased to 7 MW, the quantum efficiency deteriorated quickly. In just 7 hours the quantum efficiency dropped from 2×10^{-5} to 1×10^{-5} , a factor of 2. This test was done with the gun vacuum isolated from the rest of the beamline which is typically maintained at slightly higher pressures (1×10^{-6}). A residual

gas analyzer was used to measure the primary contaminants of the vacuum system which were H₂O, H₂, N₂, O₂, Ar and CO₂ in order of decreasing partial pressure.

In an attempt to increase the quantum efficiency, the cathode surface was damaged using the focused UV laser beam as had been done with CATH1. The laser was focused to a 200 μm spot and an array of 5 by 5 damaged spots was created at the cathode center. It was expected that further reduction of the work function could be achieved through the Schottky effect with enhanced electric fields at the surface due to the microprotrusions created by the laser damage. In the initial operation of the rf photoinjector with CATH1 quantum efficiencies of 1×10^{-4} were routinely measured from a damaged copper photocathode and no quantum efficiency degradation was ever observed. However, on CATH2, the damaged areas did not produce any change in the quantum efficiency and the recovery and degradation of the quantum efficiency continued as described above.

Following the removal of the commercially polished cathode, a third copper cathode, was prepared at UCLA (CATH3). It was machined from OFHC copper using "Marvel's Mystery Oil" as lubricant. The cathode surface was then polished starting with wet 600 grit sand paper and working down to .3 μm diamond grit. The polishing was done by hand until no surface feature was larger than 1 μm. The cathode was stored in methanol until installation in the rf gun. This cathode was also tested in a dc gun prior to installation in the rf gun and a quantum efficiency of 1×10^{-5} was measured[60].

During the cathode installation, the rf gun was back filled with nitrogen and maintained at the operating temperature of 55° C. Once vacuum of better than 1×10^{-7} was achieved, the rf conditioning was started. Within a few hours rf power levels of 5 MW were achieved with practically no signs of rf breakdown.

The quantum efficiency was immediately measured to be 3.3×10^{-5} at an rf power

level of only 4 MW. Based on the previous measurements of quantum efficiency as a function of rf power, this would imply a quantum efficiency of 5×10^{-5} at 7 MW. Furthermore, the beam showed no indication of beam structure. Two days later, following less than 8 more hours of conditioning which was characterized by minor breakdown in the gun, rf power levels of 6 MW were attained. The quantum efficiency was again measured and resulted in a reduction from the previous value of more than a factor of 2 to 1.5×10^{-5} . Following the beam quality measurements, this cathode was removed from the rf gun and immediately taken to the dc gun test stand for quantum efficiency measurements. The measurements did not indicate any change in quantum efficiency, again measuring 1×10^{-5} and also did not show any indication of structure on the cathode surface.

The electron emission from a copper photocathode in a rf photoinjector appears to degrade in time while under large electric fields (>50 MV/m). The cathode can be “recharged” by leaving the cathode under 10^{-8} Torr vacuum in the rf gun but without running rf power in the gun. The mechanisms for both the cathode quantum efficiency degradation and the recovery in the UCLA gun are unknown and more careful and detailed study is necessary to understand the interaction of the copper surface with both the large rf fields and the UV laser pulses present in rf photoinjectors.

For the overdense plasma lens experiment, CATH1 was used. There was no observed cathode degradation during the experiment, however, as was mentioned above, the cathode was damaged by the UV laser pulses prior to its use for the overdense plasma lens experiment. Furthermore, the imbalance of the 1/2 cell to full cell fields was not discovered until the plasma lens experiment was complete so that the electron beam charge was limited by saturation shown in Fig. 3.21. As shown in Fig. 3.21, the laser

energy on the cathode was limited to 90 μJ for 0° injection. This limit was due to a damaged laser mirror in the vacuum mirror box. The reflectivity of this mirror was measured after the plasma lens experiment to be 50% therefore accounting for the difference in laser energy on the cathode for 0° injection as opposed to 70° injection. 0° injection was used for the plasma lens experiment since it produced better beam quality than the 70° injection. Therefore, the maximum charge available for the overdense plasma lens experiment was 1.2 nC and therefore the underdense plasma regime could not be accessed.

3.3.3 Bunch Length Measurements

Although photoemission is a prompt process down to sub picosecond time scales, the production of very short (< 2 ps) electron beams from a photocathode rf gun cannot be taken for granted. When a few nC of electrons are produced from a < 1 cm^2 surface area, the space charge electric field can reach many MV/m. This large electric field acts to disperse the electron bunch radially and longitudinally, thereby leading to bunch lengthening. As was discussed in Section 3.2, photocathode rf guns are constructed to minimize bunch length growth by allowing the creation of the electron bunch in high electric fields (up to 100 MV/m). Under these fields, the electrons are accelerated to relativistic velocities in less than one centimeter. Once the beam is relativistic, the effect of the longitudinal electric field drops as $1/\gamma$ due to the increase in electron mass. Therefore, most of the bunch length growth occurs before the beam becomes relativistic and before the beam exits the rf gun.

The electron bunch length is measured using a Cherenkov radiator viewed by a streak camera. The radiator is placed as close to the exit of the rf gun as possible given physical

constraints. Only a solenoid is used to transport the beam to the radiator as shown in Fig. 3.19.

A 250 μm thick fused silica etalon served as the Cherenkov radiator. The etalon side where the electron beam entered was sanded forming a diffuse surface to prevent signal lengthening due to multiple reflections. Furthermore, the beam entrance side of the etalon was covered with a 0.005" thick aluminum foil which provides grounding of the Cherenkov radiator and prevents any scattered laser light from entering the field of view of the Cherenkov light. The etalon was attached on a mount which was externally rotatable about an axis perpendicular to the beam. For a relativistic electron beam, the angle of Cherenkov radiation with respect to the beam axis is

$$\theta = \cos^{-1}\left(\frac{1}{n}\right) \quad (27)$$

where n is the index of refraction of the medium. For fused silica $n = 1.46$ and therefore $\theta_0 = 47^\circ$. To further minimize any reflection at the fused silica and vacuum interface, the incidence angle of the Cherenkov light at that interface should be set to Brewster's angle. In this case Brewster's angle is 35° . This requires the etalon to be tilted at 12° from the perpendicular to electron beam causing the Cherenkov light to refract at 57° from the beam axis at the vacuum interface. Given the geometrical constraints of the vacuum cross, the Cherenkov light had to be directed away from the beam axis by at least 73° in order to clear the vacuum pipe. Therefore the etalon was tilted only 8° from perpendicular to the beam axis (only 4° off Brewster's angle). The Cherenkov radiator setup is depicted in Fig. 3.27.

This Cherenkov radiator allows 1 ps time resolution based on the maximum time delay between any two Cherenkov photons created by an infinitely thin electron beam. The

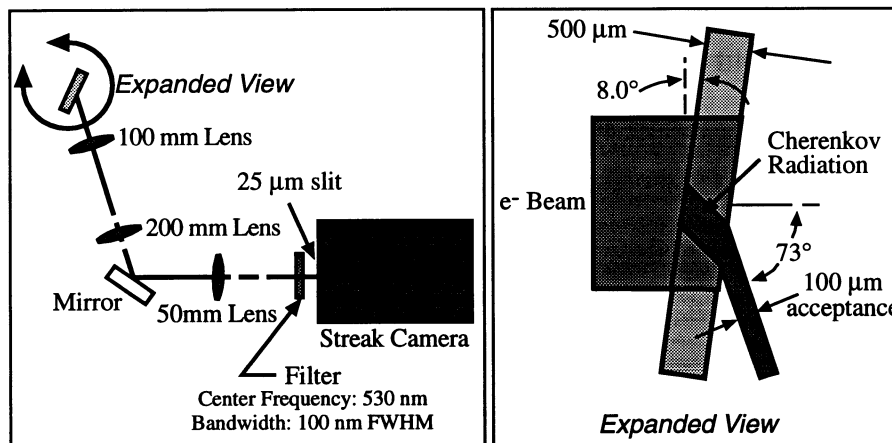


Figure 3.27: Cherenkov Radiator Setup

limiting factor in the bunch length measurements is the streak camera. We used a Hadland Imacon 500 streak camera. At the fastest sweep speed of 20 ps/mm, the time resolution is no better than 3.5 ps. The streak camera resolution was verified by streaking the laser pulses as described in Section 3.2.3. When combined with the resolution of the streak camera, the overall resolution of the Cherenkov streak system is 3.6 ps.

The streak camera cannot be installed such that it directly views the Cherenkov detector because of the high levels of radiation inside the lead shielding. Therefore the Cherenkov light is transported through a maze in the lead shielding. Because the light intensity levels are near the detection limits of the streak camera, the Cherenkov image is reduced by a factor of 4 when focused on the streak camera slit. To achieve 3.5 ps resolution, a 25 μm slit is used at the entrance to the streak camera. Accounting for the 400% reduction in image size, the 25 μm slit infers a 100 μm acceptance at the Cherenkov radiator. This 100 μm acceptance leads to the 1 ps resolution of the Cherenkov probe mentioned above. Because the Cherenkov light has a very large bandwidth, in order to achieve the best

resolution a frequency filter must be used to eliminate chromatic dispersion effects from the transport line to the streak camera. A BG18 filter and a VG9 filter were used to allow only a 100 nm bandwidth of light centered about 530 nm.

A typical Cherenkov streak of the electron bunch is depicted in Fig. 3.28. The streak

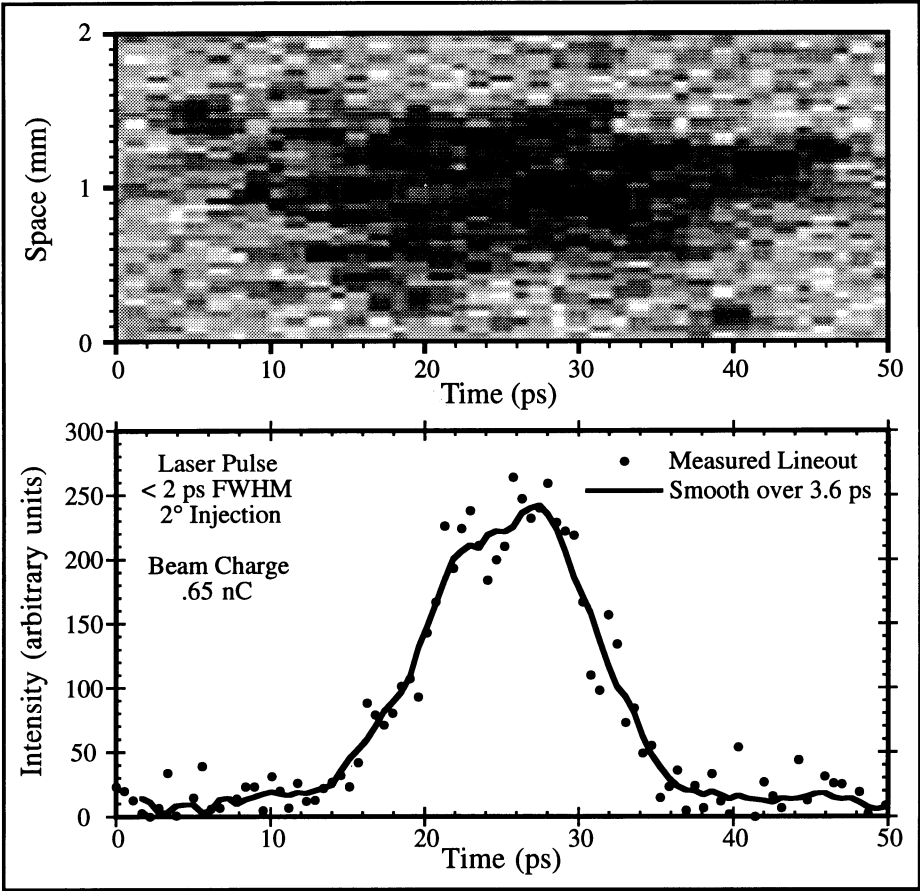


Figure 3.28: Cherenkov Streak Measurement of the Electron Beam

image appears spotted due to the low light levels incident on the streak camera. Low light levels are required to avoid space charge lengthening in the streak camera and to achieve 3.5 ps resolution as was done when streaking the laser pulse. In analyzing Cherenkov streaks, the images are integrated along the space axis to provide better statistics. Each

array element corresponds to 0.56 ps. Since the Cherenkov streak system resolution is 3.6 ps, a smoothing algorithm is used to average over the 6 nearest neighbors in the integrated array.

All the bunch length measurements were made using CATH1. Although there were plans for measuring the bunch length with CATH2 and CATH3, because of the degradation of quantum efficiency which occurred, the bunch length measurement was postponed until a suitable cathode is found or the degradation can be controlled. Therefore, the bunch length measurements were made under the unbalanced gun conditions described above for CATH1 *i.e.* the electric field ratio between the 1/2 cell and the full cell was measured to be 1:1.8. This limited the maximum electric field on the cathode to less than 50 MV/m and the electron energy to 3.5 MeV. Furthermore, recall that the cathode was damaged by the laser before any measurements were taken. Therefore, most of the electron bunch length measurements were made for electrons produced from the damaged area. However, with careful alignment of the laser, the damaged area could be avoided and some streaks from the undamaged region of the cathode were also taken.

The first streak measurements were taken with 70° laser injection. Laser injection at 70° produces bunch lengthening from a time delay across the cathode as the laser wavefront strikes it. This produces an electron beam with a linear space time correlation. This correlation is present in the Cherenkov streak shown in Fig. 3.29. A laser spot size of 2 mm produces a time delay of

$$\tau = \frac{2 \text{ mm}}{c \cos(70^\circ)} \approx 20 \text{ ps} \quad (28)$$

The measured delay from the streak in Fig. 3.29 was 25 ps. When the streak is corrected

for the delay across the wavefront, the measured pulse width becomes 13 ps.

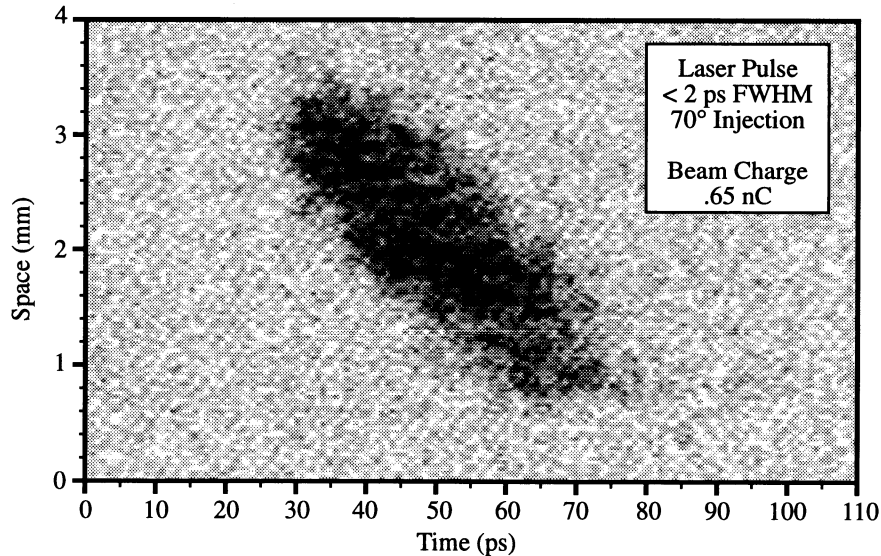


Figure 3.29: Streak Measurement of Electron Beam with 70° Laser Injection

At 2° injection, the time delay across the cathode is insignificant and the Cherenkov streaks indicate the electron bunch length directly. By focusing the laser spot to 2 mm, we were able to move the laser spot to an undamaged portion of the cathode. A streak from the undamaged cathode is depicted in Fig. 3.30. Streaks from the damaged portion of the cathode resulted in slightly longer bunches due to an elongated tail as seen in Fig. 3.31.

Bunch length measurements with the Cherenkov radiator and streak camera resulted in 9 ps to 15 ps FWHM for various charge levels from .2 nC to 2.6 nC, however, no correlation was found between the bunch length and the charge output from the rf gun.

All the streak camera measurements indicate electron bunch lengths longer than 8 ps. Measurements for 2° incidence on the undamaged portion of the cathode provide the shortest bunch length measurements averaging 12 ps. However, the 2° measurements from damaged parts of the cathode clearly characterize longer bunches with more time

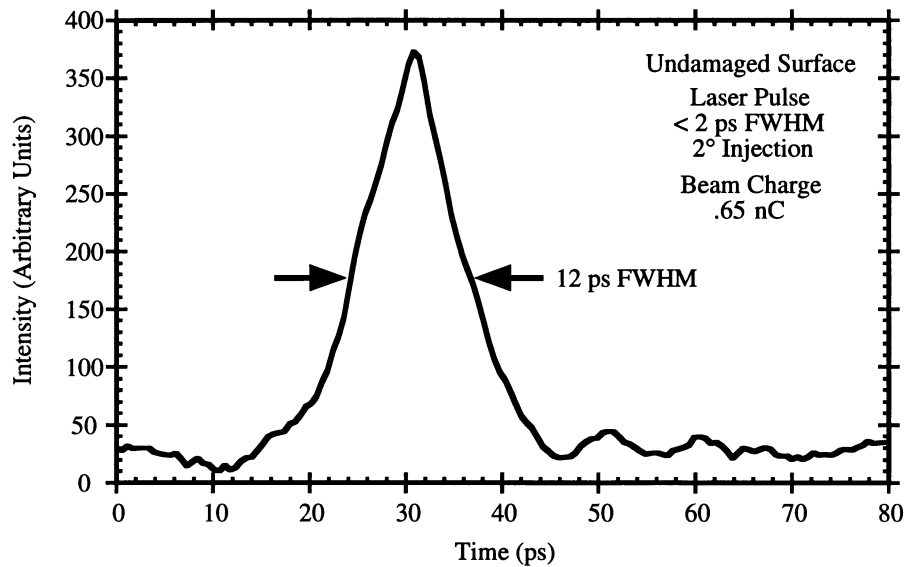


Figure 3.30: Streak Measurement of Electron Beam from Undamaged Cathode Area structure and long tails. These measurements contradict the assumption that electron bunches will mimic the laser pulses in time.

One source for bunch lengthening is space charge. The quantum efficiency data for

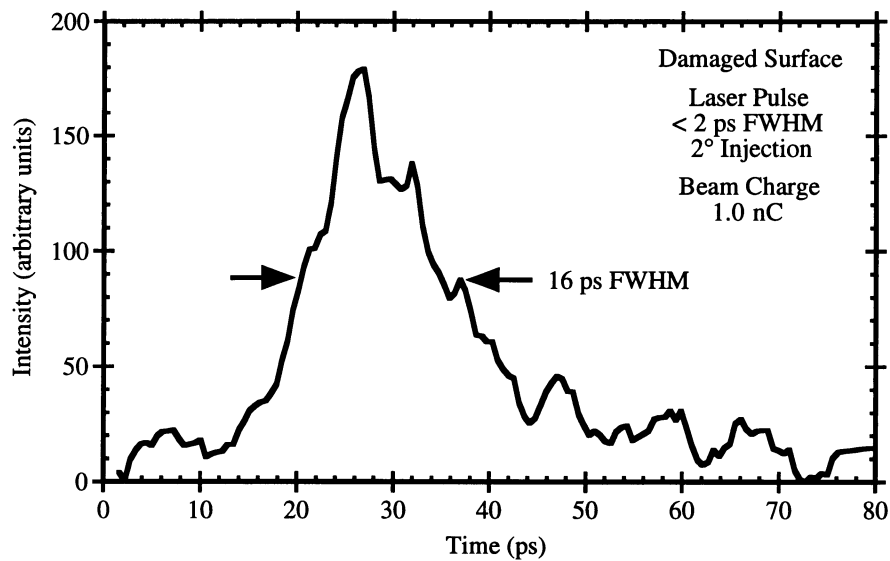


Figure 3.31: Streak Measurement of Electron Beam from Damaged Cathode Area

CATH1 indicated significant reductions in charge production due to space charge. Microemitters can further aggravate this problem possibly accounting for pulse lengthening and time structure of the streaks from damaged portions of the cathode. PARMELA simulations were performed for various output bunch charge levels from 100 pC to 1.3 nC. These simulations show a bunch lengthening as output charge is increased. For typical charge levels between 0.4 nC and 1.0 nC PARMELA predicts bunch lengths from 9 ps to 15 ps. These bunch length predictions are within the scatter of the measured bunch lengths, however, the measurements did not indicate a correlation with charge level.

For the overdense plasma lens experiment, the longest possible electron pulses were desired since the object of the experiment was to measure time dynamic response of the plasma lens. Therefore 50 ps laser pulses were used to produce the electron bunch for the overdense lens experiment. The 50 ps laser pulses were symmetric gaussian pulses

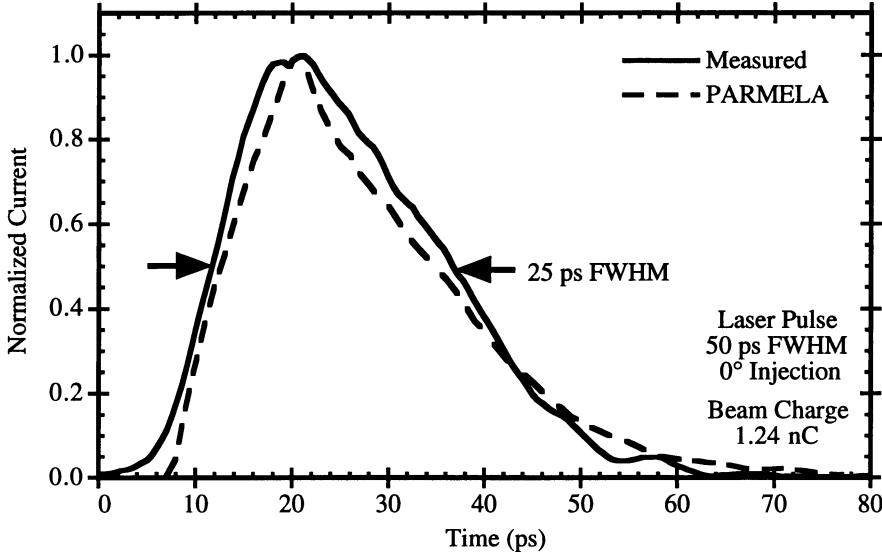


Figure 3.32: Streak Measurement and Simulation of Electron Beam Generated by 50 ps Laser Pulse

in time, but the electron bunch produced in the rf gun was an asymmetric pulse with 25 ps FWHM as seen in Fig. 3.32. This characteristic bunch length shape with a 10 ps rise time and a longer tail arises from the time dynamics of the rf gun. The 50 ps FWHM laser pulse input on the photocathode was modeled with PARMELA and the characteristic shape was reproduced as seen from Fig. 3.32. The sharp rise of the electron bunch excited wakefields in the plasma and the long duration of the bunch allowed for measurements of the time dynamics out to 60 ps as will be shown in Chapter 4.

3.3.4 Energy Measurements

The measurement of the beam energy is important not only as a characteristic of the electron beam which is critical for understanding and predicting beam propagation, but also as a diagnostic for characterizing the photoinjector performance. Knowing the beam energy and assuming the rf gun remains balanced from the gun tuning, the electric fields in the gun can be predicted. Furthermore, by measuring the beam energy as a function of rf power coupled into the gun, the shunt impedance, which is a measure of the photoinjector efficiency, can be determined.

The beam energy is measured with a dipole magnet and a phosphor screen. The dipole spectrometer is a 45° sector magnet as depicted in Fig. 3.19. As the beam passes through the dipole magnet it is deflected by the magnetic field such that the beam trajectory traces an arc whose radius is

$$r = \frac{\gamma\beta m_e c}{eB} \quad (29)$$

where $\gamma = 1/\sqrt{1-\beta^2}$, $\beta = v/c$, m_e is the electron mass, c is the speed of light, e is the charge of the electron and B is the magnetic field in the dipole. The reference trajectory

radius defined by the sector magnet and the beamline is 0.667 m. Therefore, solving for γ and replacing m_e , e , c , and r by their numerical values leads to:

$$\gamma = \sqrt{1 + \left(\frac{eBr}{m_e c}\right)^2} \quad (30)$$

and

$$\gamma = \sqrt{1 + 1.52 \times 10^{-3} B^2} \quad (31)$$

where B is given in Gauss. The magnetic field inside the dipole is extremely uniform and for currents larger than one ampere is given by

$$B = -98.556 + 140.49 I \quad (32)$$

where I is given in amperes and B is returned in gauss. For currents less than 1 ampere, the magnetic field is no longer linear with the supply current but the beam energy was always large enough to require a supply current greater than 1 ampere. Despite the uniform magnetic field within the sector magnet, at the edges the fringe field provides a small additional kick which can be included in the energy calculation by multiplying the magnetic field by a fringe correction factor of 1.035. The beam energy is therefore given by

$$E = \gamma m_e c^2 = .511 \sqrt{1 + 1.6293 \cdot 10^{-3} (-98.556 + 140.49 I)^2} \quad (33)$$

where E is in MeV and I is in amperes. In measuring the beam energy, the supply current required to bend the electron beam onto the phosphor screen is recorded and used to calculate the beam energy in the formula given above. Due to uncertainty of the placement of the phosphor screen relative to the reference trajectory center and due to difficulties in transporting the high peak current electron beam (> 100 Amps) around the

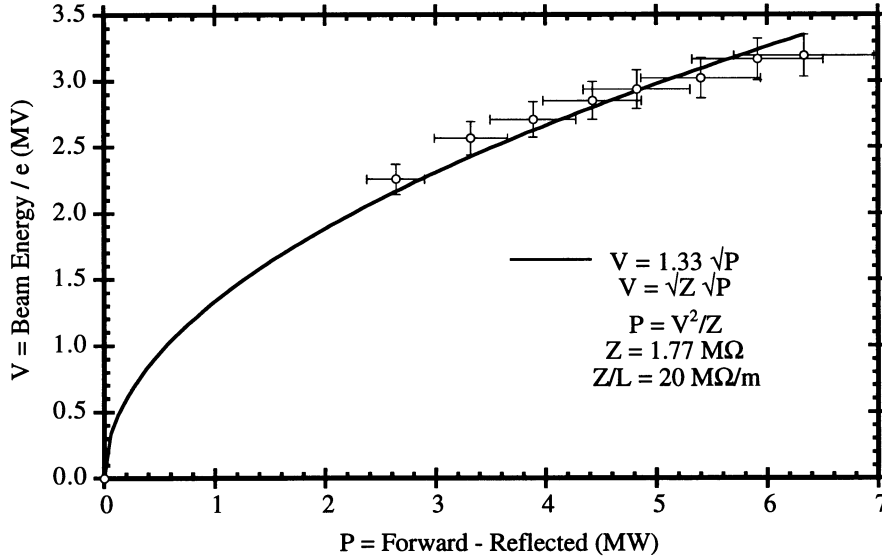


Figure 3.33: Measurement of Beam Energy as a Function of RF Power in the Gun

bend, the beam energy measurement was accurate to no better than $\pm 5\%$.

The beam energy was measured as a function of rf power and is plotted in Fig. 3.33. Since the energy also depends on the laser injection phase, the maximum energy was measured as a function of rf power. Using this data and the standard voltage power relationship

$$P = \frac{V^2}{Z} \quad (34)$$

where P is the power in the gun, V is the beam voltage and Z is the shunt impedance, the shunt impedance is determined to be

$$Z = 1.77 \text{ M}\Omega \quad (35)$$

This relation can be used to predict the beam energy given the rf power in the gun. From the beam energy the electric fields in the gun can be inferred using PARMELA. A plot of maximum energy as a function of electric field in the gun is shown in Fig. 3.34. Also

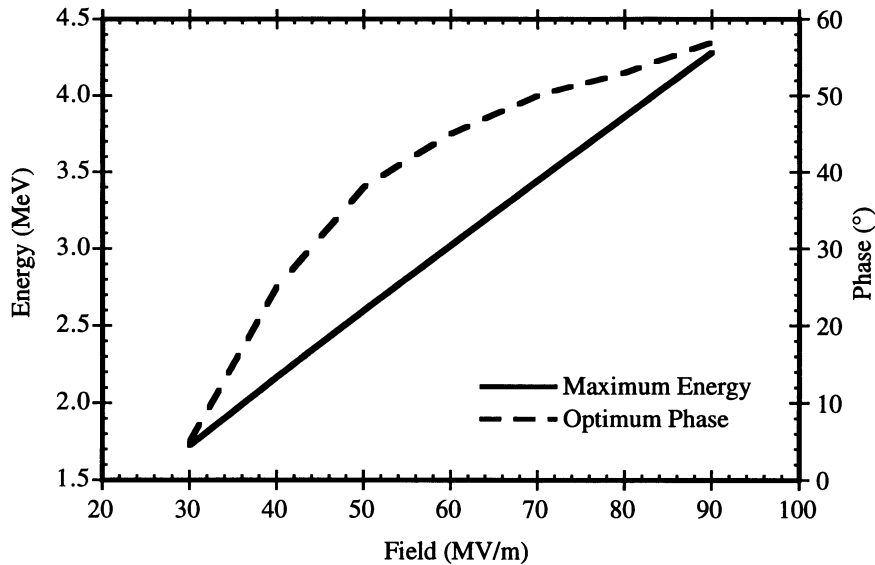


Figure 3.34: Energy and Phase as Functions of Electric Field for Optimal Acceleration

shown in Fig. 3.34 is the optimum phase which produces the maximum energy at a given electric field. By using the shunt impedance and Fig. 3.34, The electric field on the cathode can be determined and used in the calculations of quantum efficiency as was done in the calculation of charge as a function of phase in Section 3.3.2.

During the overdense plasma lens experiment, the beam energy was maintained at 3.5 MeV resulting in a γ of 7. In the previous two sections, the electron charge was demonstrated to be adjustable from 0.1 - 7 nC and the bunch length shown to be less than 30 ps. The peak current, therefore, ranges between 5 Amps and 300 Amps. Since the beam energy is low and the peak beam current is relatively large, for spot sizes ≈ 1 cm, the beam propagation is space charge dominated for beam emittances $< 10 \pi$ -mm-mrad [39].

3.3.5 Emittance Measurements

As was described in the introduction to Section 3.2, the emittance of an electron beam produced by an rf gun is dependent on the gun tune, the laser injection phase and the space charge of the electron bunch. In addition to the inherent beam emittance due to the temperature of the electrons as they leave the cathode, rf induced emittance growth and space charge emittance growth contribute to the total beam emittance. Rf emittance growth in the photoinjector is caused by radial electric fields in the gun while space charge emittance growth is the result of Coulomb repulsion within the electron bunch. Therefore, the rf emittance growth will exhibit a dependence on the rf injection phase and gun tune, while the space charge emittance growth will only depend on the beam charge. The gun tune was very sensitive to cathode position and was difficult to monitor accurately. Therefore, parametric studies of the beam emittance as a function of the gun tune were not performed. However, emittance measurements as a function of beam charge and rf phase were completed. These measurements were performed in collaboration with Dr. Spencer Hartman [39][61] and are reproduced here for completeness.

From PARMELA simulations of the rf photoinjector, the beam normalized emittance is predicted to be $< 10 \pi$ -mm-mrad for beam charge up to 1.0 nC. This is a relatively small emittance and can be difficult to measure if the electron beam propagation is space charge dominated. The beam propagation is said to be space charge dominated if the space charge force acting on the beam exceeds that of the beam emittance. The ratio of space charge force over emittance force is:

$$\frac{F_{sc}}{F_\epsilon} = \frac{2I_0 R^2}{\beta^3 \gamma_A \epsilon_N^2} \quad (36)$$

where I_0 is the beam current, R is the beam radius, I_A is the Alfvén current and ϵ_N is the normalized beam emittance [1]. In the last section, the beam energy measurement was described and the energy of the electron bunch was determined to be 3.5 MeV while peak current ranged from 5 - 300 Amps. Since the beam energy is low and the peak beam current is relatively large, $1.5 < \text{space charge force} / \text{emittance force} < 5$, and therefore, the beam propagation is space charge dominated. In order to extract the beam emittance from a space charge dominated beam, a pepper pot is used to transform the space charge dominated beam into an array of emittance dominated beamlets. The beam expansion of each beamlet is measured and whole beam emittance is determined from an ensemble average over all the beamlets [62]. In addition, since the pepper pot measurement is a single shot measurement, the emittance of each bunch can be measured and correlated with the beam charge and laser injection phase.

The UCLA emittance diagnostic was designed and tested by Hartman [39]. A venetian blind with 8 slits, each 50 μm in width and 1.1 mm apart, was used because the hole sizes required to eliminate space charge in a pepper pot were difficult to manufacture. The portion of the beam which passed through the slits in the venetian blind created diverging beam lines which were observed on a profile monitor, similar to the one described in the following section, located 20 cm downstream of the venetian blind. The widths and relative spacing of the beam lines were measured and used to calculate the beam phase space and emittance [39]. The beam lines produced by the venetian blind were integrated lengthwise to improve signal to noise. Since a venetian blind was used rather than a pepper pot, only the vertical emittance was measured, but because of the

cylindrical symmetry of the rf gun, the horizontal emittance should match the vertical emittance. Using this technique, beam emittances of less than 5π -mm-mrad were measured for a beam charge less than 0.2 nC.

The emittance was first measured as a function of beam charge. Due to limitations in the beam transport at the time, the range of charge was limited to 0.1 - 0.5 nC. However, even over this range, the emittance dependence on beam charge was resolved as seen in Fig. 3.35 [63]. As predicted by the analytic theory of Kim for rf photoinjectors, the emittance dependence on beam charge is linear [47].

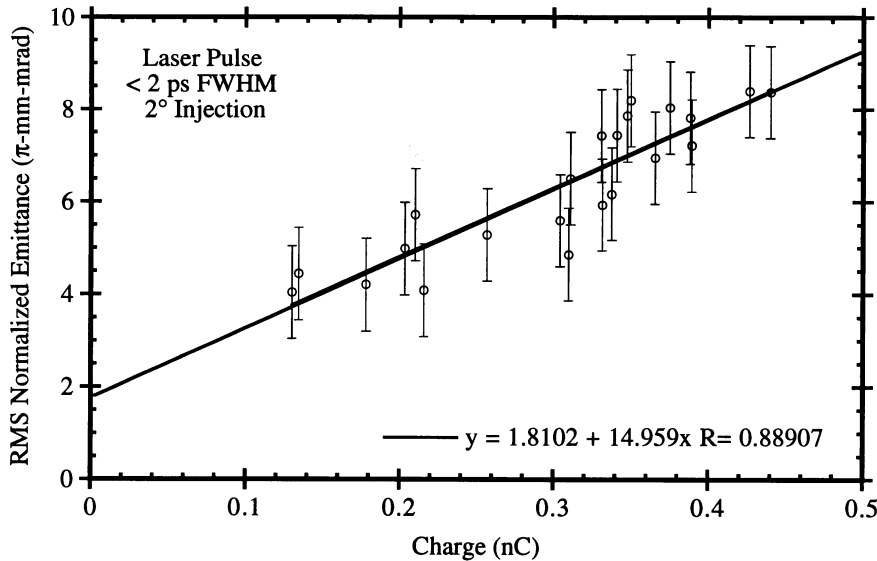


Figure 3.35: Measurement of Emittance as a Function of Beam Charge

Because of the large contribution to beam emittance from space charge, the rf induced emittance could not be measured directly. In order to extrapolate the rf contribution, measurements of emittance vs charge were taken at each laser injection phase. Linear fits to the charge data were performed and the rf contribution was extrapolated as the zero charge limit from the linear fit. Since the quantum efficiency and beam transport change as a function of rf phase, the measurement was limited to injection phases from 50°-100°.

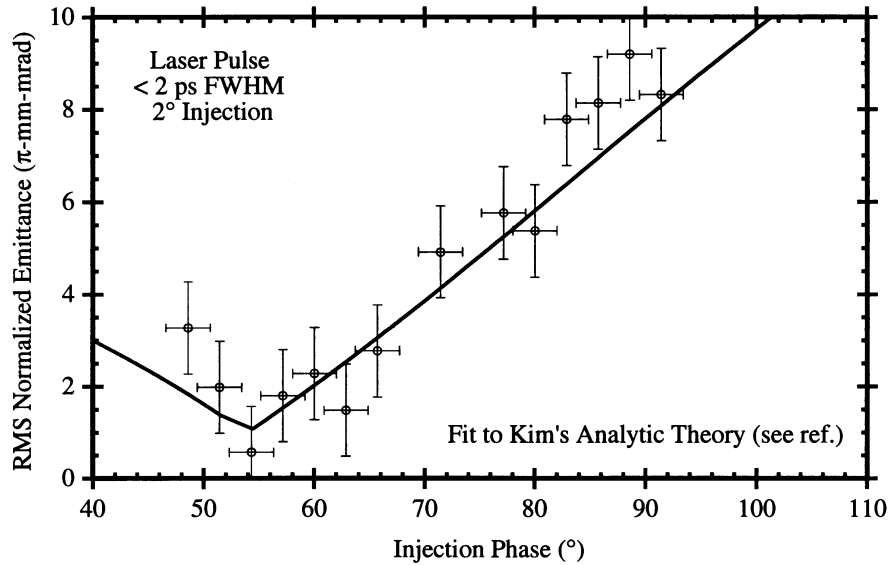


Figure 3.36: Measurement of Emittance as a Function of Laser Injection Phase

The results are plotted in Fig. 3.36 [63]. The minimum emittance occurs at about 50° which agrees well with the analytic theory as described by Hartman [39]. The rf and space charge contributions to the emittance are comparable, however, at the optimal injection phase of 50° , the space charge contribution dominates the emittance.

Since the beam propagation was space charge dominated, the emittance was not a critical parameter in the overdense lens experiment. However, when the beam was focused by the plasma lens, near the focal point, the beam became emittance dominated and the minimum spot size was determined by the beam emittance. Since the plasma lens produces time dependent focusing, the slice emittance determines the minimum spot size rather than the whole beam emittance. The emittance measurements described above were performed with the 12 ps FWHM electron beam bunches rather than the 25 ps FWHM bunches used in the lens experiment. These shorter bunches should better approximate the slice emittance than the longer bunches. Finally, in the overdense plasma lens experiment, the beam charge from the rf gun was typically > 1 nC and the

laser injection phase was typically $40^\circ - 60^\circ$. Although the emittance measurements were only made up to 0.5 nC, since peak current determines the emittance growth rather than total charge, and since the measured electron beam temporal profiles only varied by a factor of 2 with 2 ps and 50 ps laser pulse illumination of the cathode, the space charge emittance measured at 0.5 nC for the short bunch should equal the emittance at 1 nC for the long bunch. Therefore, the beam emittance for the overdense lens experiment is taken to be approximately 8π -mm-mrad. Both PARMELA simulations and the analytic fits presented in Chapter 4 agree with this estimate for the beam emittance.

3.3.6 Profile Measurements

One of the most useful diagnostics is the profile monitor. This diagnostic is used for detecting the beam position and measuring the beam spot size at various locations along the beamline. Steering and focusing of the electron beam are greatly facilitated by the profile monitor. The construction of the profile monitor consists of a phosphor screen mounted perpendicular to the electron beam axis and a mirror placed at 45° from the beam axis to allow viewing of the phosphor by an 8-bit CCD camera mounted perpendicular to the electron beam axis. The phosphor screen is a thin tantalum sheet whose back side has been coated with Sylvania type 2611 phosphor. This phosphor fluoresces in the green part of the visible spectra when an electron strikes it and the fluorescence is easily visible by CCD cameras. The response of the phosphor is linear with the beam charge and therefore the profile monitors can also be used to measure beam charge. However, the light levels seen by the CCD depend on the f stop used, the lens used to collect the light, and the distance of the camera from the phosphor screen. Therefore, the profile monitor must be calibrated against a known charge measurement like the ICT or the Faraday Cup.

Once this is done, the profile monitor can be used to measure beam charge provided the lens, the f stop, and the position of the CCD camera are not changed. The fluorescence persists for several milliseconds and therefore the image viewed by the CCD camera is time integrated over the entire rf pulse duration. Consequently, any beam image will also include contributions from the dark current that must be subtracted in order to resolve the photo-current image and charge.

Typically the profile monitor is used to measure the beam spot size near a waist or to check the position of the beam relative to the beamline center, however, by adjusting the solenoid focal strength, an image of the photo-emission from the cathode can be produced at profile monitor PM0 (see Fig. 3.19). To facilitate the adjustment of the solenoid focal strength so that the cathode is imaged at PM0, a stencil of the letter "S" was placed in the laser beam so that a light image was formed on the cathode. The light image produced a distinct photo-electron image at the cathode which was recreated at PM0 by adjusting the solenoid field. Because most of the dark current is at a lower energy than the photo-current, the dark current was strongly overfocused and the dark current background was negligible. This imaging technique was used to study the emission from the copper photocathode when the quantum efficiency degraded.

Two different copper cathodes were studied using the imaging technique. The first was the commercially polished cathode purchased from Spawr Industries, CATH2. Recall from Section 3.3.2 that CATH2 was polished to $\lambda/4$ at $.6 \mu\text{m}$ flatness and 40/20 scratch and dig. The second was CATH3 which was hand polished at UCLA down to $0.3 \mu\text{m}$ diamond grit size as described in Section 3.3.2. Both cathodes were fabricated from OFHC copper. The photo-current from CATH1 was never carefully imaged to look for uniform emission.

It was mentioned in Section 3.3.2 that the quantum efficiency of CATH2 dropped suddenly after one month of continuous running at high power (> 6 MW). Concurrently, it was noticed that the electron beam had developed severe structure and the solenoid focal strength was set to image the electron emission from the cathode surface on PM0. The image of this emission is depicted in Fig 3.37(a). After this change in cathode

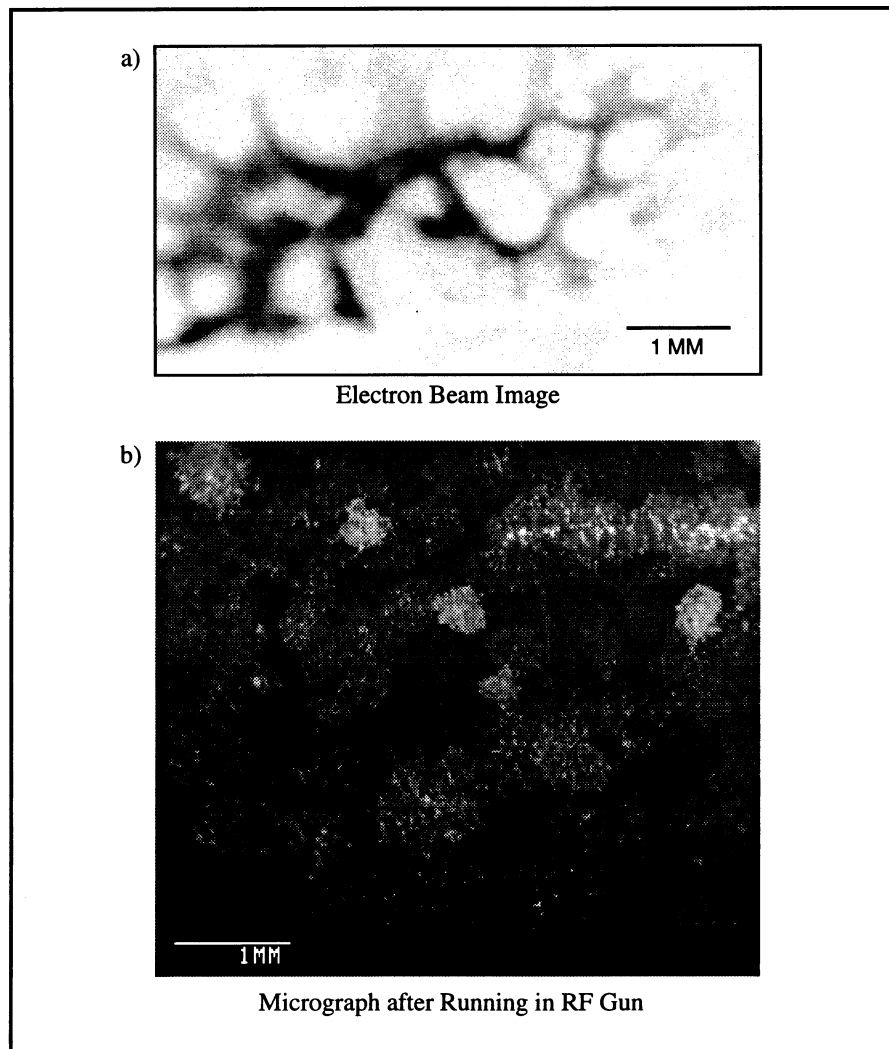


Figure 3.37: Nonuniform Electron Emission: a) Image of electron beam produced from CATH2. b) SEM image of the surface of CATH2

emission, the quantum efficiency was again remeasured. This time the quantum efficiency dropped by a factor of 3.

CATH2 was then removed from the rf gun and the surface was imaged using a Scanning Emission Microscope (SEM). Fig. 3.37(b) depicts surface structure which covers the cathode surface except in the laser damaged area described in Section 3.3.2. The size and shape of the structure seen in the SEM correspond roughly with that of the nonuniform emission shown in Fig. 3.37(a). The light colored areas indicate a fractal growth pattern at the edges. This seems typical of a contamination growth on the cathode surface from residual gasses which is facilitated by the field emitted electrons and back bombardment of ions. CATH2 was further tested in a DC photo-emission test stand where variations in emission greater than factors of 2 were measured across the surface [60]. For the beam image depicted in Fig. 3.37(a), the camera contrast was set to enhance the visibility of the structures. Since this distorts the dynamic range of the camera a quantitative evaluation of emission variation across the cathode could not be made and compared with the DC test stand results. Upon closer examination of CATH2 with the SEM, various types of damage were observed. Electron micrographs showing different types of surface damage produced by laser damage and rf breakdown are shown in Fig. 3.38. The laser damage typically produces larger scale structures formed from molten copper while the rf damage shows a smaller more symmetric structure. The large scale laser damage depicted in Fig. 3.38(a)-(b) were created in an attempt to improve the quantum efficiency as described in Section 3.3.2 after the beam image of Fig. 3.37(a) was recorded. Therefore, the structured emission shown in Fig. 3.37(a) is not produced by laser damage but most likely by the contamination growths described above. The other structures observed on the cathode surface, Fig. 3.38(c)-(d), are much smaller than

could be resolved with the profile monitor imaging system and serve only to indicate the types of damage which can occur to a copper cathode in the large electric fields present in the rf gun.

As described in Section 3.3.2, following the investigation of quantum efficiency and nonuniform emission of CATH2, it was replaced with CATH3, an OFHC copper

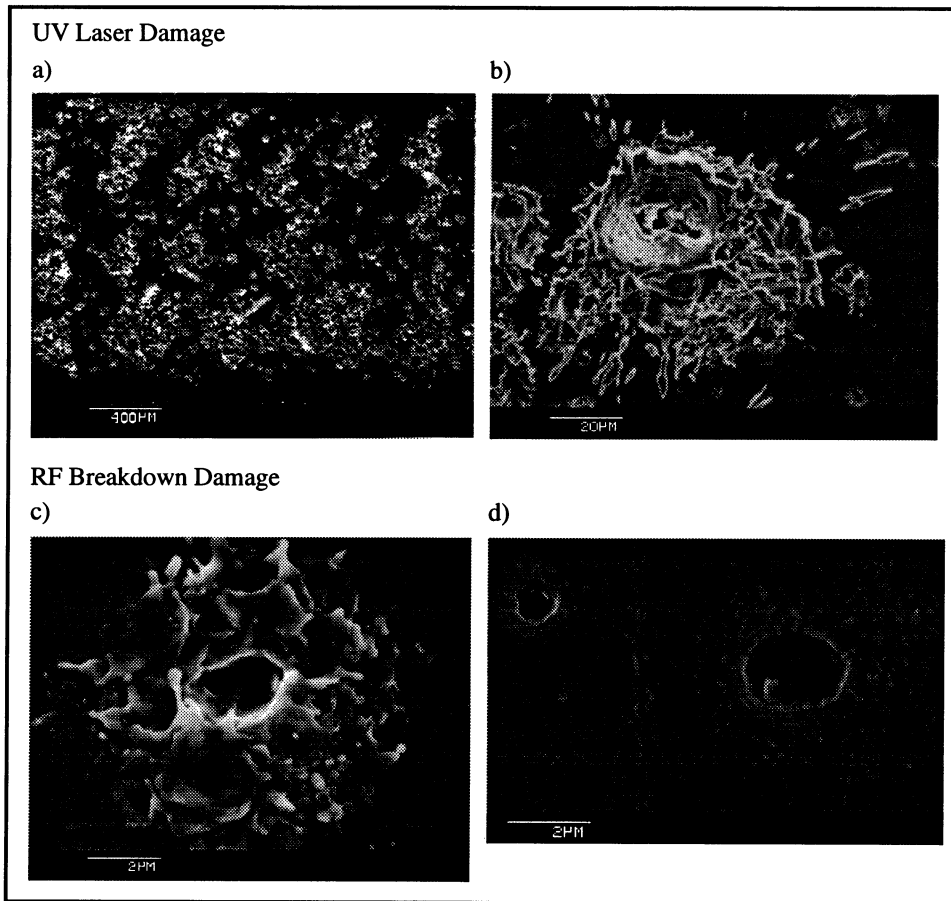


Figure 3.38: Damage on Surface of CATH2: a) Laser damage produced on cathode by focusing the laser to a 300 µm spot at the cathode surface. This damage is characterized by severe melting of the Cu surface. b) Laser induced damage outside of direct laser incidence. This damage is occurred adjacent to the direct laser damaged area. It is characterized by localized severe melting of the copper surface. It also gives the appearance of molten copper drops adhering to the surface. c) Rf induced damage from multiple arcs from high power rf breakdown. d) Single rf breakdown crater.

cathode which was hand polished at UCLA. This cathode was pre-tested in the DC test stand [60] to verify that the quantum efficiency was uniform across the cathode surface prior to installation in the rf gun. The quantum efficiency was measured to be uniform across the cathode to within $\pm 10\%$ [60]. This cathode was then installed in the rf gun and conditioned up to 4 MW of rf power. The quantum efficiency was measured as described in Section 3.3.2 and the cathode emission was imaged on PM0. These images showed a smooth emission profile which matched that of the laser beam. However, after 8 hours of conditioning during which the rf power was increased to 6 MW and the quantum efficiency dropped by a factor of 2, the cathode emission became "spotty" as shown in Fig. 3.37(a). CATH3 was immediately removed from the rf gun and taken to the DC test stand where the quantum efficiency was remeasured. No change in quantum efficiency or evidence of nonuniform emission was observed. An SEM image of the cathode was made which indicated that some structures had formed on the surface which had not been present prior to its installation in the rf gun (see Fig. 3.37(b)), however, these structures had a different character than those observed on CATH2. Although nonuniform emission was produced from CATH3 and a corresponding structure on the cathode surface was observed, neither was as pronounced as the structures produced from and observed on CATH2. This is probably due to the shorter time and lower rf powers achieved in the conditioning of the cathodes.

The profile monitor is a valuable diagnostic for monitoring and characterizing the electron beam. By imaging the cathode emission on PM0, nonuniform emission from the copper cathode was observed and a qualitative correlation between the onset of nonuniform emission and a drop in quantum efficiency due to rf conditioning was discovered. More detailed measurements should be performed in order to quantitatively

understand why and how the cathode surface is modified by the high power rf and how the surface characteristics affect the photo-emission. However, for the overdense plasma lens experiment which will be presented in Chapter 4, the initial spot size was only 2.5 mm FWHM and no evidence of nonuniform emission was observed. Four profile monitors were used to measure the beam size before and after the plasma lens and by fitting these measurements with the theory presented in Chapter 2, the characteristics of the overdense plasma lens are determined.

3.4 Summary

An electron beam, suitable for performing plasma lens experiments was developed and characterized at UCLA. The beam parameters matched the requirements set forth in the introduction to Chapter 3. The beam charge was adjustable up to 7 nC, the bunch length was measured to be 25 ps FWHM in long pulse mode (with ≈ 7 ps rise time and a > 50 ps fall time), the beam energy was 3.5 MeV, and the normalized beam emittance was approximately 8π -mm-mrad. With the use of a single solenoid focusing element, the beam spot size could be adjusted to a 2 mm FWHM spot size at the plasma lens. However, due to limits in the laser energy available during the lens experiment and the difficulty of propagating the space charge dominated beam to the plasma lens, the beam charge at the lens was limited to $< .6$ nC. For this reason, the underdense regime could not be accessed and only the overdense plasma lens experiment was performed.

Chapter 4

Overdense Plasma Lens Experiment

4.1 Introduction

An overdense "passive" plasma lens could produce large enhancements in the luminosity at the final focus of an electron collider. The theory for overdense plasma lenses is well developed and was described in Chapter 2. However, before such lenses can be applied in high energy beam experiments, a full characterization of the lens's properties must be performed. In order to fully characterize an overdense "passive" plasma lens, both time resolved electron beam measurements and time integrated beam envelope measurements must be performed under the same conditions so that they can be compared and reconciled with the theoretical model. Furthermore, the beam must focus outside of the plasma with a significant reduction in spot size (more than a factor of 2) in order to demonstrate the lens as a practical tool for improving beam luminosity. With the electron source and beam diagnostics presented in Chapter 3, a complete overdense plasma lens experiment can be performed.

The plasma and beam parameters required to conduct this experiment can be roughly

estimated from the model presented in Chapter 2. Recall from Section 2.3 that the minimum response time of the plasma is $\approx 1/\omega_p$ due to the inertia of the plasma electrons. In order to resolve the onset of the plasma response with the Cherenkov diagnostic, $1/\omega_p$ must exceed 5 ps. Therefore, a plasma density of $n_p \approx 4 \times 10^{12} \text{ cm}^{-3}$ was chosen so that $1/\omega_p \approx 9 \text{ ps}$. For the plasma lens to operate in the overdense regime, the plasma density must exceed the beam density, $4 \times 10^{12} \text{ cm}^{-3} > n_b$. From the beam measurements at the plasma ($Q \leq 0.6 \text{ nC}$, $\sigma_r \approx 0.1 \text{ cm}$, $\sigma_z \approx 0.3 \text{ cm}$), the beam density can be calculated and compared to the plasma density:

$$n_b = \frac{Q}{(2\pi)^{\frac{3}{2}} e \sigma_r^2 \sigma_z} \leq 8 \times 10^{10} \text{ cm}^{-3} \ll n_p. \quad (37)$$

Using the beam profile monitors described in Section 3.3.6, the beam envelope can be measured at various distances from the plasma lens. To demonstrate a practical lens, the beam focus should occur downstream from the plasma and the beam envelope through the focus should be measured along with the time resolved measurement at the focal point. To ensure that the beam focus occurs outside the plasma, a relatively short plasma length is chosen, $L \approx 5 \text{ cm}$. Given the beam energy from Chapter 3 ($\gamma = 7.5$), the focal length for the overdense plasma lens can be estimated using equation (11):

$$f = 5.6 \times 10^{11} \frac{\gamma}{L[\text{cm}] n_b[\text{cm}^{-3}]} \text{ cm} \geq 10 \text{ cm}. \quad (38)$$

Therefore, the focus occurs downstream from the plasma as would be required in lens applications. With this focal length, significant focusing (up to a factor of 10) could be achieved. Using the beam emittance measurement from Chapter 3, $\epsilon \approx 1 \times 10^{-3} \text{ } \pi\text{-mm-rad}$, the focal spot size after the plasma lens is estimated as:

$$\sigma_f \approx \frac{f\epsilon}{\sigma_r} \approx 0.1 \text{ mm.} \quad (39)$$

where σ_f is the RMS beam radius at the focus and ϵ is the real beam emittance. These rough estimates show that with the above plasma and beam parameters, a practical overdense plasma lens can be demonstrated.

This chapter presents the full characterization of an overdense "passive" plasma lens at UCLA using the electron beam described in Chapter 3. The overdense plasma lens focused the electron beam 21 cm downstream of the plasma and a reduction of greater than a factor of 4 in spot size was observed. Time resolved measurements of the focused electron bunch are presented which reveal the dynamic nature of the overdense plasma lens focusing mechanism. This dynamic focusing is then used to explain the time integrated beam spot size measurements made at various positions downstream of the plasma lens. The electron beam envelope follows a distinct asymmetry as it passes through a focus from a plasma lens. Downstream from the focal point, the beam envelope divergence angle is less than the convergence angle to the focal point. This asymmetry had previously been interpreted as a reduction in the beam emittance due to the plasma lens [27]. However, it is now explained as a manifestation of the dynamic focusing of the overdense plasma lens. The beam measurements are compared to the analytic theory and computer simulations from Chapter 2. In Section 4.2 the electron beamline used for the experiment and its effects on the beam parameters measured in Chapter 3 are described. The plasma source and the plasma density measurements are presented in Section 4.3. The effect of the neutral gas on the electron beam is examined and found to be negligible. Sections 4.4 and 4.5 are summaries of the time resolved and time integrated beam profile measurements respectively. The analysis of these

measurements is presented in Sections 4.6 and 4.7. Section 4.6 covers the wakefield analysis while Section 4.7 describes particle simulations performed for the exact experimental parameters and compares the results with the measurements and the wakefield calculations.

4.2 Electron Beamline

The electron beam used in the overdense lens experiment was described in detail in Chapter 3. The rf photoinjector produced a 3.8 MeV electron beam with a normalized beam emittance of 10π -mm-mrad. For the lens experiment, 50 ps FWHM laser pulses were used to generate the electron bunches in the rf gun. Due to the characteristics of the photoinjector, the electron bunches produced from the rf gun had 25 ps FWHM with ≈ 7 ps risetime and a falltime > 50 ps. During the experiment, the laser energy was limited to 90 μ J because of damaged optics, so the maximum charge extracted from the photoinjector was 1.5 nC. The charge delivered to the plasma lens was further limited to 0.6 nC by the beam transport line between the rf gun and the experiment.

The experimental beamline is depicted in Fig. 4.1. The plasma chamber was positioned 2 m downstream of the photoinjector. The diagnostic chamber, located downstream from the plasma source, provided three vacuum ports at 21, 31, and 44 cm from the plasma source for various beam diagnostics. A single solenoid lens and 4 steering dipoles (not shown) were used to focus and transport the beam through the differential pumping system which isolates the rf gun vacuum from the plasma.

Because of the large rf fields maintained in the rf gun, the vacuum in the gun must be

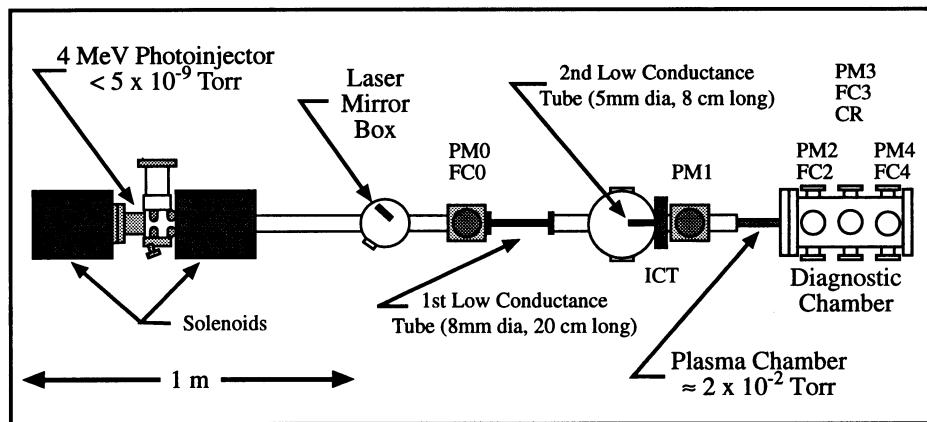


Figure 4.1 Overdense Lens Experimental Beamline

maintained below 5×10^{-8} Torr. The plasma source, however, requires 20 mTorr of neutral gas pressure to achieve the plasma density of $\approx 4 \times 10^{12} \text{ cm}^{-3}$. Although thin foils could be used to isolate the plasma chamber from the gun, because of the low beam energy, the beam scattering in the foil would degrade the beam emittance. In order to preserve the beam emittance, a windowless differential pumping system was designed. Two stages were needed to generate the two orders of magnitude pressure differential required across the 2 m between the rf gun and the plasma. Each pumping stage consisted of a turbo pump followed by a low conductance tube. In the first stage, the low conductance tube was 20 cm long and 8 mm in diameter while in the second stage an 8 cm long and 5 mm diameter tube was used. Although the six orders of magnitude pressure differential was maintained throughout the experiment, because of the small diameter of the low conductance tube in the second stage, the electron beam was scraped as it passed through the tube. More than half of the initial beam charge was lost and therefore the maximum beam charge available at the plasma lens was limited to 0.6 nC. However, the beam emittance was not degraded.

The beamline was equipped with all of the electron beam diagnostics described in Chapter 3. Four profile monitors were used to measure the beam envelope. PM1 was located just downstream of the second low conductance tube and 18 cm upstream of the plasma. The beam profile measured on PM1 established the electron beam characteristics as it entered the plasma lens. Profile monitors PM2-4 were used to evaluate the beam envelope with and without the plasma lens activated. Table 4.1 contains the electron beam spot sizes measured at each profile monitor while the plasma lens was inactivated:

Profile Monitor	PM1	PM2	PM3	PM4
Position	-18 cm	21 cm	31 cm	44 cm
Y FWHM	$2.3 \pm .1$ mm	$3.2 \pm .15$ mm	$3.5 \pm .15$ mm	$4.2 \pm .2$ mm

Table 4.1: Electron Beam Spot Size Measurements Without Plasma Lens

Without the plasma lens, the beam is clearly diverging from PM1 to PM4. Since the profile monitors intercept the electron beam when used, all of the profile monitors were made retractable. Furthermore, the beam envelope can only be reconstructed from many electron bunches since the beam profile can only be measured at one location for each electron bunch. The fluctuations in the beam profile at any monitor position were less than $\pm 5\%$ from shot to shot. The profile monitors could also be used as charge diagnostics once they were calibrated against either the ICT or a Faraday cup.

Besides the profile monitors, the beamline was equipped with 5 charge measuring diagnostics: 1 ICT and 4 Faraday cups, FC1-4. The ICT, described in Section 3.3.2, was placed between the second low conductance tube and PM1. Since the ICT is the only nondestructive charge diagnostic, it was used to measure the total beam charge delivered to the plasma lens for each shot. The Faraday cups, on the other hand, were used primarily in optimizing the rf photoinjector and in verifying the electron beam

transport to the end of the diagnostic chamber. Since Faraday cups intercept the electron beam, like the profile monitors, each Faraday cup was also retractable. FC0 was located upstream of the first low conductance tube. With this diagnostic, the full charge from the photoinjector could be measured and the photoinjector performance could be optimized independent of the beam transport through the differential pumping system. Some dark current was measured at FC0 but for the beam energy of 3.8 MeV, it amounted to less than 0.5 nC. This dark current was completely eliminated through the differential pumping system since its energy was lower and energy spread larger than that of photocurrent. As was mentioned above, the maximum photo-charge measured at FC0 was 1.5 nC of which only .6 nC was transported to the ICT. Faraday cups FC1-3 were used to confirm that the entire beam was transported through the diagnostic chamber with and without the plasma lens activated. These Faraday cups were located along side their respective profile monitors.

Time resolved measurements of the beam profile were performed with a Cherenkov radiator similar to the one described in Section 3.3.3. The electron beam diameter was measured with a spatial resolution of 33 μm and a temporal resolution of 5 ps. Only one Cherenkov radiator was available and it was placed at the same axial position as PM2 and FC2, 31 cm downstream from the plasma, and like PM2 and FC2, was retractable. The electron beam temporal profile was measured with the plasma lens deactivated and matched the results presented in Section 3.3.3, that is, 25 ps FWHM, \approx 7 ps risetime, and $>$ 50 ps falltime. Using this temporal profile and the total charge per bunch measured by the ICT, the beam current within each electron bunch can be calculated. With 0.6 nC of charge, the electron beam current reaches 20 Amps and the beam propagation is space charge dominated.

The beamline was equipped with diagnostics for measuring the beam charge, time-integrated profile and time-resolved profile. Furthermore, it provided six orders of magnitude in pressure isolation between the plasma source and the photoinjector without the use of vacuum windows. Although more than half of the photo-current was lost in the differential pumping system, up 0.6 nC were transported to the plasma source.

4.3 Plasma Source

The plasma source was designed to provide a plasma density of up to $4 \times 10^{12} \text{ cm}^{-3}$. At this density, the plasma response time is $1/\omega_p \approx 9 \text{ ps}$, allowing temporal resolution with the Cherenkov radiator and streak camera described in Section 3.3.3. Also, and the plasma lens clearly operates in the overdense regime, $n_p > 8 \times 10^{10} \text{ cm}^{-3} \approx n_b$. As an additional consideration, a plasma source without an external magnetic field was desired. A magnetic confinement field would produce additional focusing which might compete with the plasma lens and therefore would complicate the analysis.

For these reasons, an inductively coupled rf discharge was chosen as the plasma source. A schematic of the source is depicted in Fig. 4.2. The source consisted of a helical antenna wrapped around the outside of a glass tube which had been filled with Argon gas to a pressure up to 20 mTorr. The helical antenna totaled 12 turns and was 5.5 cm long. The turns were wrapped tightly around the 1.7 cm diameter and 12 cm long glass tube. The rf source used to drive the antenna consisted of a tunable oscillator, 10-20 MHz, which was amplified up to 1 kW of rf power. The oscillator was coupled to the antenna via a capacitive tuning circuit which was used to match the antenna impedance to

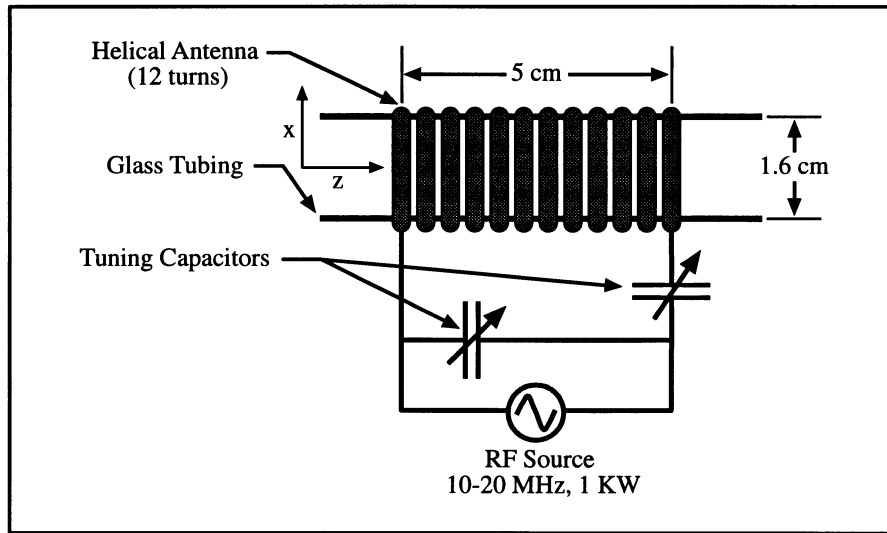


Figure 4.2: Schematic of the Plasma Source

the oscillator. The tuning circuit and the oscillator frequency were adjusted for maximum plasma density. Under optimal tuning conditions, 75% of the rf was absorbed by the plasma. The plasma density was adjustable from $5 \times 10^{11} \text{ cm}^{-3}$ to $5 \times 10^{12} \text{ cm}^{-3}$ by changing the gas pressure and the rf power. Argon was chosen as an inexpensive fill gas because of its relatively low ionization threshold (16 eV). During the experiment, the discharge was pulsed at 5 Hz synchronized with the photoinjector with a 2.5% duty cycle, by pulsing the rf amplifier.

The plasma density was measured with three different diagnostics: a Langmuir probe, a microwave interferometer, and a CCD camera observing an Ar+ emission line. The Langmuir probe was the primary density diagnostic. The probe had a cylindrical tip 3.2 mm long and 760 μm in diameter. It was calibrated by comparing the Langmuir probe ion saturation current with the density measured by the microwave interferometer for various plasma densities. The microwave source was a 62.5 GHz Gunn diode which can be used to probe densities up to $5 \times 10^{13} \text{ cm}^{-3}$ before cutoff. In calibrating the Langmuir

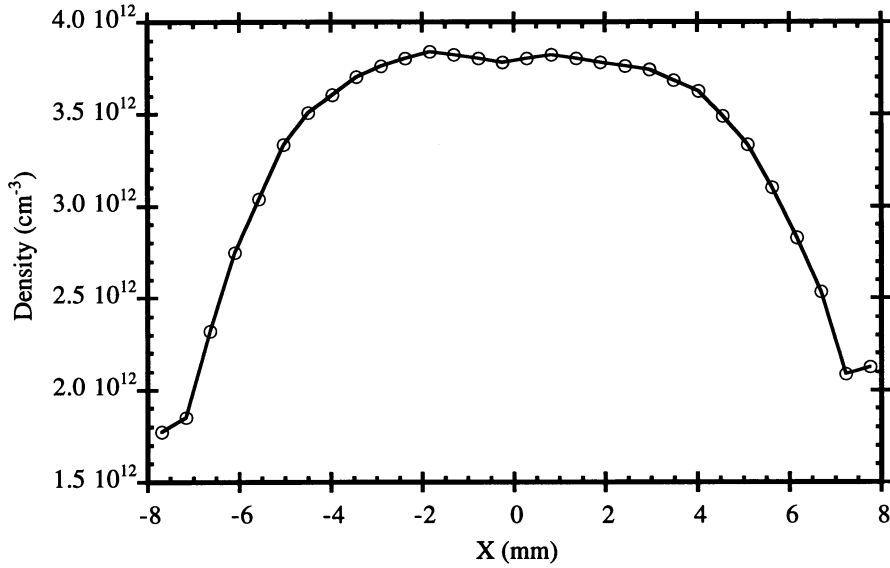


Figure 4.3: Radial Plasma Density Profile

probe, the plasma temperature can be estimated. Given the probe area (measured to be $A = 8.43 \times 10^{-2} \text{ cm}^2$), the ion saturation current, I_{sat} , and the plasma density, n_0 , measured by the microwave interferometer, the plasma temperature is approximately:

$$T_e \approx M_i \left(\frac{2 I_{sat}}{e A n_0} \right)^2 \approx 4 \text{ eV} \quad (40)$$

where M_{Ar} is the Argon ion mass and e is the electron charge [64]. The calibrated Langmuir probe was then used to measure the plasma profile. The radial density profile measured 5 mm axially from the antenna edge is plotted in Fig. 4.3. Over the central 8 mm, the profile is flat to better than 5% but the density begins to fall off 4 mm from the tube walls. This same radial profile was measured at various axial positions. The axial density profile was more difficult to measure. As the Langmuir probe penetrated the plasma under the helical antenna, the discharge was perturbed. Therefore, the Langmuir

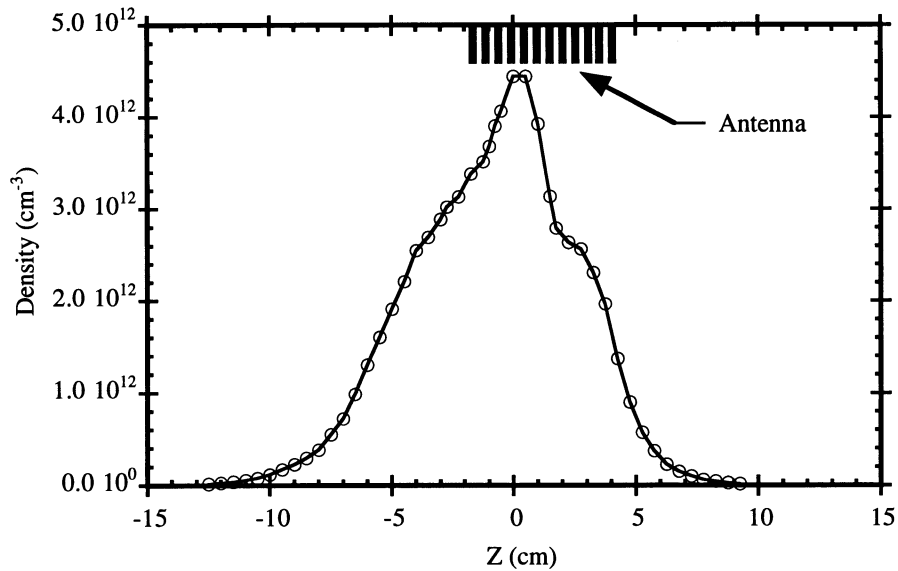


Figure 4.4: Longitudinal Plasma Density Profile

probe could only be used to measure the plasma density up to the edge of the antenna. In order to measure the density under the antenna a spectroscopic density diagnostic was needed. An excited Ar⁺ ion has an emission line at 480 nm. The Ar⁺ is excited by collisions with electrons so the intensity of the emission is proportional to the density of electrons times the density of the Ar⁺ ions. In the plasma, the density of electrons and ions is nearly equal and therefore the intensity of the 480 nm light is proportional to the square of the plasma density. By imaging the light to a CCD camera and filtering all but the 480 nm Ar⁺ line, the entire longitudinal density profile was measured in a single shot. This measurement was calibrated to the Langmuir probe in overlapping regions outside the antenna where the probe did not perturb the plasma. Using this calibration, the density under the antenna was measured with the CCD camera. The axial profile measurement is plotted in Fig. 4.4. The profile is roughly bell shaped with a FWHM of ≈ 7.5 cm. All axial beamline distances were referenced to the peak in the axial plasma density profile. The asymmetry in the profile is caused by a pressure gradient of 20

mTorr over 15 cm across the glass tube. The gas feed was located upstream of the plasma and, therefore, the density peaked 2 cm upstream of the antenna center.

The density was also measured as a function of time over the rf pulse. A 100 μ s turn on time was measured after which the plasma density stabilized. A density ripple of < 10% was measured over the 5 ms pulse. This ripple was reproducible so that the density fluctuations were < 5% from shot-to-shot. The timing between the rf photoinjector and the plasma source was synchronized so that the electron beam passed through the plasma 4 ms into the rf pulse. Since the Langmuir probe could not be installed during the experiment, a photodiode which monitored the 480 nm Ar+ emission line was used as a shot-to-shot density monitor. The photodiode monitor was calibrated with the Langmuir probe before its removal. With this diagnostic the capacitive tuning and frequency matching were performed to optimize the rf power coupling to the plasma.

Given the plasma density of $4 \times 10^{12} \text{ cm}^{-3}$ and the plasma temperature of $\approx 4 \text{ eV}$, the fundamental plasma parameters can be calculated and effects of electron-ion, electron-electron, and electron-neutral collisions examined. The plasma frequency, ν_p , is equal to 18 GHz while the electron-ion collision frequency (ν_{ei}), the electron-electron collision frequency (ν_{ee})[64], and the electron-neutral collision frequency (ν_{en})[65] are 28 MHz, 71 MHz, and 220 MHz respectively. Since $\nu_{ei} < \nu_{ee} < \nu_{en} < \nu_p$, the plasma is collisionless. Therefore, the plasma return currents were not affected by collisions and the wakefield theory presented in Section 2.3 applies. Furthermore, the ionization frequency (ν_{ion}) for the electron beam to ionize the Argon gas is calculated to be 87 MHz [66]. When compared with the electron beam length ($\tau_b < 100 \text{ ps}$, $1/\tau_b > 10 \text{ GHz}$), the beam ionization of the Argon is negligible for the time scales of the experiment as is the scattering of the electron beam with the Argon gas. This was tested experimentally. The

plasma chamber was filled to 30 mTorr of Argon without striking the plasma discharge and the electron beam was propagated through it. Measurements of the beam profile in the diagnostic chamber with and without the Argon gas agreed to within the experimental errors.

An rf discharge plasma source was built and characterized for the overdense plasma lens experiment. The plasma density of $4 \times 10^{12} \text{ cm}^{-3}$ resulted in a plasma response time ≈ 9 ps. By propagating the relativistic electron beam from the rf photoinjector through this plasma, significant beam focusing was observed and the dynamic nature of the plasma lens focusing mechanism was investigated.

4.4 Time Integrated Measurements

The first measurements of the overdense plasma lens focusing were time integrated profile measurements made with the phosphor screen profile monitors described in Section 3.3.6. In addition to the many 8-bit CCD cameras available for capturing the beam profile, one cooled, 12-bit CCD camera, Star1, was available. With this camera a dynamic range of $> 1000:1$ was achieved whereas the 8-bit CCDs were limited to $< 200:1$. This allowed the beam halo to be observed without saturating the focused core of the electron beam.

The time integrated measurements were made at 4 positions along the beamline. The results of these measurements are presented in Table 4.2 which compares the unfocused spot size measurements described in Section 4.2 with the plasma focused beam spot sizes:

Profile Monitor	PM1	PM2	PM3	PM4
Position	-18 cm	21 cm	31 cm	44 cm
Plasma Off	2.3 ± .1 mm	3.2 ± .15 mm	3.5 ± .15 mm	4.2 ± .2 mm
Plasma On	2.3 ± .1 mm	.55 ± .02 mm	1.0 ± .04 mm	1.1 ± .04 mm

Table 4.2: Electron Beam Spot Size Measurements With and Without the Plasma Lens

Focusing of the electron beam was observed on all three profile monitors downstream of the plasma lens.

The beam spot size was also measured as a function of beam charge and plasma density. As expected from the simple theory of Section 2.2, for the overdense lens, the focusing strength depends on the electron beam density. With the plasma density set to $4 \times 10^{12} \text{ cm}^{-3}$, the spot size was measured for various amounts of beam charge. For low beam charge, $< 0.1 \text{ nC}$, no plasma lens focusing was observed. However, as the beam charge was increased from 0.1 nC to 0.25 nC , the spot size on PM2 decreased from 2.3 mm to 0.5 mm . As the beam charge was further increased from 0.25 nC to 0.5 nC , the beam spot size increased slightly to 0.55 mm . The initial decrease in spot size is directly related to the focusing strength of the lens, which increases as the beam density increases. Therefore, as the charge increases, the focal length decreases until at $\approx 0.25 \text{ nC}$ the lens focal length equals 21 cm and the beam is strongly focused on profile monitor PM2. However, if the beam spot size only depended on the focal strength, then, as the charge was further increased up to 0.5 nC and the focal length continued to shorten, the beam spot size measured at PM2 should increase significantly due to the overfocusing of the electron beam. Instead, at the 0.25 nC charge level, the dynamic effects of the plasma lens begin to dominate and the time resolved measurements are needed to explain the saturation of beam spot size as a function of beam charge.

Measurements of spot size at PM2 also indicated a dependence on plasma density. With a fixed beam charge of 0.5 nC, the plasma density was adjusted while the beam spot size was measured. For densities $> 1 \times 10^{12} \text{ cm}^{-3}$, the spot size was constant at 0.55 mm. However, for densities $< 1 \times 10^{12} \text{ cm}^{-3}$, the spot size increased by a factor of 2 or more. Unfortunately, the plasma density was difficult to control at densities $< 1 \times 10^{12} \text{ cm}^{-3}$ and only a qualitative observation of the plasma density dependence could be made. Since the plasma density remained larger than the beam density, the plasma lens operated in the overdense regime for all the measurements. As was indicated above, for the overdense plasma lens, the focusing strength is determined by the beam density and not the plasma density. Therefore, only a weak dependence on plasma density might be expected. However, the lens response time depends entirely on the plasma density, $\tau \approx 1 / \omega_p$. Therefore, as the plasma density is lowered, the plasma cannot respond fast enough to focus the electron beam and the beam propagates through the plasma almost unaffected. On the other hand, for plasma densities $> 1 \times 10^{12} \text{ cm}^{-3}$, the plasma response is fast enough that the focusing dynamics become determined by the electron beam.

Of the three positions downstream of the plasma lens, the smallest spot size was recorded on the first one, PM2, located 21 cm from the plasma density peak. The Star1 camera was used to capture the beam profile with and without the plasma lens at PM2. These images are displayed in Fig. 4.5. Because of the large dynamic range of the Star1 camera, even though the camera aperture setting remained the same in both pictures, the focused beam image was not saturated. Since the phosphor response is linear with the beam charge, the summation of the counts in each picture is proportional to the beam charge. The total counts in both images are the same to within 3%. From the ICT charge

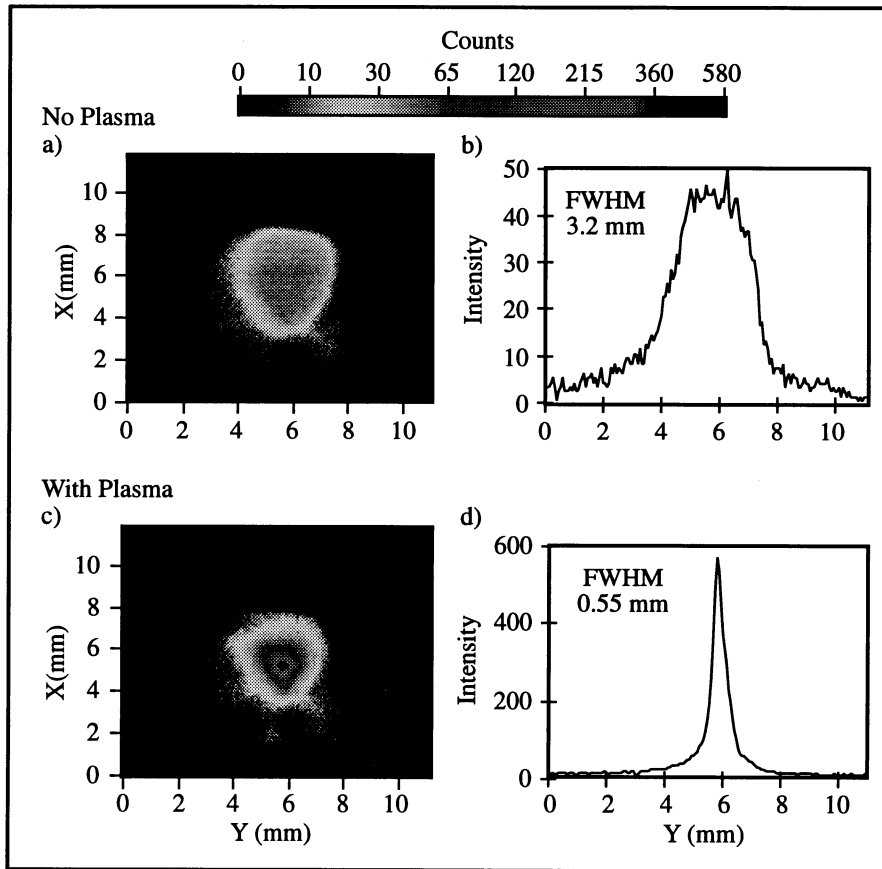


Figure 4.5: Time Integrated Spot Size Measurements at PM2, 21 cm Downstream of the Plasma Lens measurement, the beam charge was determined to be 0.45 nC for each shot. FC2 confirmed the 100% transmission of the beam charge both with and without the plasma lens.

From Fig. 4.5, two salient features should be noted: the strong focusing produced by the plasma lens and the existence of the beam halo in both the focused and unfocused beam images. Along side the beam images are vertical lineouts through the center of the electron beam. These lineouts show the significant focusing produced by the overdense plasma lens. The unfocused beam spot size of 3.2 mm FWHM was reduced to 0.55 mm FWHM by the plasma lens. Relative to the spot size at the entrance to the plasma lens

measured at PM1 of 2.3 mm FWHM, a factor of 4.2 reduction in spot size was demonstrated. Due to this focusing, the peak intensity increased by a factor of 12, from 45 counts in the unfocused image to 550 counts in the focused image. Given that the beam charge was conserved (as was confirmed by the image count summation) and assuming the beam profile remained unchanged by the focusing, an increase in the peak intensity of a factor of 34 would be expected for the measured spot size reduction. However, as is clear in both the focused beam image in Fig. 4.5 and in its respective lineout, the focused beam retained a beam halo of roughly the same dimensions as the unfocused beam. This halo, which accounts for the shortfall in the measured peak intensity, is due in part to the dynamic focusing of the plasma lens and in part to spherical aberrations of the overdense plasma lens. From the simple lens theory, it is expected that the head of the pulse will not be affected by the plasma because of the finite response time of the plasma. Therefore, the first $1/\omega_p \approx 9$ ps of the electron beam will remain unfocused and contribute to the beam halo. This is verified by the time resolved measurements presented in the next section.

4.5 Time Resolved Measurements

The time integrated measurements cannot be correctly explained without an understanding of the dynamic nature of the overdense plasma lens. Time resolved measurements were performed with a slightly thicker Cherenkov radiator than the one described in Section 3.3.3. A 500 μm thick fused silica etalon was installed in place of the 250 μm etalon used earlier. This thicker etalon produced twice the Cherenkov

radiation per beam electron than did the thinner etalon, without sacrificing time resolution. The 250 μm etalon had a 1 ps time response but the overall diagnostic resolution was limited to 5 ps due to the streak camera's temporal resolution. Therefore, by using the 500 μm etalon, the diagnostic's sensitivity was increased, but although the Cherenkov radiator's temporal response was increased to 2 ps, the overall diagnostic's temporal resolution was still limited by the streak camera to 5 ps. Spatially, the resolution was also limited by the streak camera to 33 μm . The Cherenkov radiator was placed on a retractable mount 31 cm downstream from the plasma.

The raw streak data for the plasma focused electron beam is shown in Fig. 4.6(a). The dynamic effect of the plasma lens on the electron beam profile is immediately apparent. As was expected, the head of the electron beam did not focus. It maintained a 2.7 mm FWHM spot size after passing through the plasma lens. The best focus at this location occurs almost 20 ps from the head of the bunch. At this focus, the beam spot size is reduced to 0.57 mm FWHM. Quantitative measurements extracted from the streak image are plotted in Fig. 4.6(b). The points on the graph are calculated by slicing the streak into 15, 5 ps wide strips, based on the resolution of the streak camera. The 5 ps strips overlap to provide 5 ps resolution over 40 ps. In measuring the spot size FWHM, each 5 ps strip is integrated along the temporal axis to provide better statistics. The FWHM of the resulting spatial profile is plotted in Fig. 4.6(b). The peak intensity values of these profiles are also plotted as a function of time in Fig. 4.6(b). The peak intensity value rises from 100 to 2300 counts as the beam spot size is reduced from the head of the beam to the best focus. This factor of 23 rise surpasses the linear dynamic range of the streak camera which is approximately 20:1. Saturation effects in the streak camera for counts above 200 in the streak image of Fig. 4.6(a), result in approximately a 20% reduction in

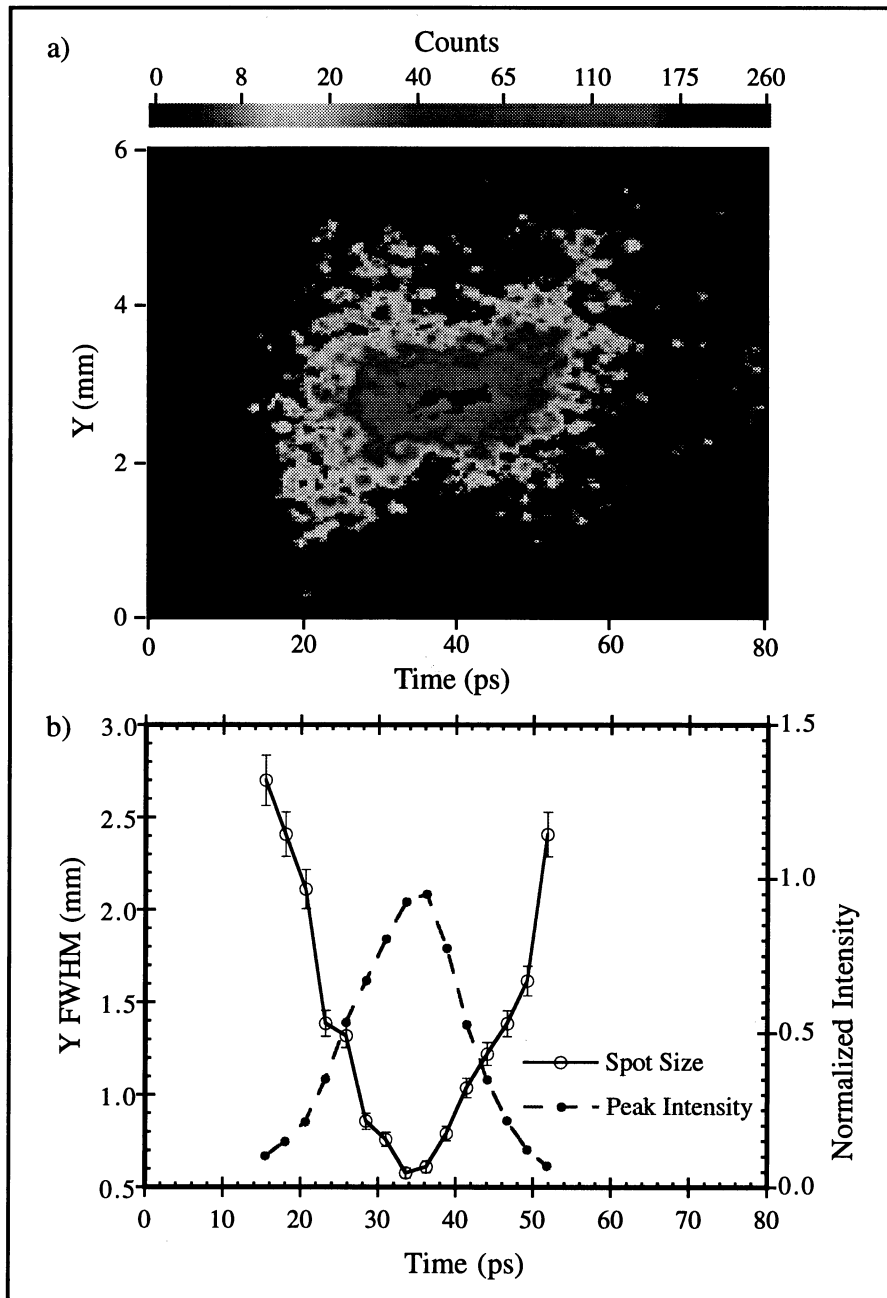


Figure 4.6: Time Resolved Measurement of the Plasma Focused Electron Beam a) Streak image of the electron beam at CR located 31 cm downstream of the plasma. b) Measurement of spot size and peak intensity from the streak image.

the peak intensity measurement of Fig. 4.6(b). Nevertheless, the peak intensity occurred at the time when the beam was focused tightest as is expected.

Another important feature of the dynamic focusing is that the beam spot size increases in the tail of the electron beam. This can be explained qualitatively by two effects. The most obvious reason for the larger spot size in the tail of the beam is that the focusing force decreases due to the wakefield response of the plasma. As was described in Chapter 3, the wakefield will provide a varying degree of focusing as a function of time. If the peak in the wakefield focusing occurred at the time corresponding to the minimum spot size, then it is expected that at later times the focusing force decreases and therefore results in larger spot sizes. There is another related effect, however, that can result in the same dynamic focusing. That is, if the peak in the focusing force occurs at a later time than that of the minimum spot size, then the tail of the electron beam is overfocused at the axial position where the measurement was made, resulting in a larger spot size at the tail of the electron beam. This emphasizes the fact that each temporal slice of the electron beam might have a different focal length due to the time dependent focusing force. In order to determine which effect was occurring, a simple test was performed. The dynamic focusing was observed as a function of beam charge. As the beam charge was lowered, the minimum spot size occurred at later times. If the effect had been caused by the weaker focusing force due to the temporal wakefield response, then the minimum spot size should have increased in size because of the weaker focusing. However, it also should have occurred at the same relative time, since the time response is determined by the plasma density and the electron beam profile, which were unchanged. Instead, the minimum spot size occurred at a later time because the focal length of that later time slice matched the axial position of the Cherenkov radiator where the measurement was made.

Whereas the focal length of earlier time slice had increased and the spot size of that slice was still relatively large as it approached a focus beyond the Cherenkov radiator. This can also be confirmed by wakefield calculations. It will be shown in Section 4.6 that the peak in the temporal focusing force occurred at 35 ps from the beam head.

4.6 Wakefield Analysis

In order to compare the analytic wakefield theory presented in Chapter 2 with the measurements described above and to quantify the dynamic focusing described in the previous section, numerical calculations are performed based on the experimental parameters. Recall from Section 2.3 that the overdense plasma lens focusing force can be expressed as a function of the spatial and temporal profiles of the electron beam:

$$\begin{aligned}
 W_{\perp}(r, \tau) &\equiv E_r(r, \tau) - \beta B_{\theta}(r, \tau) \\
 &= \frac{\partial G(r)}{\partial r} \left[\omega_p \int_0^{\tau} d\tau' T(\tau') \sin[\omega_p(\tau - \tau')] - \frac{T(\tau)}{\gamma^2} \right]. \quad (41)
 \end{aligned}$$

where $G(r)$ is a function of the electron beam's spatial profile as defined in equation (20) and $T(r)$ is the beam's normalized temporal profile. The radial dependence can be calculated using the measured beam profile. However, since the measured profiles are roughly gaussian, for simplicity, a gaussian profile was assumed with the appropriate sigma to match the measured FWHM. The radial integral of equation (20) is performed using the gaussian profile to arrive at the radial dependence of the focusing force. Likewise, using the measured temporal profile of the unfocused beam from Fig. 3.32,

the temporal part of the focusing force (in square brackets above) is calculated and plotted in Fig. 4.7 for the measured plasma density peak of $4 \times 10^{12} \text{ cm}^{-3}$. The peak in the

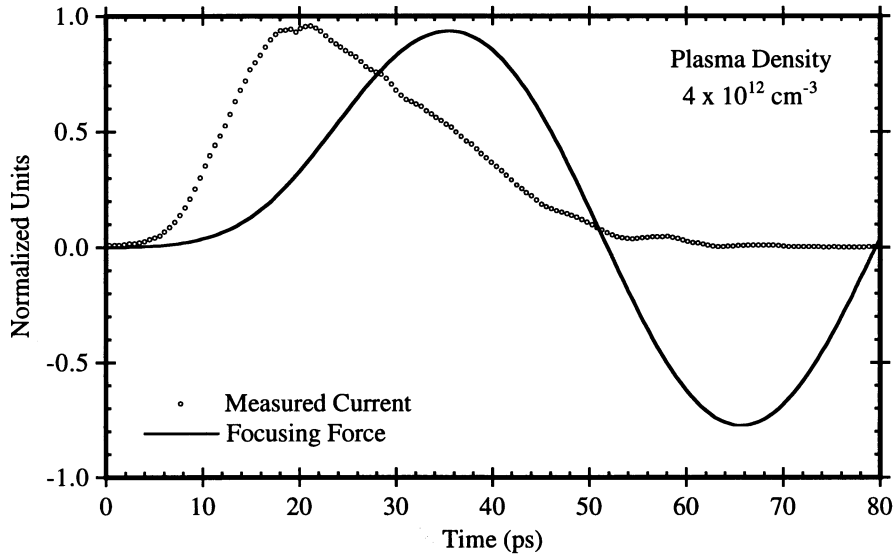


Figure 4.7: Calculated Temporal Wakefield Response. The calculation was performed using the measured temporal profile of the electron beam and the measured plasma density.

focusing force occurs at 35 ps from the head of the beam. Due to the sharp risetime (≈ 7 ps) of the electron bunch, a sizable wakefield is excited in the plasma. Using equation (19) the longitudinal electric field is calculated to be $\approx 1 \text{ MeV/m}$. Therefore, it is expected that the electrostatic radial electric field contributes significantly to the focusing force. The wakefield focusing force of equation (41) can be separated into contributions from the radial electric field and azimuthal magnetic field as depicted in Fig. 4.8. The azimuthal magnetic field focusing force follows the electron beam profile since it is generated directly by the electron beam. On the other hand the radial electric field follows the response of the plasma since it is a manifestation of the electrostatic wakefield induced in the plasma by the sharp risetime of the electron beam. At the peak in the net focusing force, the azimuthal magnetic field provides 40% of the focusing whereas the radial

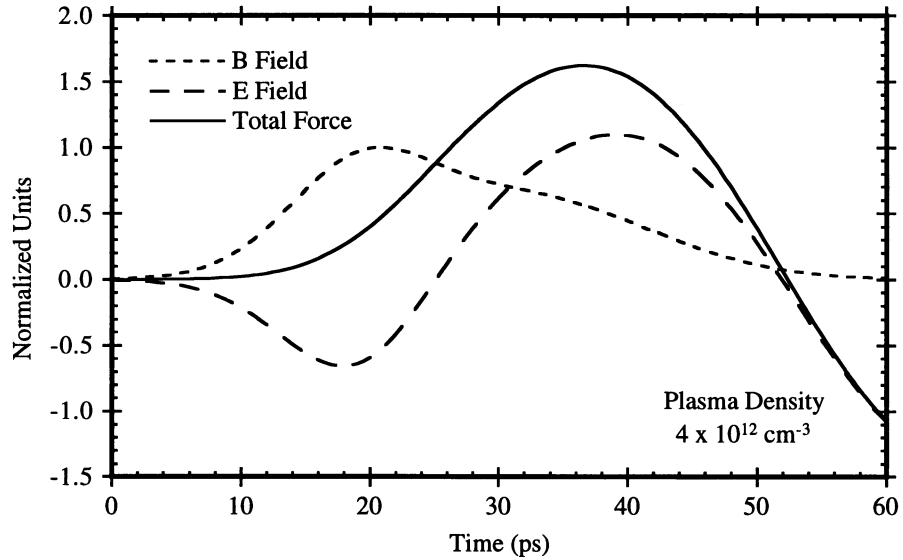


Figure 4.8: Electric and Magnetic Field Contributions to the Radial Wakefield

electric field contributes the remaining 60%. It is important to note that the amplitude and time response of the focusing force also depends on the plasma density as described in Chapter 2. As the electron beam propagates through the plasma lens, it will experience varying amounts of focusing according to the axial plasma profile. The dependence of the net focusing force on plasma density can also be calculated using equation (41).

Given the focusing force from the wakefield theory as a function of time, space, and plasma density, the dynamic focusing of the overdense plasma lens can be numerically calculated. First the temporal profile of the unfocused electron beam is divided into 11 evenly spaced slices at 5 ps intervals. Each slice is assigned an instantaneous beam current based on the measured temporal profile and is labeled by its time (τ) from the head of the beam. Likewise, the plasma axial profile is divided into 20 sections, each 1 cm thick. A constant density value is assigned to each section equal to the average measured density of each 1 cm slice. The wakefield focusing force can now be calculated as a function of axial distance (z) through the plasma for each beam slice. The beam

envelope equation for each slice, including space charge and the focusing term from the overdense plasma lens, can be expressed as:

$$\frac{d^2 R_\tau(z)}{dz^2} - \frac{\epsilon^2}{R_\tau^3(z)} - \frac{K}{R_\tau(z)} + \frac{W_\perp(z, r_0, \tau)}{E \beta^2} = 0 \quad (42)$$

where $R_\tau(z)$ is the beam sigma of the slice τ , ϵ is the beam emittance, E is the beam energy, and

$$K = 2 r_e I_0 / e \beta^3 \gamma^3 c \quad (43)$$

is the generalized perveance of the beam where I_0 is the beam current of the slice and r_e is the classical electron radius [1]. In using the beam envelope equation, it is assumed that the radial beam profile remains gaussian. The wakefield, $W_\perp(z, r_0, \tau)$, is evaluated from equation (41) for each plasma slice using the beam radius, r_0 , at the beginning of the slice and the plasma density value assigned to the plasma slice. Note that using a constant radius for each plasma slice introduces a negligible error since the beam radius changes by less than 1% over the 1 cm distance of each plasma slice. Therefore, the beam envelope can be calculated by numerically integrating the envelope equation from one plasma section to the next, each time using the values of $R_\tau(z)$ and $R'_\tau(z)$ from the previous section as the initial conditions. This numerical integration is repeated for each beam slice to get the overall dynamic focusing of the entire electron beam. For the drift section before and after the plasma lens, the wakefield term is dropped and equation (42) becomes the standard envelope equation including space charge. However, before the beam envelope can be evaluated numerically, the initial conditions must be known.

The initial beam conditions are defined at PM1 since it is the final diagnostic at which beam measurements could be made before the plasma lens. Therefore, the initial

conditions are derived from the beam measurements of Chapter 3 and the unfocused measurements of Sections 4.4 and 4.5. As described in Chapter 3, the beam energy and real emittance were measured to be 3.5 MeV and 1π -mm-mrad respectively while the spot size measurement at PM1 was 2.3 mm FWHM, defining an initial beam radius of 1.0 mm. The unfocused streak measurement described in Section 4.5 did not indicate any significant temporal dependence of the beam size, and therefore, the initial beam radius of 1.0 mm is used for all beam slices. To derive the initial beam divergence, the time-integrated profiles measured for the unfocused beam at PM1-4 were used. Using an average beam current, the envelope equation was solved for a vacuum drift to the end of the diagnostic chamber as a function of the initial beam divergence. The best fit with the measured data required an initial beam divergence of 1.2 mrad. The vacuum beam envelope and the measured data from Section 3.4 are graphed in Fig. 4.9. It was assumed that the initial beam divergence was constant over the entire beam, and

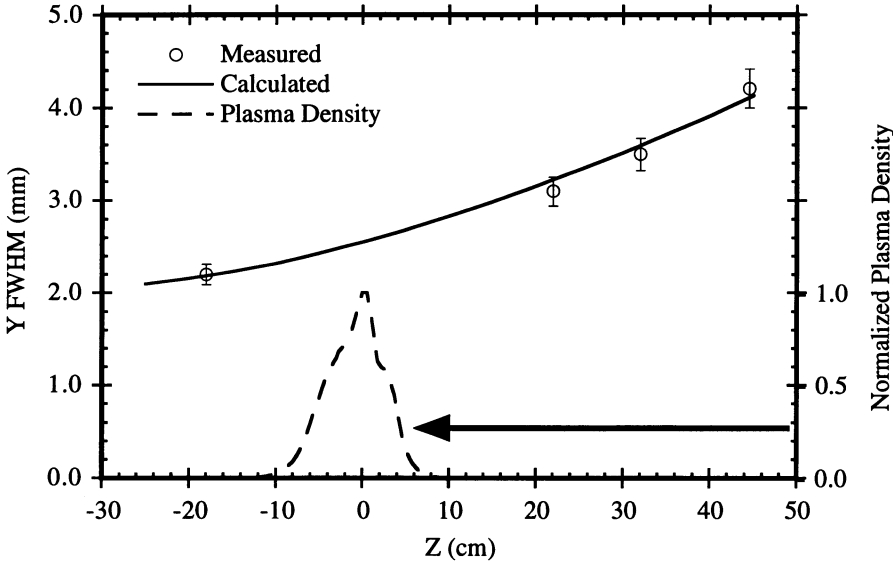


Figure 4.9: Measured Beam Envelope with Plasma Off. The calculated curve is a fit to the measured data using the beam envelope equation with space charge.

therefore, 1.2 mrad was used as the initial condition for each beam slice.

With these initial beam conditions equation (42) can be numerically integrated for each electron beam slice. Since the initial conditions were defined at PM1, the initial section in the envelope equation is a vacuum drift space up to the first plasma section which occurs at -10 cm from the peak in the axial plasma profile. After the 20 plasma sections, the beam envelope integration is continued for a vacuum drift section to the Cherenkov radiator position, 31 cm downstream of the plasma peak. The calculation is repeated for each plasma slice. The results of these calculations are plotted with the time-resolved measurements for the plasma focused electron beam in Fig. 4.10. The

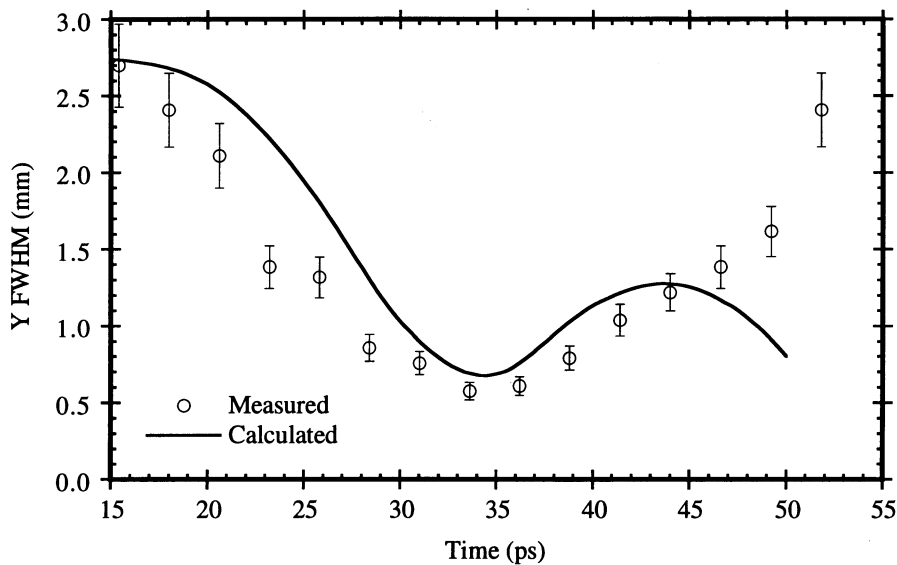


Figure 4.10: Comparison of the Wakefield Calculation of Dynamic Focusing with the Measurement.

calculations show very good agreement with the measurements considering the simplicity of the model. Both the minimum spot size and the time at which it occurs are correctly predicted by the wakefield calculations.

By summing over all the beam slices, the wakefield calculations can also be compared with the time-integrated measurements of the plasma focused beam. Remember that a

gaussian profile was assumed as one of the initial conditions, and that one of the caveats of the beam envelope equation is that the radial profile is preserved. Therefore, a gaussian profile is calculated for each beam slice according to its beam envelope radius. These gaussian profiles are assigned weighted amplitudes according to each beam slice's initial current and inversely proportional to the slices radius squared so that the total charge of each slice is conserved. The Gaussians are then summed to produce a time integrated beam profile. To compare this calculation with the measured beam profile from Section 6.4, the calculated beam profile at PM2 is plotted with the measured profile in Fig. 4.11. Excellent agreement is achieved between the calculation and the measurement. In particular, the wings in the profile are correctly predicted.

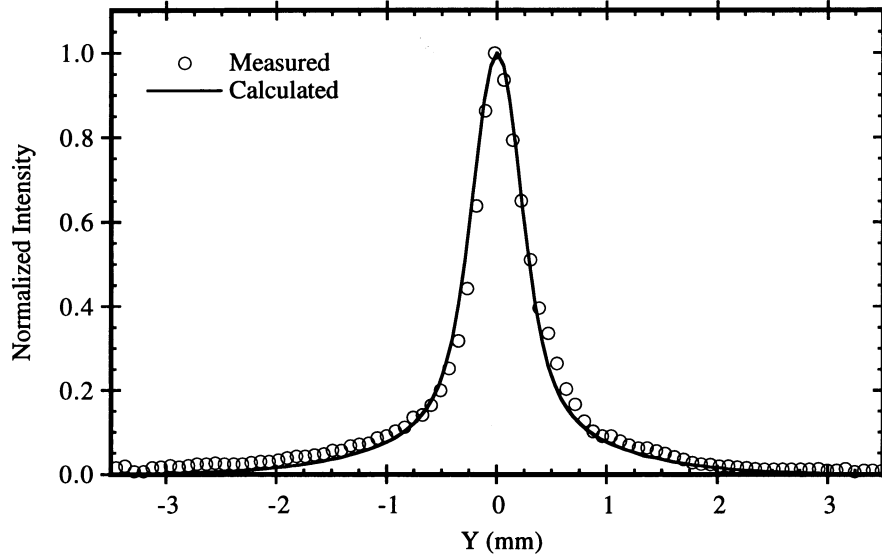


Figure 4.11: Comparison of the Wakefield Calculated Beam Profile and the Measurement at PM2.

Similar calculations are performed for various distances from the initial position at PM1 to PM4 located 44 cm downstream of the plasma. The resulting FWHM of the time-integrated beam envelope is shown in Fig. 4.12 along with the measured values from Section 4.4. The calculated envelope agrees very well with the measured values

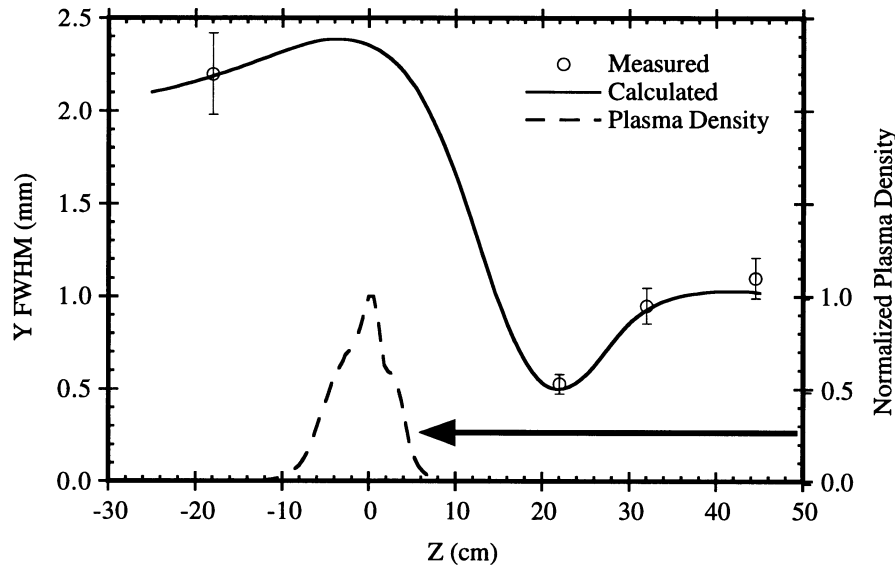


Figure 4.12: Measured and Calculated Beam Envelope with Plasma On

and correctly reproduces the asymmetric focus observed in the measurement. As explained by these calculations, the asymmetric focus is a manifestation of the dynamic focusing produced by the overdense plasma lens. The beam envelope calculated for each beam slice follows a symmetric path about its focal point as expected from standard beam propagation dynamics. However, since each of the beam slices experiences a different focusing force while propagating through the plasma lens, the focal length of each beam slice is different. When calculating the time-integrated profile, the beam slices which are focused at the axial position of interest contribute significantly to the peak amplitude of the time-integrated profile while the beam slices which are not focused produce low amplitude wings in the profile. Because the FWHM measurement of the beam profile is very sensitive to the peak amplitude of the profile and insensitive to the wings of the profile, the beam slice which is focused at the axial position of interest dominates the FWHM measurement. Therefore, in reference to Fig. 4.12, the time-integrated beam envelope between the plasma lens and the minimum focal spot follows the envelope of

the beam slice which is focused strongest by the lens since this beam slice has the smallest radius in this region. However, because this beam slice was strongly focused, it will strongly diverge once it has passed its focal point and a different beam slice will dominate the FWHM measurement. As the focal length of each successively focused beam slice increases, the minimum spot size of each slice increases according to standard beam dynamics and therefore the time-integrated FWHM increases according to the minimum spot size of the focused slice at the position of interest rather than the beam envelope of any one particular slice. Therefore, the asymmetry is caused by the longitudinal aberrations from the plasma lens due to time dependent focusing.

The same procedure can be repeated for various beam charges to predict the time-integrated spot size as a function of charge. Calculations of the FWHM for time-integrated profiles were performed for beam charges ranging from 75 pC to 0.5 nC. As seen in Fig. 4.13, the results of the calculations fit the measurements well.

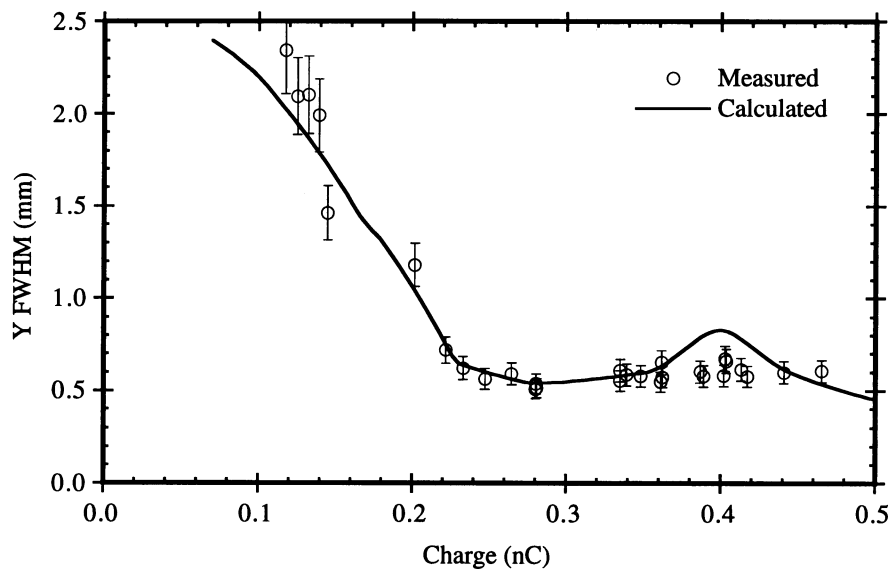


Figure 4.13: Spot Size at PM2 as a Function of Beam Charge

Considering the simplicity of the model, the wakefield calculation results agree very well with both the time-resolved and time-integrated measurements. Although it was assumed that the initial beam conditions were not functions of time and that the initial gaussian form of the beam profile was not altered by the lens, the minimum spot size, the focal length, and the time dependent focusing were all correctly modeled by the wakefield theory. The measured time-integrated beam profile was matched by the calculations and its dependence on beam charge predicted. In addition, with the help of the wakefield calculations, the asymmetry in the beam envelope equation is correctly interpreted as a manifestation of longitudinal aberrations induced by the time dependent focusing of the overdense plasma lens.

4.7 Simulations

Some of the limitations of the analytic wakefield model can be addressed by using particle simulations. In calculating the solution to the wakefield equations, the beam current and beam radius is kept constant in the plasma and the beam velocity is assumed to equal the speed of light. Particle acceleration or deceleration due to axial electric wakefields is ignored and the beam's spatial profile is assumed to be self-similar after propagating through the plasma lens. Furthermore, the initial conditions for solving the beam envelope equation are independent of time. The effects of these limitations are minimized by the procedure of dividing the beam and plasma into slices, however, in order to perform a fully self-consistent calculation, particle simulations must be used. Particle simulations are generally limited by computer time and memory. Fully

selfconsistent three dimensional simulations are prohibitive due to cost and, therefore, as with the wakefield calculations, azimuthal symmetry is assumed.

The initial conditions of the electron beam before entering the overdense plasma lens are predicted by the particle code PARMELA. With PARMELA, the electron beam is modeled from its creation at the photo-cathode in the rf gun to the position of PM1, through the differential pumping section of the beamline. This code employs point to point space charge calculations in modeling the Coulomb repulsion between the beam particles. Although the beam particles are modeled in full three dimensions, azimuthal symmetry is assumed in the rf gun and the beamline. Furthermore, since the point to point calculations are extremely time consuming, the number of particles used to model the electron beam was limited to 4000. The beamline apertures used for the differential pumping system are included in the simulation and, as was measured experimentally, > 50% of the beam particles are lost to the beampipe walls as the beam is propagated through those sections. The focusing solenoid is also included in the simulation. Most of the simulation parameters are known from direct measurements. The initial spot size of the electron bunch is determined by the laser and is gaussian with a 1 mm sigma. The initial electron bunch length of 50 ps FWHM is likewise determined by the laser. Based on the measured beam charge at FC0 and at the ICT, the initial beam charge at the cathode was set equal to 1.0 nC so that the charge at the position corresponding to the ICT equaled 0.5 nC, in agreement with the measurements during the lens experiment. The accelerating gradient in the rf gun is set to 80 MV/m in order to match the measured beam energy of 3.5 MeV. Only two simulation parameters were not measured directly, the rf injection phase and the solenoid strength. Simulations were run for various injection phases until the final temporal profile from the simulation matched that of the

measurement as shown in Fig. 3.32. With the rf injection phase chosen, simulations for various solenoid focusing fields were run until the best fit with the measured time-integrated beam envelope was achieved. The simulated beam envelope from PARMELA is plotted with the measured envelope in Fig. 4.14. The normalized emittance predicted

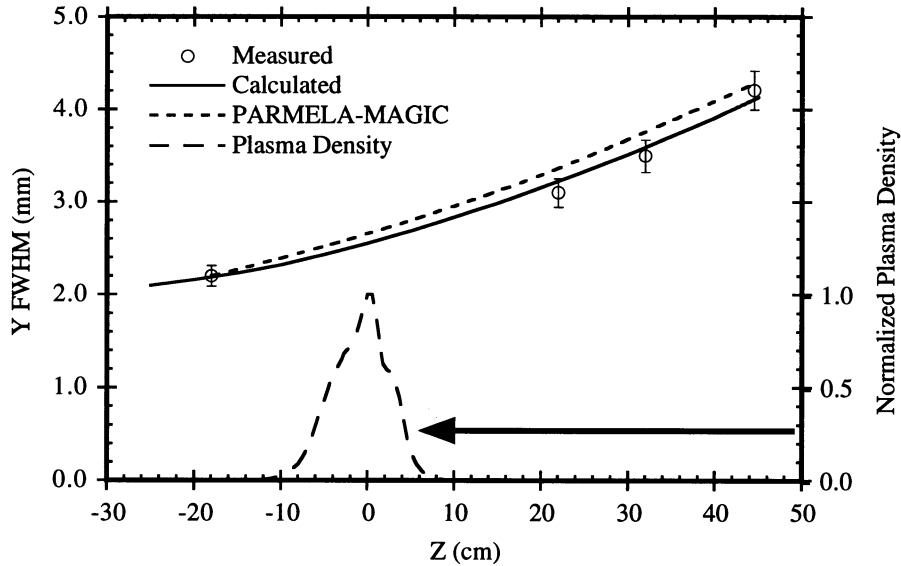


Figure 4.14: Simulated, Calculated and Measured Beam Envelope with Plasma Off

by PARMELA at PM1 is 8π -mm-mrad, in good agreement with measurements and the wakefield calculations, while the beam divergence at PM3 predicted by PARMELA was 1.2 mm-mrad, in agreement with what was predicted by the beam envelope equation in Section 4.6. Since half of the beam charge is lost while propagating through the differential pumping system, only about 2000 particles remain in the simulation at the position corresponding to PM1. These 2000 particles, representing 0.5 nC of beam charge, are exported to a PIC simulation code, MAGIC, for propagation through the plasma lens.

The simulation code MAGIC is a fully electromagnetic and relativistic PIC code which can simulate the interaction of the electron beam with a plasma. The plasma is

represented by 80,000 electrons and ions, however, the ions are assumed to be infinitely massive and therefore immobile. It was discussed in Section 2.4, that this assumption is valid for times corresponding to the electron beam propagation time through the plasma. The plasma profile created in the simulation is uniform in the radial dimension, but in the axial dimension the measured plasma profile is reproduced. Since this is a fully electromagnetic code, the response of the plasma is modeled self-consistently as the electron beam is affected within the plasma and allows for beam acceleration and deceleration from the axial wakefield generated in the plasma. However, MAGIC is a 2-1/2 dimensional code in which azimuthal symmetry is assumed. The 1000 particles from PARMELA are imported into MAGIC and propagated through the plasma. Both time-resolved and time-integrated beam profile information is extracted from the simulation.

The time-resolved results of the PARMELA-MAGIC simulation at the position of the Cherenkov radiator, 31 cm downstream of the plasma, are graphed in Fig. 4.15 along with the measured values from the streak data and the calculated values from the

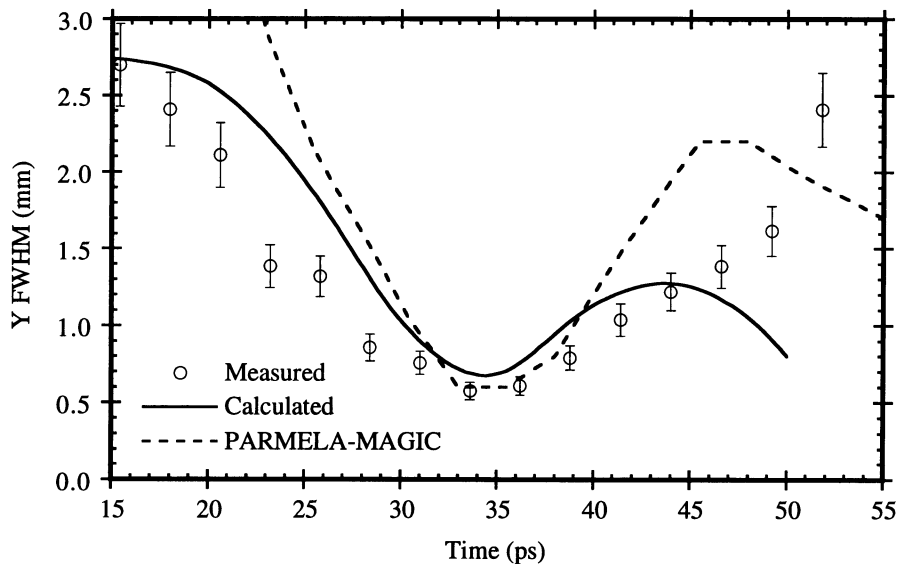


Figure 4.15: Simulation, Calculation and Measurement of Dynamic Focusing from the Plasma Lens

wakefield model. Although the simulation results do not match the data as well as the wakefield calculations, the minimum spot size and the time at which it occurs is correctly predicted. The time-integrated beam profile at PM2 is also extracted from the simulations and plotted with the measured profile and the calculated profile in Fig. 4.16. The FWHM

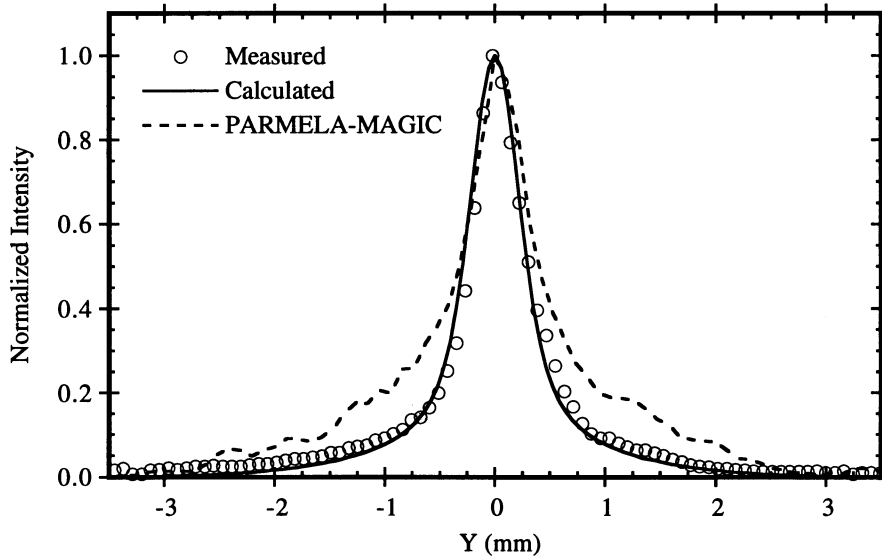


Figure 4.16: Simulated, Calculated and Measured Beam Profile at PM2.

of the MAGIC profile is 0.7 mm which agrees with the measured value to within 20%, however, although evidence of wings are visible in the simulation profile, the wings have a much larger amplitude than those of the measured and calculated profiles. In Fig. 4.17 the FWHM beam envelope is plotted for the simulated, calculated and measured values. Once again the minimum spot size is correctly predicted by the simulations as is the axial position at which it occurs.

Although the PARMELA-MAGIC simulations include a more detailed description of the electron beam and the beam plasma interaction than that of the wakefield model, the wakefield model showed better agreement with the measurements. Some of the reasons for the discrepancy could be in the added complexity of the simulations. Remember that

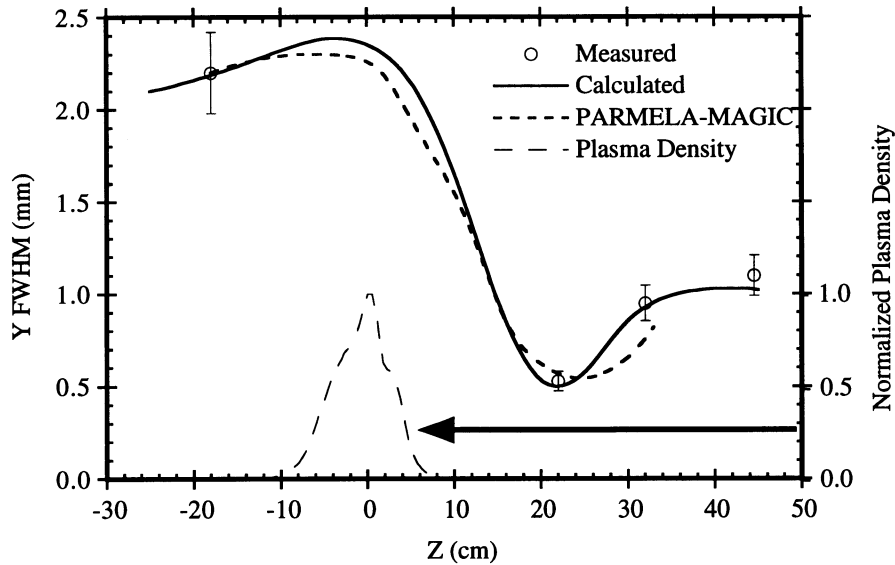


Figure 4.17: Simulated, Calculated and Measured Beam Envelope with the Plasma On

in matching the PARMELA with the measurements, the beam is propagated from the cathode of the rf gun, whereas, in the wakefield calculations, the beam propagation upstream of PM1 was ignored and only the beam profile from PM1-4 was considered in determining the initial conditions of the electron beam for the calculations. Also recall from Chapter 3 that the rf gun 1/2 cell and full cell field were unbalanced during the experiment. After the experiment the field balance was determined, however, since the balance is extremely sensitive to the cathode position, it is likely that the measured field imbalance did not match the actual field imbalance during the overdense lens experiment. In the PARMELA simulation, the measured field imbalance is used to determine the relative field strengths in the 1/2 cell and full cell of the rf gun. If the actual field balance during the experiment was different, the initial beam conditions predicted by PARMELA would be incorrect and the results of the MAGIC simulations would be duly affected. The uncertainty in the field balance is probably the largest source of error in the particle simulations. Nevertheless, good agreement of the simulations with the wakefield

calculations and the measured values was achieved.

4.8 Summary

A practical overdense plasma lens was fully characterized using the electron beam described in Chapter 3. Both time-resolved and time-integrated spot size measurements were performed under the same experimental conditions. The time-resolved measurements demonstrated the dynamic focusing properties of the overdense plasma lens which are also manifested in the time-integrated spot size measurements as an asymmetry in the beam envelope through the focus. The head of the beam remained unfocused as expected due to the finite response time of the plasma, while the rest of the beam was focused to a varying degree depending on the wakefield response of the plasma and the current profile of the electron beam. Significant beam focusing was observed with the original spot size of 2.4 mm FWHM being reduced to 0.55 mm FWHM at the best focus. This factor of 4 reduction in spot size was achieved over a focal length of 21 cm. The measurements were compared with numerical calculations based on the wakefield theory presented in Chapter 2 and PARMELA-MAGIC particle simulations. Good agreement between the simulations, calculations, and measurements was realized. Furthermore, by using the calculations, a deeper understanding of the physical mechanism behind the dynamic focusing of the overdense plasma lens was gained. Because of the sharp risetime of the electron beam, ≈ 7 ps, a strong wakefield is generated in the plasma. The observed plasma lens focusing was due in part (60%) to an electrostatic radial electric field component of the wakefield and in part (40%) to the azimuthal self-magnetic field generated by the electron beam.

Chapter 5

Conclusion

Luminosity continues to be a critical parameter for present and future electron beam colliders. The most effective way to increase the luminosity is by reducing the spot size of the electron beam at the interaction point. Currently, the smallest achievable beam size is limited by the focusing strength of conventional magnets and alignment tolerances of quadrupole focusing systems. In order to significantly improve the electron beam focusing a novel focusing element must be employed.

The overdense plasma lens is a good candidate for a final focusing element. From the theoretical analysis, focusing gradients, orders of magnitude larger than those of conventional magnets, are predicted with collider type electron beams. This dissertation described the full characterization of the overdense plasma lens. Although these extremely large focusing gradients were not demonstrated, the fundamental properties of the overdense plasma lens were examined and compared with the theory.

In order to study the overdense plasma lens, an electron beam suitable for characterizing the overdense plasma lens was developed and characterized. A successful overdense plasma lens experiment demanded a bunch length long enough to resolve with

a streak camera (> 5 ps), a beam charge capable of producing a significant focusing force, and a beam energy such that the electron beam would focus downstream of the plasma with a significant reduction in spot size (> 2). The beam was produced by a rf photoinjector which delivered a 25 ps FWHM electron bunch with variable charge from 0.1 - 0.6 nC (delivered at the plasma lens), and a beam energy of 3.5 MeV.

Utilizing this electron beam, the overdense plasma lens was fully characterized. The overdense plasma lens produced a factor of 4 spot size reduction 21 cm downstream of the plasma. This focusing was temporally resolved 31 cm downstream from the plasma, demonstrating the dynamic focusing of the overdense plasma lens. The head of the electron bunch was unaffected by the plasma lens while the rest of the beam manifested varying degrees of focusing. The minimum spot size occurred 35 ps from the head of the pulse, corresponding to the plasma response time. This dynamic focusing was compared with analytic calculations and computer simulations and good agreement was achieved. Using these results, the time integrated behavior of the electron beam envelope was explained.

Future work on plasma lenses should be pursued on two fronts. One front is the implementation of an overdense plasma lens with a collider quality electron beam. Although the overdense plasma lens has been fully characterized, an experiment which demonstrates significant focusing of a collider type electron beam should be performed. In particular, the experiment should produce an enhancement in beam luminosity beyond what is possible with a conventional quadrupole system. An overdense lens experiment using the SLAC beam is being proposed and if approved should prove the feasibility of using overdense plasma lenses in future electron beam colliders. The second front is experimental verification of the underdense plasma lens and a full characterization of its

properties. As was discussed briefly in Chapter 2, the underdense lens could provide some advantages over the overdense lens. Although the focusing strength of the underdense lens will always be less than that of the overdense lens for the same electron beam, the spherical and temporal aberrations may be smaller than those of the overdense lens. The net effect on beam luminosity should be examined in order to determine whether an underdense lens may be more favorable for use in electron beam colliders. Nevertheless, it has been demonstrated that an overdense plasma lens can provide significant focusing of an electron beam and that although the focusing is extremely dynamic, it is well understood theoretically and both analytic calculations and computer simulations can be used to model such a lens for use in future electron beam colliders.

Bibliography

- [1] S. Humphries, *Charged Particle Beams* (J. Wiley and Sons, New York, 1990)
- [2] P. Chen *et al.*, "Final focusing and enhanced disruption from an underdense plasma lens in a linear collider", *Physical Review D*, **40**, 923 (1989)
- [3] B. Richter, "Very High Energy Colliders", *IEEE Transactions on Nuclear Science*, **NS-32**, 3828 (1985).
- [4] P. Tenenbaum *et al.*, SLAC-PUB-6593 (1994)
- [5] T. Katsouleas, "Physical mechanisms in the plasma wake-field accelerator", *Physical Review A*, **33**, 2056 (1986)
- [6] P. Chen, "A Possible Final Focusing Mechanism For Linear Colliders", *Particle Accelerators*, **20**, 171 (1987).
- [7] J.B. Johnson, "A Low Voltage Cathode Ray Oscillograph", *Journal of the Optical Society of America*, **6**, 701 (1922)

- [8] A.S. Halsted and D.A. Dunn, "Electrostatic and Magnetic Pinch Effects in Beam-Generated Plasmas", *Journal of Applied Physics*, **37**, 1810 (1966)
- [9] D. Gabor, "A Space-Charge Lens for the Focusing of Ion Beams", *Nature*, **160**, 89 (1947)
- [10] See A.S. Halsted and D.A. Dunn, "Electrostatic and Magnetic Pinch Effects in Beam-Generated Plasmas", *Journal of Applied Physics*, **37**, 1810 (1966) and references therein.
- [11] G. Hairapetian, "Plasma Based Lenses for Charged Particle Beams", *Advanced Accelerator Concepts*, edited by Paul Schoessow, AIP Conference Proceedings 335, 174 (1994)
- [12] J.A. Palkovic *et al.*, "Gabor lens focusing of a proton beam", *Review of Scientific Instruments* , **61**, 550 (1990)
- [13] T.J. Murphy and C.M. Surko, "Positron trapping in an electrostatic well by inelastic collisions with nitrogen molecules", *Physical Review A* , **46**, 5696 (1992)
- [14] W.K.H. Panofsky and W.R. Baker, "A Focusing Device for the External 350-MeV Proton Beam of the 184-Inch Cyclotron at Berkeley", *Review of Scientific Instruments*, **21**, 445 (1950)

- [15] E. Boggasch *et al.*, "Z-Pinch Plasma Lens Focusing of a Heavy-Ion Beam", *Physical Review Letters*, **66**, 1705 (1991)
- [16] B. Autin *et al.*, "A Z-Pinch Plasma Lens for Focusing High-Energy Particles in an Accelerator", *IEEE Transactions on Plasma Science*, **PS-15**, 226 (1987)
- [17] F. Dothan *et al.*, "Dynamics of a z pinch for focusing high-energy charged particles", *Journal of Applied Physics*, **62**, 3585 (1987)
- [18] P.J. Channel *et al.*, "Laser Focusing of Particle Beams", in *Laser Acceleration of Particles*, AIP Conference Proceedings No. 130, 407 (1985)
- [19] R. Ruth *et al.*, *Particle Accelerators*, **17**, 171 (1985)
- [20] J.B. Rosenzweig *et al.*, "Experimental measurement of nonlinear plasma wake fields", *Physical Review A*, **39**, 1586 (1989)
- [21] W.H. Bennett, "Magnetically Self-Focussing Streams", *Physical Review*, **45**, 890 (1934)
- [22] R. Keinigs and M.E. Jones, "Two-dimensional dynamics of the plasma wakefield accelerator", *Physics of Fluids*, **30**, 252 (1987)
- [23] J.J. Su *et al.*, " Plasma lenses for focusing particle beams", *Physical Review A*, **41**,

3321 (1990)

[24] P. Chen *et al.*, "Plasma-Based Adiabatic Focuser", *Physical Review Letters*, **64**, 1231 (1990)

[25] S.E. Graybill and S.V. Nablo, "Observations of Magnetically Self-Focusing Electron Streams", *Applied Physics Letters*, **8**, 18 (1966)

[26] J.B. Rosenzweig *et al.*, " Demonstration of electron beam self-focusing in plasma wake fields ", *Physics of Fluids B*, **2**, 1376 (1990)

[27] H. Nakanishi *et al.*, "Direct Observation of Plasma-Lens Effect", *Physical Review Letters*, **66**, 1870 (1991)

[28] G. Hairapetian *et al.*, "Experimental Demonstration of Dynamic Focusing of a Relativistic Electron Bunch by an Overdense Plasma Lens", *Physical Review Letters*, **72**, 2403 (1994)

[29] G. Hairapetian *et al.*, "Transverse dynamics of a short, relativistic electron bunch in a plasma lens", *Physics of Plasmas*, **2**, 2555 (1995)

[30] D. Betz *et al.*, "Plasma Lenses for SLAC Final Focus Test Facility", *Proceedings of the Particle Accelerator Conference*, San Francisco, 619 (1991)

- [31] J.L. Cox and W.H. Bennett, "Reverse Current Induced by Injection of a Relativistic Electron Beam into a Pinched Plasma", *Physics of Fluids*, **13**, 182 (1970)
- [32] P. Chen *et al.*, "Acceleration of Electrons by the Interaction of a Bunched Electron Beam with a Plasma", *Physical Review Letters*, **54**, 693 (1985)
- [33] S. Humphries, *Charged Particle Beams* (J. Wiley and Sons, New York, 1990) pp. 87-93
- [34] J.B. Rosenzweig *et al.*, "Luminosity Enhancement in Linear Colliders Using a Short-Focal-Length Plasma Lens", *Particle Accelerators*, **24**, 11 (1988)
- [35] J.B. Rosenzweig, "Acceleration and Focusing of Electrons in Two-Dimensional Nonlinear Plasma Wakefields", *Physical Review A*, **44**, 6189 (1991)
- [36] B. Golpen *et al.*, "User-Configurable MAGIC for Electromagnetic PIC Calculations", *Computer Physics Communications*, **87**, 54 (1995)
- [37] K.T. McDonald, "Design of the Laser-Driven RF Electron Gun for the BNL Accelerator Test Facility", *IEEE Transactions on Electron Devices*, **ED-35**, 2052 (1988)
- [38] M. Hogan *et al.*, "Status of the UCLA High-Gain Infrared Free Electron Laser", *Proceedings of the 1995 Particle Accelerator Conference*, Paper FAA23 (1995)

- [39] S.C. Hartman, "The UCLA High-Brightness Rf Photo-Injector", *Ph.D. Dissertation* (UCLA, 1993)
- [40] R.B. Miller, *Intense Charged Particle Beams*, (Plenum Press, New York, 1982) p.155
- [41] J.D. Lawson, *The Physics of Charged-Particle Beams*, (Oxford University Press, London, 1977), pp. 384-387
- [42] J.S. Fraser *et al.* "High-Brightness Photoemitter Injector for Electron Accelerators", *IEEE Transactions on Nuclear Science*, **NS-32**, 1791, (1985)
- [43] R.L. Sheffield *et al.*, "The Los Alamos Photoinjector Program", *Nuclear Instruments and Methods in Physics Research*, **A272**, 222 (1988)
- [44] S. Humphries, *Principles of Charged Particle Acceleration*, (J. Wiley and Sons, New York, 1986), p.377
- [45] W.D. Kilpatrick, "Criterion for Vacuum Sparking Designed to Include Both rf and dc", *The Review of Scientific Instruments*, **28**, 824 (1957)
- [46] J.S. Fraser and R.L. Sheffield, "High-Brightness Injectors for RF-Driven Free-Electron Lasers", *IEEE Journal of Quantum Electronics*, **QE-23**, 1489 (1987)

- [47] K.J. Kim, "RF and Space-Charge Effects in Laser-Driven RF Electron Guns", *Nuclear Instruments and Methods in Physics Research*, **A275**, 201 (1989)
- [48] C. Travier, "An Introduction to Photo-Injector Design", *Workshop on High Intensity Photocathodes, Legnaro, Italy, May 24-28* (1993)
- [49] L.P. Smith, "Chapter 6:Thermionic Emission", *Handbook of Physics*, edited by Condon and Odishaw, 8-67 (McGraw-Hill, 1967)
- [50] J.S. Fraser *et al.*, "A New High-Brightness Electron Injector for Free Electron Lasers Driven by RF Linacs", *Nuclear Instruments and Methods in Physics Research*, **A250**, 71 (1986)
- [51] R.W. Springer and B.J. Cameron, "Photocathode transfer and storage techniques using alkali vapor feedback control", *Nuclear Instruments and Methods in Physics Research*, **A318**, 396 (1992)
- [52] K. Halbach and R.F. Holsinger, "SUPERFISH-A Computer Program for Evaluation of RF Cavities with Cylindrical Symmetry", *Particle Accelerators*, **7**, 213 (1976)
- [53] E. Ginzton, *Microwave Measurements*, (McGraw-Hill, 1957)
- [54] L.C. Maier and J.C. Slater, "Field Strength Measurements in Resonant Cavities",

Journal of Applied Physics, **23**, 68 (1952)

[55] P. Maine *et al.*, "Generation of Ultrahigh Peak Power Pulses by Chirped Pulse Amplification", *IEEE Journal of Quantum Electronics*, **24**, 398 (1988).

[56] D.W. Juenker *et al.*, "Vectorial Photoelectric Effect in Clean Molybdenum", *Journal of the Optical Society of America*, **54**, 216 (1964)

[57] T. Srinivasan-Rao *et al.*, "Photoemission studies on metals using picosecond ultraviolet laser pulses", *Journal of Applied Physics*, **69**, 3291 (1991)

[58] X.J. Wang, "High-Brightness Electron Accelerator Injection System and Experimental Studies of Laser-Induced Explosive Electron Emission", *Ph.D. Dissertation* (UCLA, 1992)

[59] P. Davis *et al.*, "Quantum Efficiency Measurements of a Copper Photocathode in an RF Electron Gun", *Proceedings of the 1993 Particle Accelerator Conference*, **4**, 2976 (1993)

[60] R. Brogle *et al.*, "Studies of Linear and Nonlinear PhotoEmission for Advanced Accelerator Applications", *Proceedings of the 1995 Particle Accelerator Conference*, Paper WPC20 (1995)

[61] S.C. Hartman *et al.*, "Emittance Measurements of the 4.5 MeV UCLA RF Photo-Injector", *Proceedings of the 1993 Particle Accelerator Conference*, **4**, 561 (1993)

[62] C. Lejeune and J. Aubert, *Emittance and Brightness Definitions and Measurements*, (Academic Press, New York, 1980)

[63] S.C. Hartman *et al.*, "Initial Measurements of the UCLA RF Photoinjector", *Nuclear Instruments and Methods in Physics Research*, **A340**, 219 (1994)

[64] F.F. Chen, *Introduction to Plasma Physics and Controlled Fusion* (Plenum Press, New York, 1984) p. 352

[65] S.C. Brown, *Basic Data of Plasma Physics* (MIT Press, Cambridge, MA, 1966)

[66] F.F. Rieke and W. Prepejchal, "Ionization Cross Sections of Gaseous Atoms and Molecules for High-Energy Electrons and Positrons", *Physical Review A*, **6**, 1507 (1972)